KINETICS AND MICROSTRUCTURAL ANALYSIS OF FATIGUE FRACTURE PROGRESS IN WELD JOINTS OF DUPLEX STAINLESS STEEL GRADE 2205

A THESIS SUBMITTED TO
THE GRADUATE SCHOOL OF NATURAL AND APPLIED SCIENCES
OF
MIDDLE EAST TECHNICAL UNIVERSITY

BY

KORAY YURTIŞIK

IN PARTIAL FULFILLMENT OF THE REQUIREMENTS
FOR
THE DEGREE OF DOCTOR OF PHILOSOPHY
IN
METALLURGICAL AND MATERIALS ENGINEERING

JUNE 2013

Approval of the thesis

KINETICS AND MICROSTRUCTURAL ANALYSIS OF FATIGUE FRACTURE PROGRESS IN WELD JOINTS OF DUPLEX STAINLESS STEEL GRADE 2205

Submitted by **KORAY YURTIŞIK** in partial fulfilment of the requirements for the degree of **Doctor of Philosophy in Metallurgical and Materials Engineering Department, Middle East Technical University** by

Prof. Dr. Canan Özgen
Dean, **Graduate School of Natural and Applied Sciences** _____

Prof. Dr. C. Hakan Gür
Head of Department, **Metallurgical and Materials Eng.** _____

Prof. Dr. Rıza Gürbüz
Supervisor, **Metallurgical and Materials Eng. Dept., METU** _____

Examining Committee Members

Prof. Dr. Bilgehan Ögel
Metallurgical and Materials Eng. Dept., METU _____

Prof. Dr. Rıza Gürbüz
Metallurgical and Materials Eng. Dept., METU _____

Prof. Dr. C. Hakan Gür
Metallurgical and Materials Eng. Dept., METU _____

Prof. Dr. Ali Kalkanlı
Metallurgical and Materials Eng. Dept., METU _____

Assist. Prof. Dr. Kazım Tur
Metallurgical and Materials Eng. Dept., Atılım University _____

DATE: 27/06/2013

I hereby declare that all information in this document has been obtained and presented in accordance with academic rules and ethical conduct. I also declare that, as required by these rules and conduct, I have fully cited and referenced all material and results that are not original to this work.

Name, Last Name: Koray YURTIŞIK
Signature:

ABSTRACT

KINETICS AND MICROSTRUCTURAL ANALYSIS OF FATIGUE FRACTURE PROGRESS IN WELD JOINTS OF DUPLEX STAINLESS STEEL GRADE 2205

Yurtışık, Koray

Ph. D., Department of Metallurgical and Materials Engineering
Supervisor: Prof. Dr. Rıza Gürbüz

September 2012, 125 Pages

Despite its high efficiency, autogenous keyhole welding technique leads to an excessive δ-ferrite formation in as-welded duplex stainless steels that leads to deterioration of the corrosion properties of the material, as well as its toughness. Developing the hybrid plasma-gas metal arc welding procedure for duplex stainless steels, a narrow gap and single-pass weldment on 11 mm-thick duplex stainless steel (grade 2205) plates has been achieved. Contrary to other keyhole techniques, such as Laser beam welding, electron beam welding and conventional plasma arc welding, the developed procedure apparently enabled us to obtain a proper cooling rate and weld metal chemistry, which were the key factors determining the microstructure and consequently corrosion and mechanical properties of the material. Fatigue crack propagation behaviour of the fusion zone in both air and sour environments has been interested and investigated within the damage tolerant design framework.

A comparative analysis basis methodology was employed during investigations; beside hybrid plasma-gas metal arc welding, gas metal arc welding and plasma arc welding were also operated to obtain two reference duplex stainless steel weldments. Simultaneous utilization of keyhole and filler metal deposition in this hybrid welding process enabled us to achieve less total heat input and arc time compared to conventional multi-pass gas metal arc welding. Therefore precipitation secondary phases were considerably supressed. Moreover, microstructural examinations and analyses provided data indicating a sufficient reconstructive transformation of primary austenite in the fusion zone of the weldment obtained using hybrid plasma gas-metal arc welding, and that was not possible using autogenous plasma arc welding.

Fatigue crack propagation tests were conducted in laboratory air and 3.5% NaCl solution on compact tension specimens, which were notched at the centre of fusion zone of the weldments. Controversial effect of the secondary austenite on crack propagation behaviour was the primary interest among the others, such as residual stress, phase balance and precipitates of chromium-nitrides and intermetallic phases. On the one hand, retarding the crack propagation in near threshold stress intensity factor range, precipitation of the secondary austenite in multi-pass weldment was observed to be beneficial for as-welded duplex stainless steel as long as the material would give service in air. On the other hand, the

secondary austenite led to chromium and molybdenum depleted zone, where pitting and crevice resistance of the material was relatively low. Crack propagation rate of secondary austenite free single-pass weldment that was obtained employing the hybrid welding was lower than the one of multi-pass weldment in the sour environment. Crack propagation rate data was supported with comprehensive fractography and micro analysis works.

Keywords: *Hybrid plasma-gas metal arc welding; Keyhole welding; Gas metal arc welding; Duplex stainless steel; Phase balance; Secondary austenite; Intermetallic phases; Chromium nitride; Crack propagation; Chloride environment.*

ÖZ

2205 SINIFI DUBLEKS PASLANMAZ ÇELİK ALAŞIMI KAYNAKLI BİRLEŞTİRMELERİNDE YORULMA ÇATLAĞI İLERLEMESİNİN KİNETİK VE İÇ YAPI ANALİZİ

Yurtışık, Koray

Doktora, Metalurji ve Malzeme Mühendisliği Bölümü
Tez Yöneticisi: Prof. Dr. Rıza Gürbüz

Eylül 2012, 125 Sayfa

Yüksek verimliliğine rağmen, otojen anahtar-deliği kaynağı tekniği, malzemenin tokluğunu olduğu kadar korozyon özelliklerini de olumsuz etkileyecek şekilde δ-ferrit oluşumuna neden olur. Dubleks paslanmaz çelikler için hibrit plazma-gaz metal ark kaynağı prosedürü geliştirilerek, 11 mm kalınlığında dubleks paslanmaz (2205 sınıfı) çeliğinden mamul plakaların, dar aralık ve tek paso kaynaklanması başarılmıştır. Lazer ışın kaynağı, elektron ışın kaynağı ve plazma ark kaynağı gibi diğer anahtar-deliği kaynak uygulamalarının aksine geliştirilen prosedür, malzemenin iç yapısını ve dolayısı ile mekanik ve korozyon özelliklerini belirleyen anahtar etmenler olarak uygun soğuma hızı ve kaynak metali compozisyonunun elde edilmesini mümkün kılmıştır. Ergime bölgesinin hava ve tuzlu su ortamlarında yorulma çatlağı ilerleme davranışına hasar tolere tasarım çerçevesinde odaklanılmış ve bu davranış incelenmiştir.

Çalışmalarımızda karşılaştırmaya dayalı bir araştırma yöntemi uygulanmıştır; hibrit plazma-gaz altı ark kaynağı uygulamasına ilave olarak gaz metal ark kaynağı ve plazma ark kaynağı yöntemleri uygulanarak iki referans kaynaklı birleştirme de elde edilmiş ve incelenmiştir. Bu hibrit kaynak yönteminde anahtar-deliği oluşumu ile dolgu metal transferinin birlikte gerçekleştirilmesi, çok pasolu gaz metal ark kaynağı yöntemine göre kaynak işleminin daha az toplam ısı girdisi ve ark yanma süresi ile tamamlanmasını sağlamıştır. Bu sayede ikincil faz oluşumları büyük oranda baskılanmıştır. Bununla birlikte, otojen plazma ark kaynağı ile mümkün değilken, hibrit plazma-gaz metal ark kaynağı ile elde edilen ergime bölgesinde yeteri miktarda birincil östenit oluşumu söz konusudur.

Yorulma çatlağı ilerleme testleri, çentikleri ergime bölgesi merkezinde açılmak suretiyle kompakt çekme numuneleri üzerinde laboratuvar havası ve 3.5% NaCl çözeltisi ortamlarında gerçekleştirilmiştir. Kalıntı gerilim, faz dengesi ve krom-nitrür ile intermetalik faz çökeltiler gibi diğer etkenler arasında, ikincil östenitin ortama bağlı değişken etkileri çalışmanın birincil odağı olmuştur. Bir yandan, malzeme hava ortamında hizmet verdiği sürece, ikincil östenit oluşumlarınıb, çatlak ilerleme hızını gerilim yoğunluk faktör aralığı eşik değeri bölgesinde yavaşlatarak faydalı olduğu gözlemlenmiştir. Diğer yandan, ikincil östenit oluşumları komşuluklarında krom ve molibden fakrleşmesine sebebiyet vermekte, bu vesile ile çukurcuk ve dar aralık korozyon direncinin görece düşmesine neden olmaktadır. Hibrit kaynak yöntemi ile elde edilmiş tek pasolu ve ikincil östenit bulunmayan birleştirmelerin

tuzlu su ortamında çatlak ilerleme hızlarının görece düşük olduğu kaydedilmiştir. Çatlak ilerleme hızı verileri kapsamlı mikroskop ve mikro analiz çalışmalarıyla desteklenmiştir.

Anahtar Kelimeler: *Hibrit plazma-gaz metal ark kaynağı; Anahtar-deliği kaynağı; Gaz metal ark kaynağı; Dubleks paslanmaz çeliği; Faz dengesi; İkincil östenit; Intermetalikler; Krom-nitrür; Çatlak ilerlemesi; Klorür ortamı.*

To Two Beloved Ladies;
one of whom has been taken away from my life early,
and one of whom has become a part of my life late.

ACKNOWLEDGMENTS

I sincerely thank my supervisor Prof. Dr. Rıza Gürbüz, who not only guided me during this study but also believed in me and provided me a big playground, in which I could do in a way that I'd like to do.

I sincerely appreciate Prof. Dr. C. Hakan Gür and Assist. Prof. Dr. Kazım Tur for their motivation, guidance and support.

No amount of gratitude can balance the generosity and support provided by my colleague and friend, Dr. Süha Tirkeş, throughout my studies.

Dr. Turhan Güngör, Mrs. Burcu Tolungüç and Mr. Alp Tolungüç, who valued my works and improved the manuscript greatly through their sensitive and competent editing, deserve a deep appreciation.

I deeply appreciate Mr. Zafer Filiz, Mr. Göksu Gürer and Mr. Tolga Ertürk, whose help and advices were invaluable. Mr. Arif Atalay Özdemir, Mr. Erkan Biçer, Mr. Cemal Yanardağ, Mr. Bedirhan Özener, Mr. Orhan Aydın, Mr. Önder Şahin and Mr. Yücel Ateş were very supportive and altruistic during fabrication and testing processes.

Dr. Igor Dykhno, Dr. Georgi Ignatchenko and Mr. Dmitry Marchuk deserve a profound appreciation; sharing their experience, they provided very valuable guidance through my studies.

Despite their irrelevant professions, law and social anthropology, my beloved mother, Gülseren, and my beloved wife, Theresa, definitely contributed to the formation of this thesis with their love and wisdom.

Last but not least, I am thankful to my 3-month-old son, Lukas, since he provided me plenty of time and energy to pursue my studies with his lovely smiles and sleeps as if he knew that I needed them.

I am deeply in their dept.

TABLE OF CONTENTS

LIST OF TABLES

LIST OF FIGURES

LIST OF SYMBOLS

A	Elongation
α	Alpha Ferrite
δ	Delta Ferrite
γ	Austenite
γ_1	Primary Austenite
γ_2	Secondary Austenite
γ_W	Widmanstätten Austenite
T_δ	Ferritization temperature
σ	Sigma Phase
χ	Chi Phase
V_γ	Volume fraction of austenite
V_δ	Volume fraction of delta ferrite
$R_{p0.2}$	0.2% offset yield stress (proof stress)
R_m	Ultimate tensile strength

ABBREVIATIONS

ASME	The American Society of Mechanical Engineers
ASTM	American Society for Testing and Materials
AWS	American Welding Society
BCC	Body Centred Cubic (lattice structure)
CCT	Continuous Cooling Transformation (diagram)
CGHAZ	Coarse Grained Heat Affected Zone
Cr_{eq}	Chromium equivalent
CPT	Critical Pitting Temperature
CT	Compact Tension (specimen)
CTOD	Crack Tip Opening Displacement
DIN	Deutsches Institut für Normung
DSS	Duplex Stainless Steel
EBW	Electron Beam Welding
EDS	Energy Dispersive Spectral Analysis
EDX	Energy Dispersive X-ray Analysis
FCG	Fatigue Crack Growth
FCC	Face Centred Cubic (lattice structure)
FGHAZ	Fine Grained Heat Affected Zone
FZ	Fusion Zone (weld metal)
GMAW	Gas Metal Arc Welding
GTAW	Gas Tungsten Arc Welding
HAZ	Heat Affected Zone
HLAW	Hybrid Laser Arc Welding
HPAW	Hybrid Plasma-Gas Metal Arc Welding
HV	Vickers Hardness
IGC	Intergranular Corrosion
IIW	International Institute of Welding
ISO	International Organization for Standardization
T_Z	Inter-pass Temperature
LBW	Laser Beam Welding
LWS	Linear Welding Speed

MAG	Metal Active Gas Welding
MIG	Metal Inert Gas Welding
NACE	National Association of Corrosion Engineers
Ni_{eq}	Nickel Equivalent
PAW	Plasma Arc Welding
PRE_N	Pitting Resistance Equivalent Number
PRE_W	Pitting Resistance Equivalent Number (including Tungsten)
T_V	Pre-heating Temperature
PQR	Procedure Qualification Record
PWHT	Post Weld Heat Treatment
SCC	Stress Corrosion Cracking
SEM	Scanning Electron Microscope
TEM	Transmission Electron Microscope
TIG	Tungsten Inert Gas Welding
TTT	Time-temperature Transformation (diagram)
UNS	Unified Numbering System
UTS	Ultimate Tensile Strength
WFS	Wire Feeding Speed
WPS	Welding Procedure Specification

CHAPTER 1

INTRODUCTION

The balanced ferrite (δ) and austenite (γ) content of duplex stainless steel, DSS, offers a good combination of strength and corrosion resistance. Due to its relatively higher strength, chloride stress-corrosion cracking and pitting resistance, DSS has been preferred to austenitic stainless steels enclosing and constructive assemblies where especially chloride attack is a consideration. Welding is a necessary process in fabrication of such assemblies.

The new generation of DSS has a good weldability by conventional arc welding methods as long as the heat input and inter-pass temperatures are adjusted in order to ensure a proper γ to δ ratio in the weld metal and heat affected zone (HAZ) [1, 2]. DSS solidifies ferritically and then partially transforms to austenite. Proper weld metal chemistry and moderate cooling rates during welding promote a proper phase proportion. On the one hand, ferrite is more stable and with the existence of N, Cr-nitrides precipitate under high cooling rates [3, 4]. On the other hand slow cooling or prolonged heat-up duration increase the possibility of intermetallic precipitations like Sigma (σ) and Chi (χ) [5]. DSS has a very good stress corrosion cracking (SCC) and intergranular corrosion (IGC) resistance, and strength due to its ferrite content. However, ferrite content in excess of 70% in the weld metal and HAZ causes loss of toughness and increased susceptibility to IGC [6].

The competition and environmental concerns in the industrial manufacturing market require novel approaches in manufacturing processes, like more effective and non-conventional welding techniques. High-power-density welding provides high efficiency for fusion weldable materials like DSS. Keyhole welding allows for deep and narrow weldments and narrow HAZ with a high linear welding speed, which minimizes residual stresses and distortions of assemblies. Keyhole based welding methods, such as electron beam welding (EBW) and Laser beam welding (LBW) are generally utilized without the addition of a filler metal. Duplex welding filler wires and stick electrodes, which are employed during conventional arc welding methods, have usually additional Ni to stabilize the austenite phase. Autogenous welding of DSS yields weld metal very high in ferrite [3, 7, 8, 9]. Such weldments shall be quench-annealed in order to get the proper phase distribution. In order to alter the unbalanced γ to δ ratio in the fusion zone and HAZ of autogenous DSS welds, Laser or electron beam surface treatments have been employed as another technique to restore the correct γ to δ ratio [9, 10]. An addition of a small amount of nickel powder [11] or assist-charging of nitrogen into the fusion zone during Laser or electron beam welding may also restore the correct γ to δ ratio [12]. These post-weld treatments make the welding process more complicated and costly.

Beside metallurgical barriers to overcome, EBW and LBW require high precision assembly fit-ups, which is not easy in industrial manufacturing activities. Although through-thickness welds can be made rapidly in a single pass of EBW and LBW variations, small fit-up tolerances are still needed to avoid sagging and lack of fusion due to their small focused spot [13, 14]. Hybrid Laser arc welding (HLAW) promises filler metal transfer that also provides bridging capability for joint openings up to a millimetre [15, 16]. Another hybrid welding technique, hybrid plasma-gas metal arc welding (HPAW), utilizes a plasma arc instead of a Laser beam to form the keyhole, which is more capable in gap bridging [17], therefore less sensitive to fit-up deviations.

The recently developed HPAW system, which uniquely integrates a consumable wire electrode and a non-consumable tungsten electrode, was employed to join the plates of standard DSS grade 2205. The hybrid welding system takes advantage of combining the deep penetration characteristics of plasma arc welding (PAW) with the filler metal deposition capability of gas metal arc welding (GMAW). The technique has been successfully applied to non-alloyed steels and weldability features were previously published [18]. In order to provide benchmarking in terms of welding metallurgy, the same investigation methodology was applied on DSS plates welded by both conventional GMAW and autogenous PAW methods. Phase transformation and precipitation processes were evaluated with respect to weld heat input and cooling rate data recorded during welding performances. Hardness and impact toughness properties of as-welded material were discussed in terms of the microstructural characteristics of the fusion zone (FZ) and the heat affected zone (HAZ) of weldments.

The focus in the present study has been on the comparison of fatigue crack propagation behaviour of single-pass and multi-pass weldments of DSS. Before the investigations, effects of four different phenomena,

- residual stress,
- δ fraction,
- solute redistribution, and
- secondary phases,

were addressed in the hypothesis.

Thanks to its good gap bridging capability, improving the design of the weld bevel, HPAW has emerged as the only keyhole based welding method, which can provide proper ferrite/austenite phase balance in the fusion zone of weldment that is free from secondary austenite at the same time. Absence of the secondary austenite provided us an opportunity to investigate the role of the phase during fatigue crack propagation process in laboratory air and sour environments in a comparative methodology and on the basis of mechanical and physical metallurgy.

After a comprehensive research through the existing literature, the present work apparently has supplied pioneering experimental data on the controversial effect of secondary austenite

on the kinetics of fatigue fracture process, which is undoubtedly important for a damage tolerant design of joints in assemblies made of duplex stainless steel.

CHAPTER 2

THEORY

2.1. General

This chapter provides a theoretical background for,

- the hybrid welding process, as the process,
- DSS grade 2205, as the material, and
- the fatigue crack propagation phenomenon, as the property

and subjected to be investigated, under three different sections.

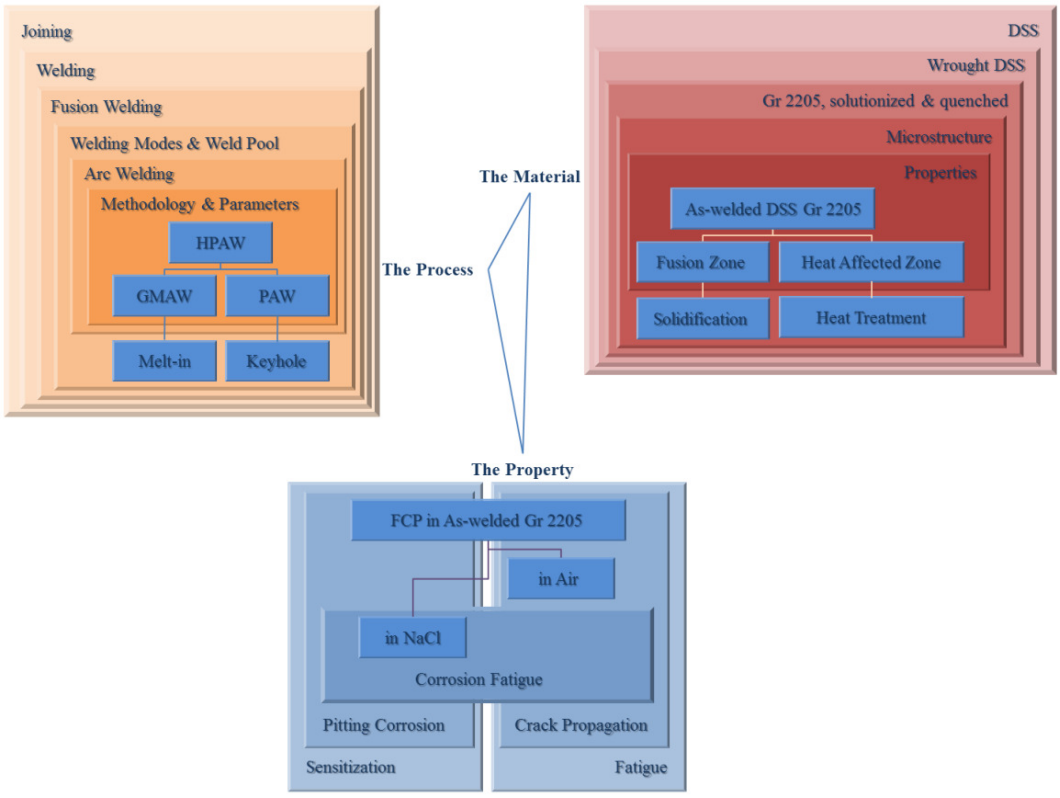

Figure 1. The structure of the Chapter including phenomena and interactions.

Basic welding and weldability concepts are introduced before giving the principles of hybrid plasma-gas metal arc welding in the first section (2.2). The second section (2.3) deals with the physical and mechanical metallurgy of DSS and its weldability in further details. The third section (2.4) begins with a description for the importance of investigation of fatigue crack propagation kinetics in weldments and continues describing underlying concepts of fatigue. In addition to generally accepted facts and figures, the text of the chapter has been enhanced by the inclusion of previous studies on these subjects. A map showing the phenomena and interactions through the Chapter is represented in Figure 1.

2.2. The Process; Hybrid Plasma-Gas Metal Arc Welding

Welding technologies have been improved through high-power-density and high-deposition-rate welding for fusion weldable alloys and solid-state welding for exotic alloys (Figure 2). As a high-power-density and high-deposition-rate welding process, keyhole based hybrid plasma-gas metal arc welding for high alloyed steels and fusion weldable super alloys and friction stir welding for exotic alloys are among primary research works in Welding Technology and Non-destructive Testing Research and Application Centre at Middle East Technical University.

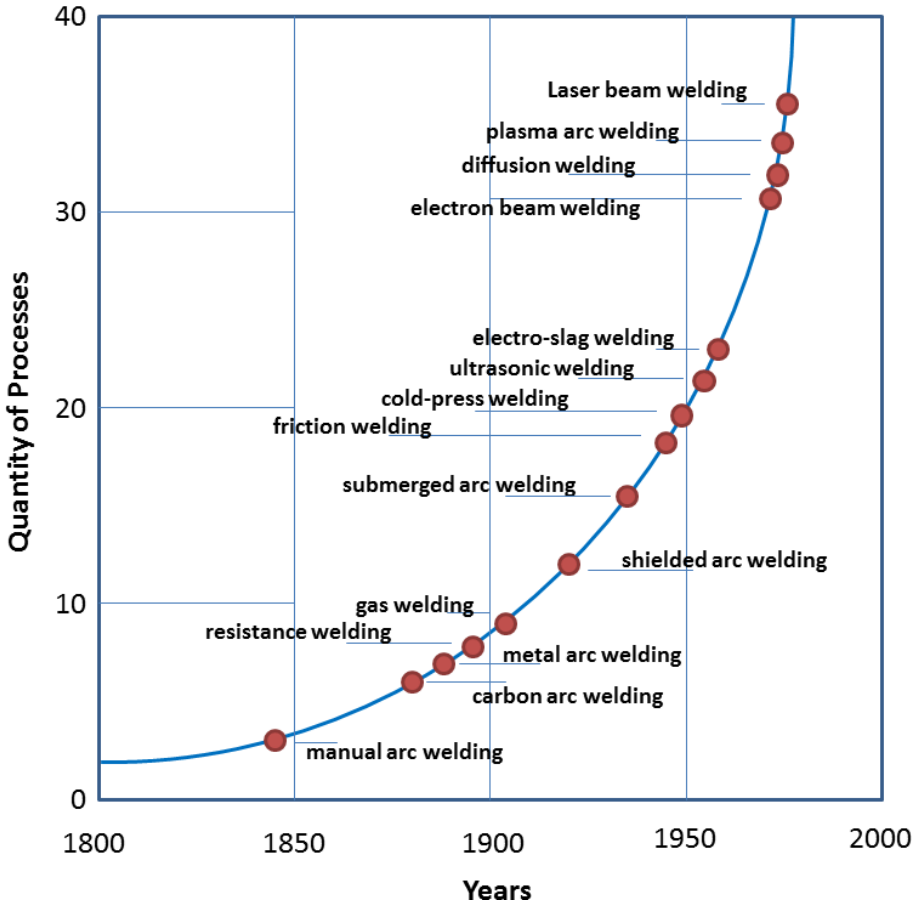

Figure 2. Inventions of welding techniques.

Hybrid plasma-gas metal arc welding (HPAW), which combines two conventional arc welding techniques, namely plasma arc welding (PAW) and gas metal arc welding (GMAW), will be described in this section. Before describing the principles of this hybrid welding technique, basic concepts of welding and weldability are introduced in the following sub-sections.

2.2.1. A Joining Process; Welding

DIN 8580 [19] classifies the manufacturing processes under following main groups:

- Group 1 – Forming,
- Group 2 – Deforming,
- Group 3 – Separating,
- Group 4 – Joining,
- Group 5 – Cladding,
- Group 6 – Modifying the Material Characteristics.

The present economic and competitive conditions impede the investments novel manufacturing technologies and constructing more efficient paths for manufacturing processes. Among all manufacturing processes, joining takes an extra attention in research and development activities.

Joining may be defined as the process of bringing two or more surfaces into intimate contact to establish continuity of a field across the resulting interface; for example structural joining denotes establishment of continuity of a stress field across an interface. Despite joints on metal structures may lead to metallurgically and mechanically weak zones, manufacturing massive industrial structures without joining would be costly, complicated and sometimes impossible.

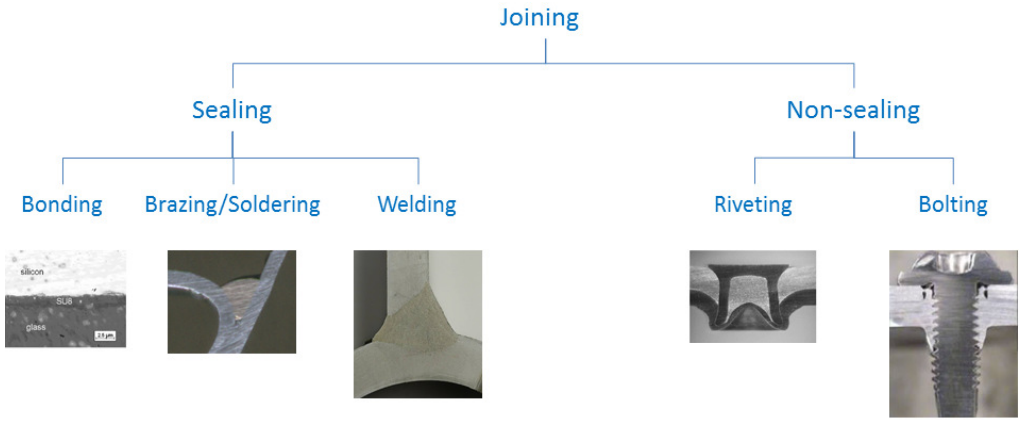

Figure 3. Classification of joining processes (Bonding picture [20], Riveting picture [21], Bolting picture [22]; Brazing/Soldering and Welding pictures are from studies of the author).

While joining engineers are in charge of optimizing the joining parameters in order to obtain metallurgically satisfactory joints, some design engineers have been interested in developing new technologies for such an important manufacturing process to let existing or new metal alloys, which are hard to join with conventional methods, be joined easily and effectively.

DIN 8580 defines the sub-groups of joining process as follows:

- Group 4.1 – Assembling,
- Group 4.2 – Filling,
- Group 4.3 – Pressing,
- Group 4.4 – Joining by forming,
- Group 4.5 – Joining by deforming,
- Group 4.6 – Welding,
- Group 4.7 – Soldering and Brazing,
- Group 4.8 – Bonding.

Figure 3 represents another approach to the classification of joining processes.

Welding is a necessary technique of joining, where sealing and strength are required. Welding is the uniting of materials in the welding zone by the application of heat and/or pressure. The heat introduced is adjusted to increase the temperature of the material, below or above its melting temperature. No matter whether the material is fused or not during the welding process, the temperature should be enough to activate diffusion mechanisms in between materials to be joined. The degree of diffusion makes the difference between welding and other sealing joining processes, such as soldering and brazing.

2.2.2. Fusion Welding and Weldability

Fusion welding is a joining process that relies upon fusion of materials of similar microstructures and melting points. Heat should be introduced to increase the temperature of the system above its melting point and form a weld pool. The heat can be generated by a flame, an arc, an electric resistance, a beam or an explosion under control.

Figure 4 shows the temperature-distance profile during a string-bead welding at a constant linear speed. As the heat source moves away from the location, it starts to cool down to the ambient temperature very rapidly. Therefore the temperature gradients are substantially higher than in casting processes.

Fusion welding is applied with or without the addition of a filler material. Welding is named as autogenous if it is applied without a filler material. If filler will be employed, it is designed to comply with the microstructure and consequently properties of the material couple, which is supposed to be welded. Addition of a filler metal results in a dilution of the filler and base materials. Therefore chemical composition of the filler is a principal determinant for the metallurgy of as-welded material, as well as the solidification rate of the weld pool.

Heat of fusion welding process not only melts the material, but also applies thermal cycles to the neighbourhood of the fusion zone. Such thermal cycles varies with respect to the distance from the fusion spot and creates a zone, called heat affected zone (HAZ), where the microstructure is altered. The extent and magnitude of microstructural alteration depends primarily on the heat transfer conditions. The base material, the filler material and the amount and concentration of heat input by the welding process determine the heat transfer conditions.

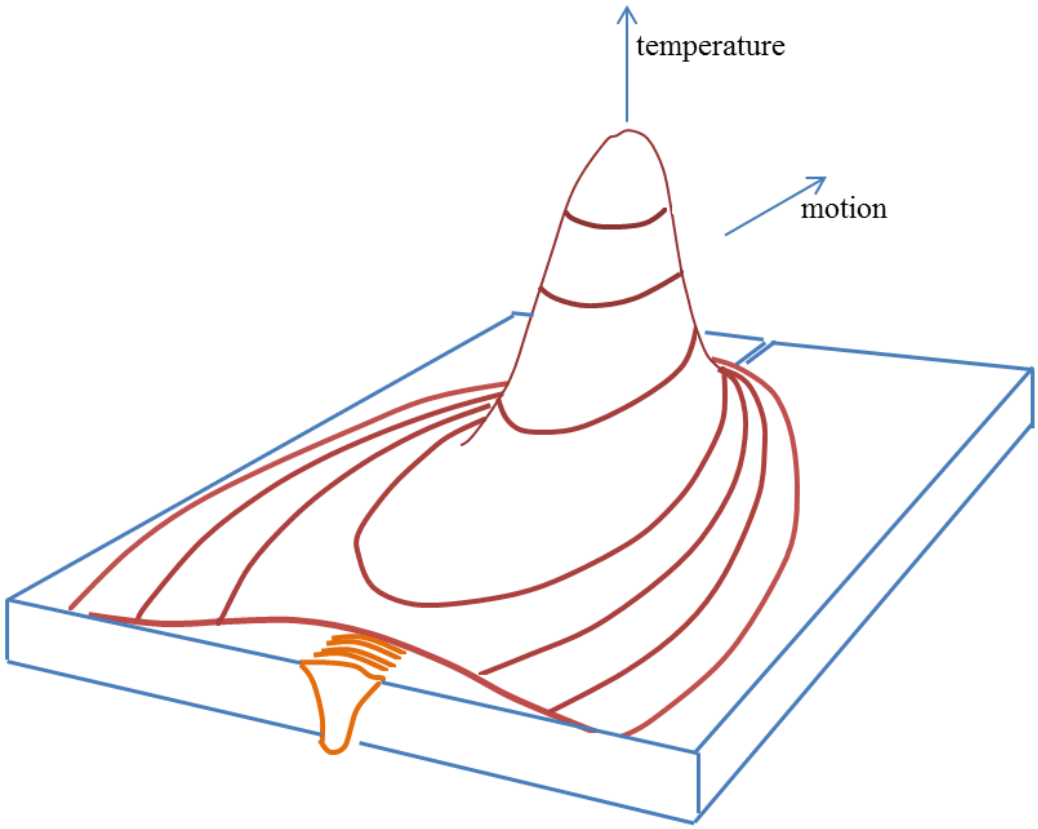

Figure 4. A general representation for the temperature profile during a fusion welding process. The maximum temperature is reached at the centre of the fusion zone.

Typical microstructures through a weldment are represented in Figure 5. The spot that reaches temperatures above the melting point of the material is called fusion zone (FZ). The fusion line experiences temperatures, where crystals can co-exist with the melt in thermodynamic equilibrium. In fact, the fusion line spans a zone, called partially melted zone (PMZ). Due to varying thermal cycles, microstructure and properties of the base material changes in various ways in individual sections of HAZ. The overheated section, coarse grained HAZ, directly adjoins the fusion line. The material in this section has been heated to a temperature, where coarse-grain annealing occurs. In the fine grained HAZ, normalization takes place, which causes a reduction in grain size. In the partially transformed zone, the metal has been heated to the temperatures, in which partial grain refining occurs.

A component consisting of metallic material is considered to be weldable by a given process when metallic continuity can be obtained by welding using a suitable welding method. At the same time the welds must comply with the requirements specified in regard to both their local properties and their influence on the construction of which they form a part. International Organization for Standardization (ISO) defines weldability in a standard [23] as: "Metallic material is considered to be susceptible to welding to an established extent with given processes and for given purposes when welding provides metal integrity by a corresponding technological process for welded parts to meet technical requirements as to their own qualities as well as to their influence on a structure they form."

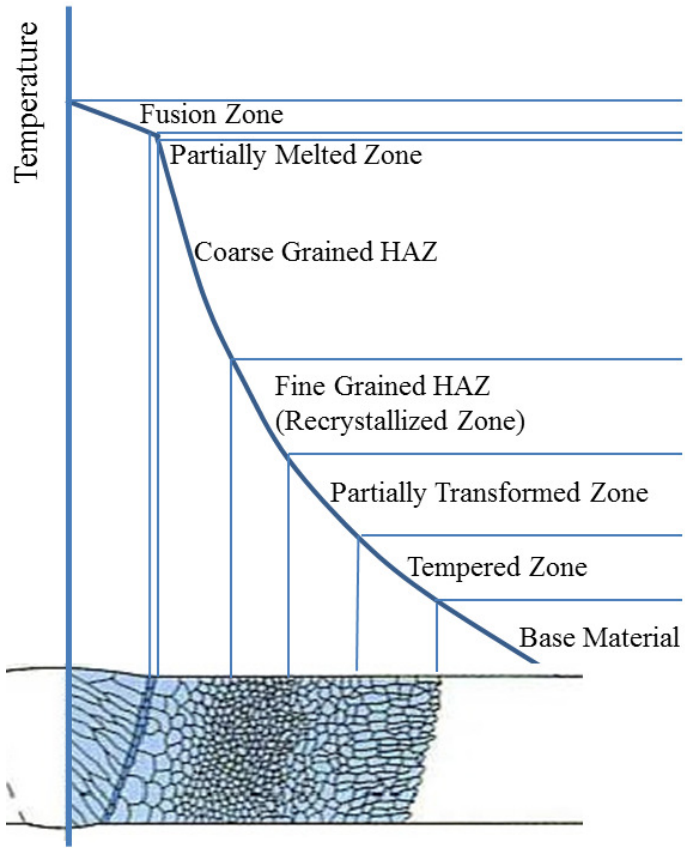

Figure 5. Typical microstructural features existing in the fusion zone, the partially melted zone and the heat affected zone (HAZ).

Weldability is influenced by four factors, namely material, type of construction (design), process and purpose, which have equal importance for weldability. Material influence on weldability can be detailed in three sub-definitions; chemical composition, microstructure and physical characteristics. Chemical composition of the material is generally responsible for the hardenability, ageing and weld pool convections.

Phase transformations, formation of grains and segregation can be considered as features of the microstructure. Physical and mechanical properties of the material, like thermal expansion and conductivity, strength and toughness, play also an important role as constituents of material characteristics.

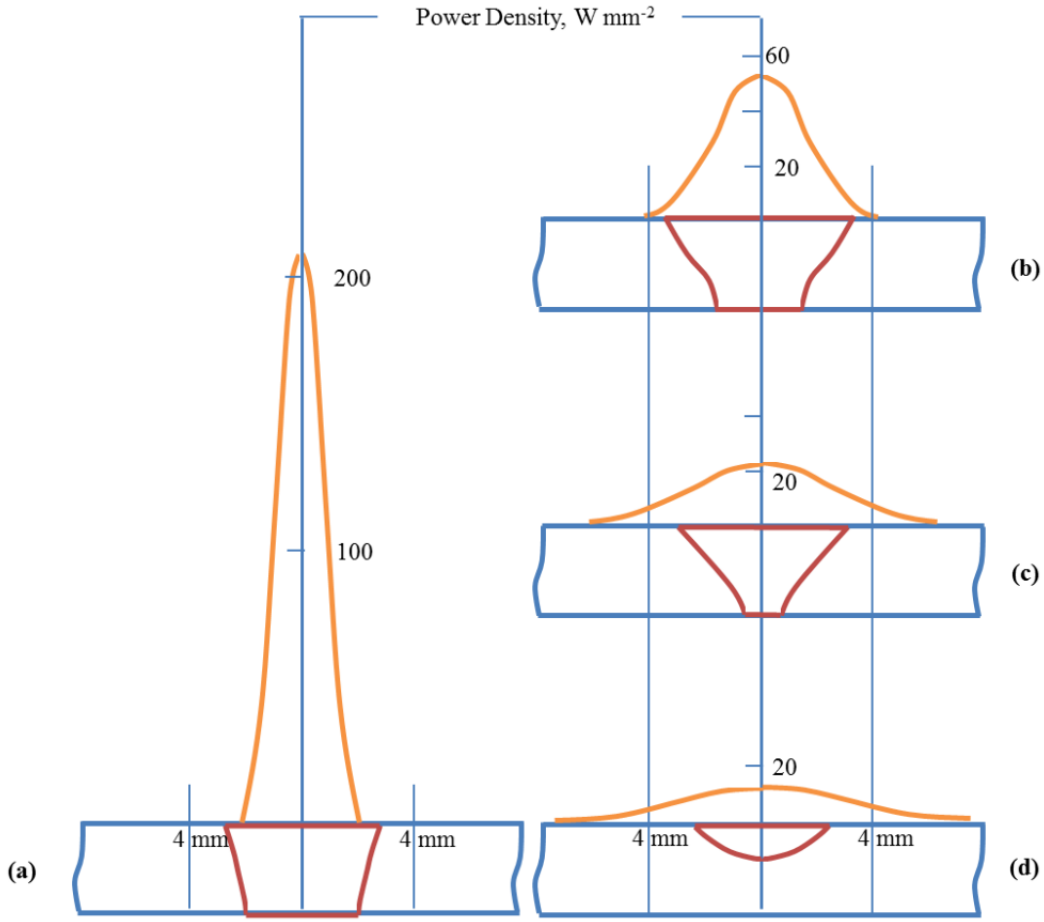

Figure 6. Illustration of the change in fusion effect (depth of penetration) with respect to the power density.

In addition to the material factor, weldability is also determined through the design of the assembly. Type, level, dimensions and rate of strain, distribution of the load and arrangement of joints in the assembly participates in the design factor. Environmental issues, such as temperature and corrosion, are other considerations. Welding technique, filler composition and type, other additives or auxiliaries, type of joint and bevel preparation, pre-heat conditions (pre-heating and inter-pass temperatures), specific point energy and the heat introduced by the welding process and post-weld treatments are main contributors of the process factor. Finally, quality requirements, in mechanical, physical and chemical senses, define the purpose factor.

2.2.3. Welding Modes and Weld Pool

Fusion welding generally operates in two different modes; conduction mode and keyhole mode. Conduction mode is also called as melt-in mode. During the conduction mode of welding, the heat supplied tends to diverge through the spacing between the source of heat and the work piece. Therefore the effective radius of energy distribution is high (power density is low) and consequently the fusion effect is limited to surface and sub-surface of the work piece. Whereas in keyhole mode of welding, the heat is focused to produce an incident power density at the surface of the work piece that creates a columnar vapour cavity surrounded by molten material. The effect of weld power density to form of the bead and depth of penetration can be seen in Figure 6. Power densities higher than 200 Wmm^{-2} lead to keyhole formation (Figure 6 a). Nevertheless, penetration effect gets less as the power density reduces for a constant welding power and an interaction time (Figure 6 b, c and d).

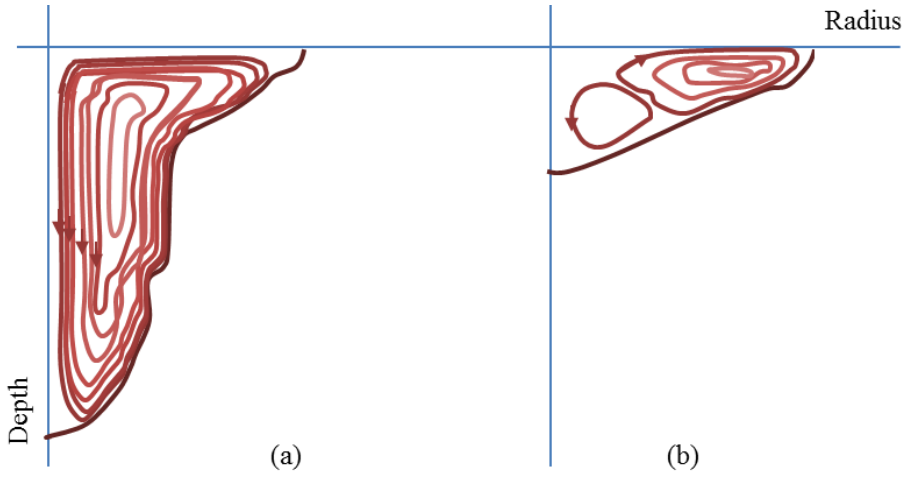

Figure 7. Illustrations for Marangoni (b) and reversed Marangoni (a) convections in weld pools (reproduced from the original figure [24]).

This cavity or keyhole is maintained during welding by equilibrium between the forces created by vapour pressure and those exerted by the surrounding molten material, where the gradient of surface tension of the weld pool is turned from negative to positive which is normally positive to negative in conduction mode of welding (Figure 7 b) [25, 26]. This effect leads to a reversed and more intensive turbulence, which leads towards the centre of the weld pool (Figure 7 a) [27].

2.2.4. Arc Welding

Arc welding, which is a fusion welding process, employs the heat of an electric arc that exists in between an electrode and the base metal in order to fuse the base and if necessary the filler metals. Welding electrodes may be fusible or non-fusible ones. Fusible electrodes have similar chemistry as the base metal and are utilized as filler to bridge the joint gap; so

they are consumed. Non-fusible electrodes are made of high-melting point metal alloys, such as pure tungsten and tungsten with oxide additives. Except a very small spot at the tip of the electrode, tungsten electrode is technically considered to not to be fused during welding operation. Since that they are also called as non-consumable electrodes.

Due to its high temperature, which is above the melting point of the metal at the fusion zone, the weldment should be protected from the ambient atmosphere in order to control the metallurgy of the zone during the welding process. During any arc welding process, oxygen and other atmospheric gases, like nitrogen, hydrogen, carbon-oxides, can react with the molten metal, causing defects or bad metallurgy that weaken the weld. Depending upon welding technique, a shielding gas or a flux is used to protect the weld pool and the HAZ. The structure of the arc and the way of shielding define the basis of the arc welding classification.

Basic arc welding techniques are presented in Figure 8 with their formal names and standard codes as per both American codes and European norms. International Standardization Organization abbreviates the techniques with both alphabetical and numerical codes.

Shielded metal arc welding (SMAW), also known as manual metal arc welding (MMA) is typically a manual arc welding process that uses a fusible electrode coated in flux to lay the weld. The technique is the first invented one among the arc welding methods. As the weld is laid, the flux coating of the electrode disintegrates, giving off vapours that serve as a shielding gas and providing a layer of slag, both of which protect the FZ and HAZ from atmospheric contamination. The coating flux may be basic, rutile or cellulosic character depending upon the application and quality requirements from the weldment.

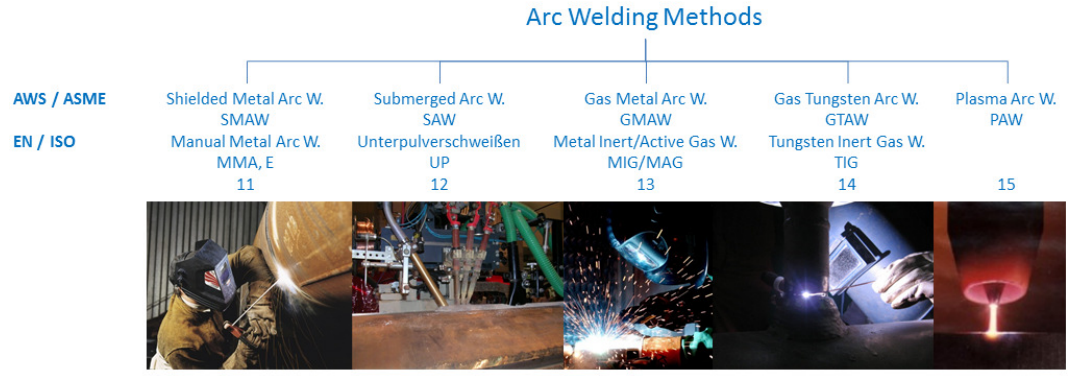

Figure 8. Classification of arc welding methods (SMAW, SAW and GMAW pictures were obtained from wikipedia.org).

Submerged Arc Welding (SAW) and Gas Metal Arc Welding (GMAW) methods require a mechanically fed consumable solid or tubular (flux cored) wire electrodes. Mechanical feeding was first proposed by Haughton in 1928 (Figure 9). Whereas FZ and HAZ are protected from atmospheric contamination by being "submerged" under a blanket of granular

fusible flux consisting of lime, silica and other ceramics compounds in the SAW operation, GMAW employs a gas or a gas mixture to shield the weld zones. Molten flux or shielding gas forms a plasma column that provides a path for a stable arc between the wire electrode and the base metal.

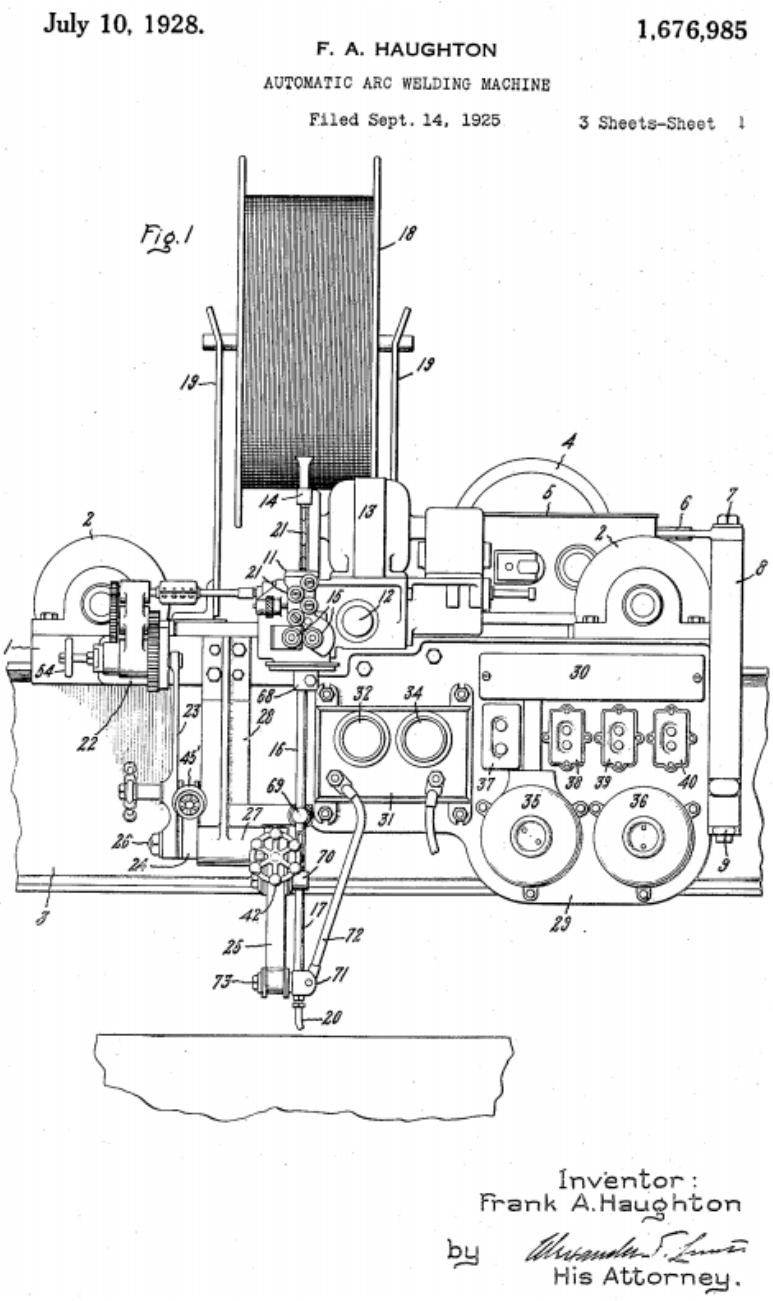

Figure 9. The automatic arc-welding machine, United States patent 1676985 by Frank A. Haughton in 1928 [28].

Contrary to the previous arc welding methods, Plasma Arc Welding (PAW) and its predecessor, Gas Tungsten Arc Welding (GTAW), use a non-fusible tungsten electrode

rather than a fusible electrode to form the arc. Filler may be or may not be employed during GTAW and PAW. Short arc length of GTAW, on one hand, requires a great care and skill to prevent contact between the electrode and the base metal, on the other hand, provides possibility to be adapted to high precision works. PAW was developed based on GTAW. It affords a constricted arc with the help of an orifice, which is at the tip of a copper nozzle. Constricting the arc increases its power density; consequently a deeper penetration can be obtained regarding to conventional arc welding techniques.

The primary function of a shielding gas or a flux is protecting the molten weld metal from atmospheric contamination and the imperfections because of the contamination. In addition to its shielding function, each gas or gas blend and flux has unique physical properties that have an effect on linear welding speed, penetration, dilution, seam appearance and form, and arc stability. During arc welding, the atmosphere in between the electrode and the base metal, and surfaces of the electrode and the base metal are dissociated and ionised to emit and receive charged particles, such as electrons and ions. The energy necessary to detach one electron from the atom is called energy of ionisation. Some examples for energies of the dissociation and the ionization during welding are represented in the equations, below [29]:

$$N_2 = N + N;\ N = N^+ + e^-, \quad (1)$$
$$H_2 = H + H;\ H = H^+ + e^-, \quad (2)$$
$$CO_2 = CO + O, \quad (3)$$
$$Fe = Fe^+ + e^- + 4.8\ eV \quad (4)$$
$$Al = Al^+ + e^- + 4.0\ eV \quad (5)$$

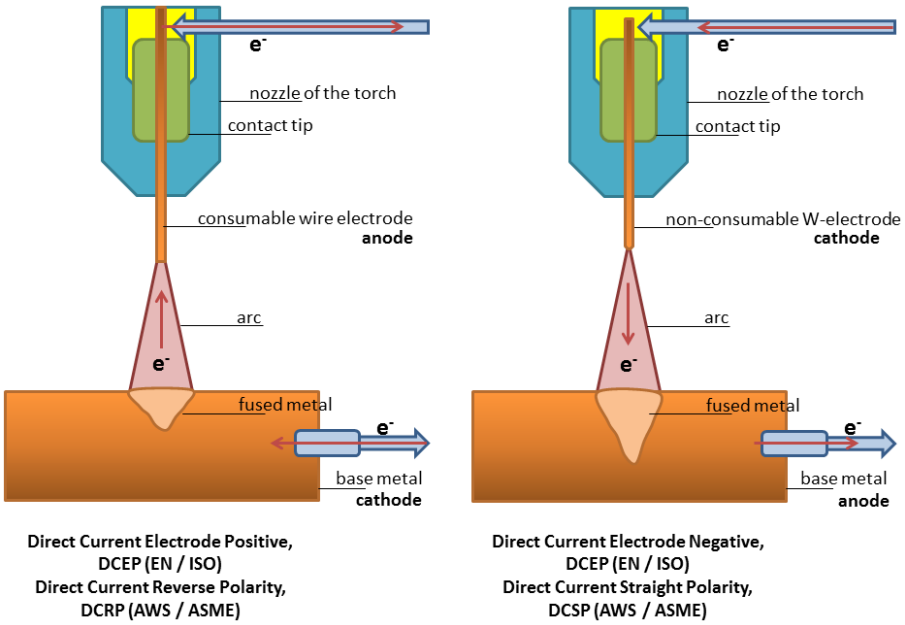

Figure 10. Two direct current (DC) polarization types during an arc welding process.

During arc welding, high temperatures are achieved. The temperature of the arc reaches to 6000 K during conventional arc welding processes. In the high density plasma arc in the

PAW process the temperature is about 30000 K [29]. At high temperatures, charged particles are detached directly from the metal lattice like the surface of the electrode and the base metal. The electrostatic field of the welding potential between the anode and the cathode is responsible for the moving direction. Movement and collision of dissociated and ionised particles form the arc.

The temperature at the anode side is usually higher than that at the cathode side for gas shielded arc welding processes. This temperature difference is usually used during a decision for the polarity. Figure 10 shows two different direct current polarization techniques during arc welding processes.

While arc welding processes such as GTAW and PAW use direct current electrode negative (DCEN) in order to provide a fusing priority to the base metal, GMAW introduces reverse polarity (DCEP) to let the wire melt easily in order to obtain a high metal deposition.

2.2.5. Arc Welding Parameters

Theory of action of the arc has been discussed extensively. A typical arc potential curve is shown in Figure 11. Ayrton [30] has shown that the relation between the current, I, flowing through the arc and the potential difference, U, across the arc can be expressed by the equation;

$$U = \alpha + \frac{\beta}{I} + (\gamma + \frac{\delta}{I})^2, \quad (6)$$

where α, β, γ and δ are constants. However, this definition may work for arcs in a few millimetres air gap and with low current amplitudes.

Ohm's law [31] is operable in current amplitude and potential relationship for the welding arc. The law states that the current amplitude is directly proportional to the potential difference across two points. In other words under constant potential, the amplitude of the arc current increases with decreasing resistance (Figure 12), and vice versa, according to the equation below:

$$V = I R, \quad (7)$$

where, V is the arc potential, I is the amplitude of arc current and R stands for electrical resistance of the arc.

During an arc welding process, if the arc length changes, then the electrical resistance of the arc changes according to the definition;

$$R = \rho L / A, \quad (8)$$

where, R is the arc resistance, ρ is the resistivity of the arc, L is the length and A is the cross-sectional area of the arc. In Figure 12, R_L, R_S and R_M stand for electrical resistances that

correspond to longest possible, shortest possible and medium arc lengths, respectively. If the tip of the electrode goes further away, the arc would be distinguished because the maximum possible potential difference would not be enough to keep the arc alive. Moreover, if the tip of the electrode gets closer than the shortest possible arc length, then the arc will be distinguished due to a contact of the electrode and the work piece, which means short circuiting.

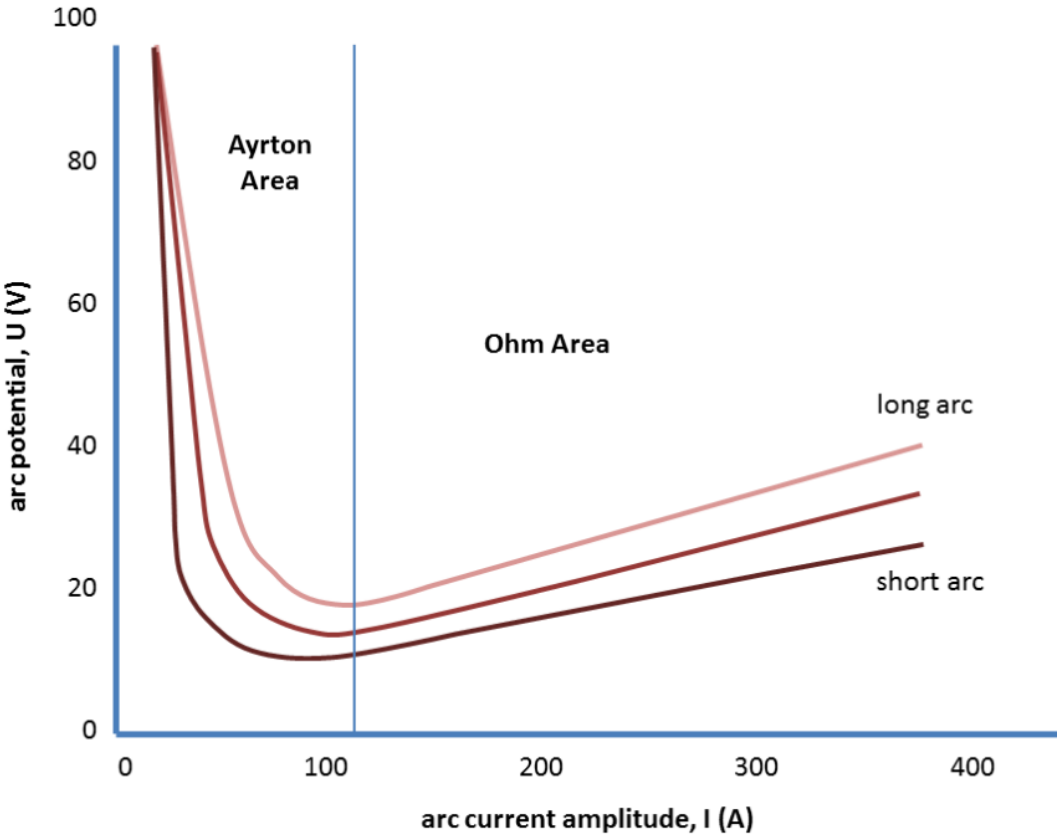

Figure 11. Graphical representation of the arc potential with respect to the current amplitude.

Since the arc is a consumer, an arc welding process requires a power supplier, which should particularly be designed for the welding method. Welding power suppliers generally have a transformer, which reduces the high voltage and increases the low current amplitude of the network, and a rectifier (diode), which transfers the alternating current (AC) to the direct current (DC).

Welding power suppliers are designed in two different potential versus current amplitude characteristics; namely constant potential (flat) and constant current (drooping) characteristics (Figure 13). In fact they are quasi-constant characteristics, which have been developed via microcontrollers. Quasi-constant current power suppliers are preferred for

manual welding techniques, such as SMAW and GTAW, in which keeping the current amplitude relatively constant is the principle concern to provide welder a short-term opportunity to fix what is wrong (position, welding power, linear welding speed etc.) during the operation. The power supplier has a relatively small change in current amplitude and consequently arc power for a corresponding relatively large change in arc potential or arc length, thus the name constant current.

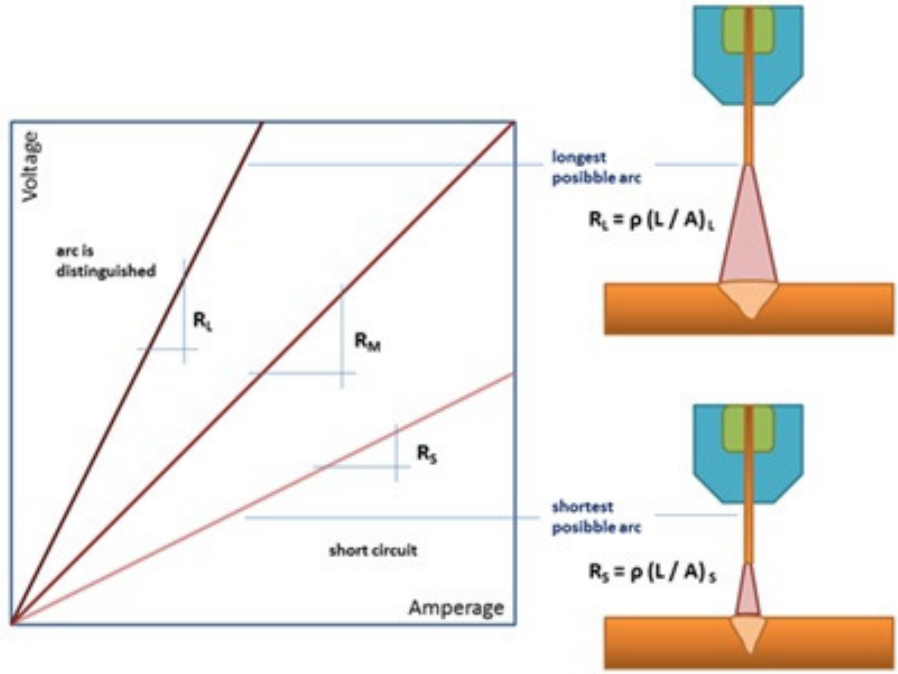

Figure 12. The relationship between the potential difference and current amplitude across the welding arc.

Figure 14 presents a proposed diagram illustrating welding process interactions and consequences of welding parameters in metallurgical and physical senses. In addition to the amount of welding power and its density, interaction time is also an important parameter, which defines weld pool convections, and so depth of penetration and heat transfer conditions. All these welding parameters consequently assembly two principal welding metrics, namely heat input and specific point energy [32].

The specific point energy, E, is calculated based on the equation;

$$E = \rho A t_i \quad (9)$$

where ρ is the power density, A is the area of the arc and t_i is the interaction time, which is calculated based on the equation;

$$t_i = \frac{\phi}{LWS} \tag{10}$$

where ϕ is the diameter of the arc and LWS is linear welding speed.

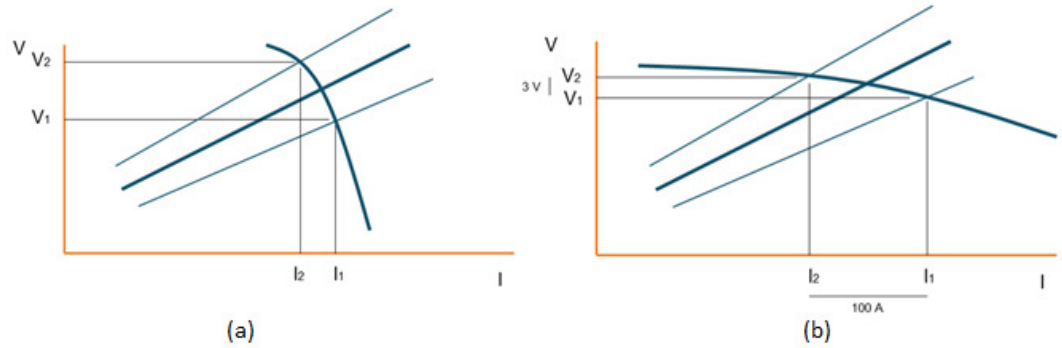

Figure 13. Two different static characteristics for welding power suppliers; (a) quasi-constant current, and (b) quasi-constant potential.

Geometry of the work piece and heat transfer coefficient of the material are determinants at the material side. In conduction mode of welding, heat input primarily determines the cooling rate at the process side. Heat input, H, by the welding process can be estimated using the following definition;

$$H = \frac{P}{LWS}\,\eta \tag{11}$$

where P is the welding power, which is a product of current amplitude in amperes and potential difference across the arc in volts and η is the efficiency factor (energy transfer efficiency for arc heat source - the ratio of the heat absorbed by the work piece to the welding energy) for a specific welding method. η is generally assumed 0.85 for GMAW and 0.60 for PAW [33, 34, 35, 36, 37].

2.2.6. Gas Metal Arc Welding

GMAW has been provided for relatively high speed and deposition rate. The method is particularly useful for vertical, inclined and overhead welds. A consumable wire electrode is fed through the tubular copper contact tip, which is placed in a welding torch having a nozzle surrounding the tip (Figure 15). Shielding gases is composed of inert and/or active gases, in which the constituents are designed specific to the material of the work piece. Gas mixtures consisting inert (Ar and He) and active gases (CO_2 and O_2) may be utilized for shielding of steels, whereas only inert atmospheres can be applied during welding of exotic alloys, such as aluminium, titanium, magnesium etc.

The electrical current is passed through the contact tip to the wire electrode and produces an arc and consequently heat that melts the end of the electrode into molten drops and the work piece. Molten drops are supplied to the weld deposit and fill the gap between pieces.

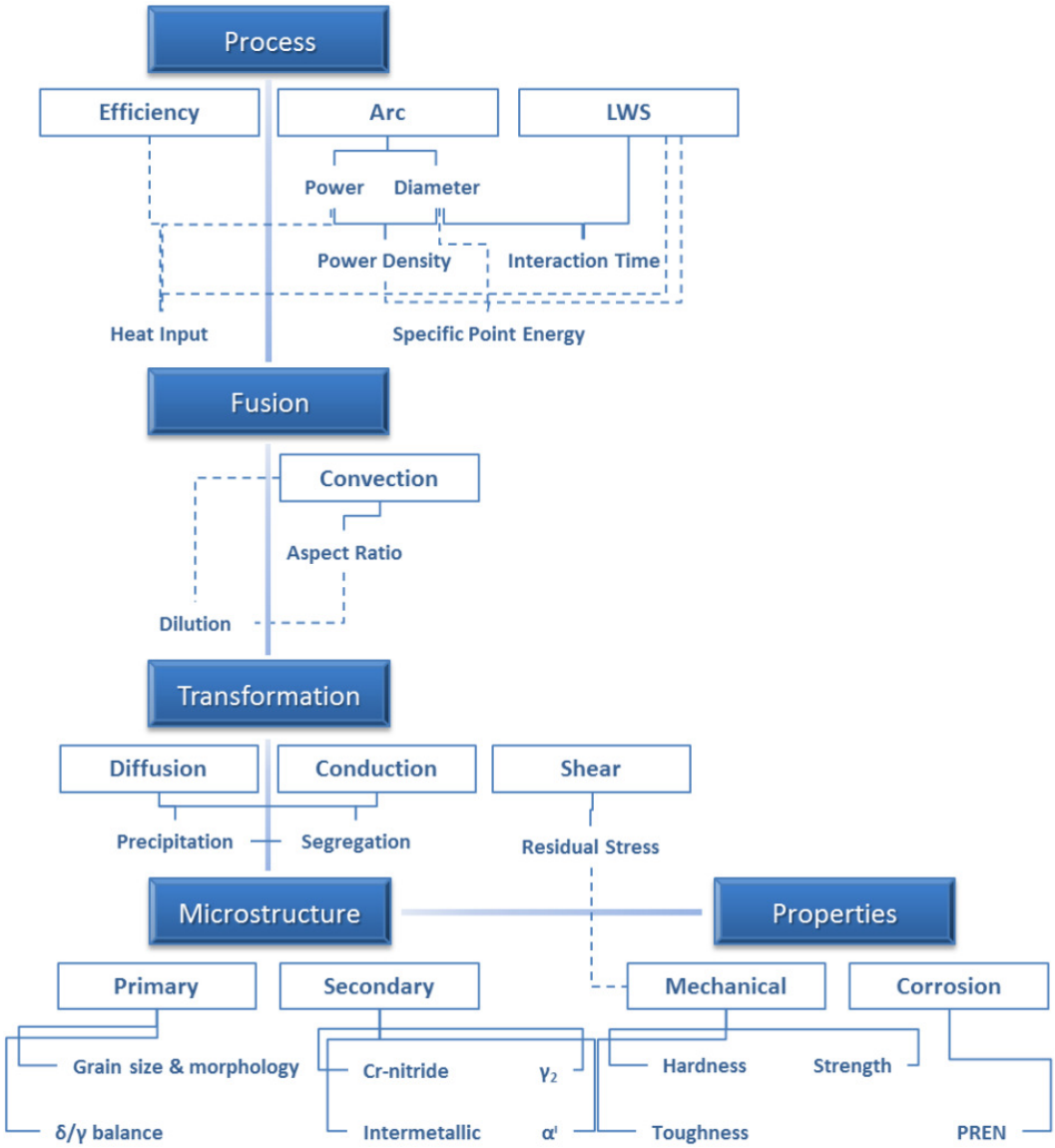

Figure 14. Welding process interactions and consequences of welding parameters.

Dynamic forces of multiple origins effect the detachment of molten metal droplet from the tip of the electrode [38]. Electromagnetic fields, surface tension, gravitation and vapour pressure are among these forces. There is metal vapour on the weld pool. Vaporized metal applies a pressure to the metal droplet, which is formed at the tip of the metal electrode. The pressure acts towards welding wire and tries to keep the droplet at the tip. Gravitation has also an effect on the droplet. Its effect depends upon the welding position. While gravitation helps the droplet fall down to the pool at the flat position, it tries to keep the droplet at the tip

of the wire at the overhead position. Electromagnetic field and the surface tension of the metal droplet are dominating factors on the metal transfer regime. The size of the droplet and its transfer mode are determined by these two factors.

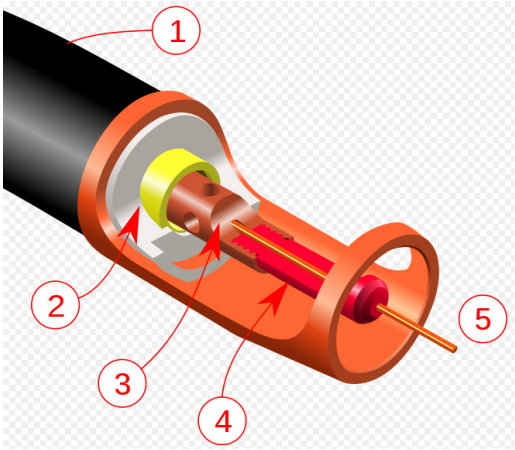

Figure 15. GMAW torch nozzle cut away image; (1) Torch handle, (2) Moulded phenolic dielectric (shown in white) and threaded metal nut insert (yellow), (3) Shielding gas diffuser, (4) Contact tip, (5) Nozzle output face [39].

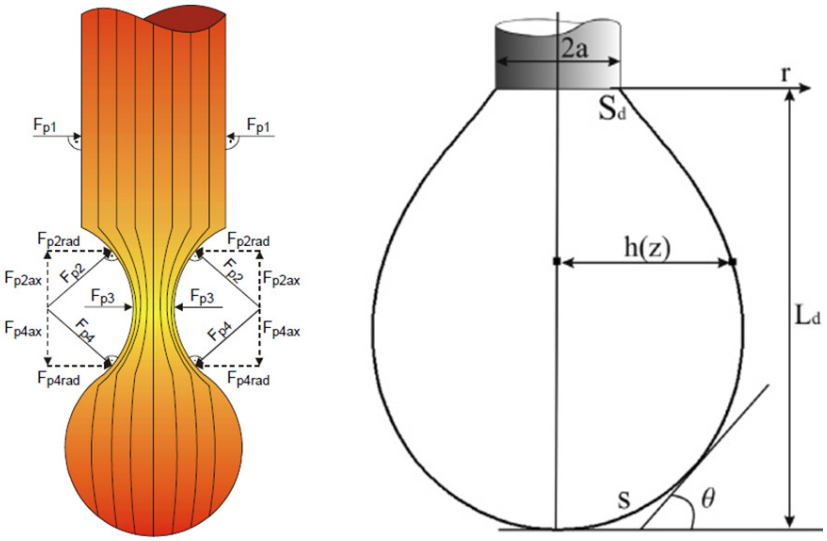

Figure 16. Lorenz forces (a) and the surface tension (b) on a metal droplet [40].

"Lorenz-force", which is provided by electromagnetic field, is also termed as pinch-force in welding terminology, since it creates a pinch effect on the neck of the droplet. The pinch

(Lorenz) force, F_P, is proportional to the square of the current amplitude, as in the following definition;

$$F_P = k\,\frac{P^2}{a}, \tag{12}$$

where a is the cross-sectional area of the wire and k is a constant. If other factors are considered to be constant, increasing welding power leads to an increase in the number of droplets that fall into the weld pool per unit time.

Welding power is not only responsible for the pinch forces, but also for the viscosity of the metal droplet. An increase in the temperature of the metal droplet due to a high welding power decreases the viscosity of the metal droplet, which provides a lower surface tension of the droplet. The shielding atmosphere is another factor that determines the surface tension (Figure 17). Using small amounts of active gasses as an addition to inert gases (2 – 5%) enhances the arc stability and reduces the surface tension of the molten metal droplet. It is possible to obtain small droplets by using gas mixtures that involve active constituent up to 25% due to this surface tension effect. Such gas mixtures are utilized for spray transfer welding of steels. Further increase in active gas content leads to higher surface tension and consequently formation of bigger droplets.

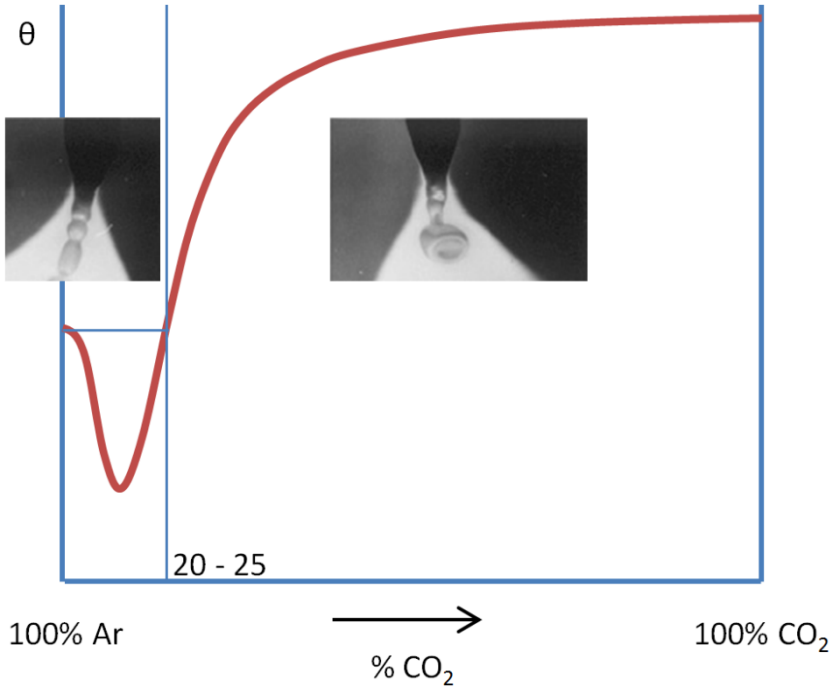

Figure 17. Effect of shielding gas composition on droplet surface tension and consequently the metal transfer mode.

Gas metal arc welding power suppliers have quasi-constant potential static characteristic. During a welding process, the voltage output remains relatively constant because of this

characteristic (Figure 13). As a result, any change in arc length results in a large change in current amplitude and therefore welding power. A shorter arc length than the optimum one causes less arc resistance, a higher current amplitude and welding power, which makes the wire electrode melt faster and thereby restore the original arc length in milliseconds. On the contrary, a longer arc length than the optimum one causes a higher arc resistance, less current amplitude and welding power, which makes the wire electrode melt slower and consequently again restore the original arc length (Figure 18). This process helps welder keep the arc length consistent.

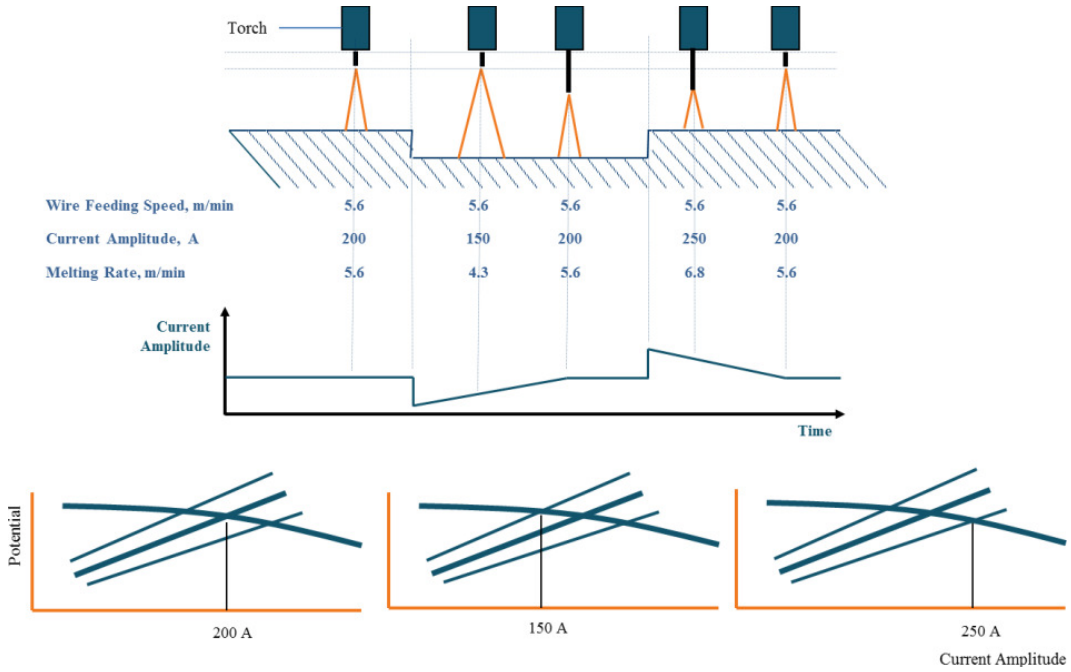

Figure 18. Illustration of the arc length self-correction process in GMAW.

2.2.7. Plasma Arc Welding

Plasma arc welding (PAW) is a development of the gas tungsten arc welding (GTAW) technique and it is relatively new [41, 42]. The method is designed to increase the productivity of GTAW. PAW provides some advantages such as good root contour, increased linear welding speed, and less heat input compared to other arc welding techniques.

Generally PAW is preferred to be utilized in keyhole mode, in which the base metal is penetrated completely and a hole is formed at the point of welding that is carried along during the welding process (Figure 19). Compared to the conventional GTAW arc, the constricted plasma arc has a much lower divergence, therefore larger changes in arc length can be tolerated and power density is relatively high. Due to its high power density, aspect ratio of the weldments obtained by plasma arc welding is relatively high if it is utilized in

keyhole mode with transferred arc. The correlations between the keyhole PAW process parameters and energy distribution, melting efficiency and weld form have been extensively studied by Tomsic and Jackson [43]. It is also possible to use the technique in conduction (melt-in) mode of welding.

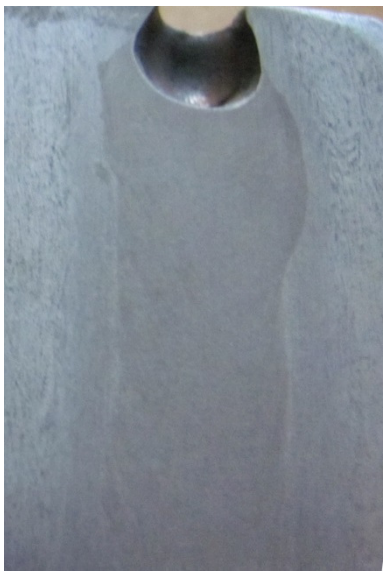

Figure 19. Grinded and polished top surface of a weldment that was obtained using HPAW; the keyhole left at the end of the weldment can be seen at the end of the seam.

High power density of the technique is achieved by concentrating the plasma inside of a narrow jet. The constricted plasma jet is obtained by an additional copper nozzle, which has a small orifice, in the main shielding gas nozzle. Two different gases are blown rather than one gas as in other gas shielded arc welding techniques. Interior gas is called orifice or plasma gas, which should be exclusively inert like argon, helium or a mixture of these two gases to protect the tungsten electrode from oxidation. Shielding gas is blown through the outer nozzle and this may be inert or active gases depending upon the material to be welded. The tungsten electrode has usually negative polarity (DCEN) as in GTAW.

2.2.8. Hybrid Plasma-Gas Metal Arc Welding

A plasma arc offers a good opportunity for joining thick and weldable materials in a single run with high linear welding speeds. It is more suitable for massive industrial manufacturing than Laser or electron beams due to its relatively wider spot size, which is capable of bridging relatively wide fit-up gaps. Combining a plasma arc with a wire arc, which deposits metal to the bevel, was a good solution for high-alloyed steels that require some degree of dilution to be able to obtain a good microstructure in the weld metal.

Hybrid plasma arc welding (HPAW) combines both the deep penetration capability of plasma arc welding and the metal deposition capability of gas metal arc welding in a single

torch. HPAW provides less consumption of filler and energy during welding and less distortion and/or residual stresses in the welded structures than conventional techniques.

HPAW has significant advantages compared to other high-power-density welding techniques, such as Laser beam welding, hybrid laser arc welding and electron beam welding in heavy industrial manufacturing, because it requires neither special environments nor high-precision fit-up and manipulation.

However welding procedure design is still important for obtaining a proper microstructure, which will provide good physical and chemical properties to materials, especially the ones, which are highly alloyed, in order to maintain their superior properties.

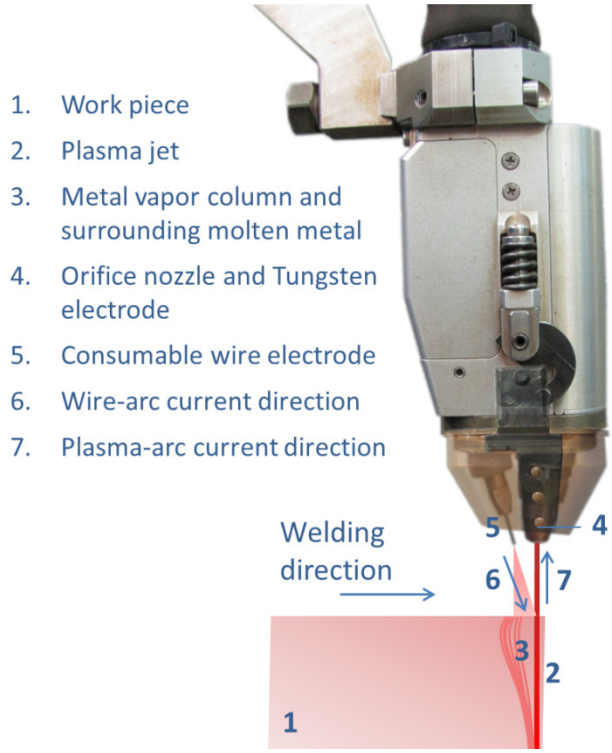

Figure 20. The hybrid plasma-gas metal arc welding system, SuperMIG, was designed by Dykhno and Ignatchenko [44].

2.3. The Material; Duplex Stainless Steel Grade 2205

DSS offers an alternative to austenitic stainless steels in many fields of application, such as chemical, oil, and gas industries like pipelines and reaction vessels. The unique combination of two phase structure of δ-ferrite and austenite offers a good combination of strength and corrosion resistance. Ferrite phase introduces strength and local corrosion resistance to the material, whereas ductility and general corrosion resistance comes from the austenite phase. Therefore, duplex stainless steels have high impact toughness and overall corrosion resistance. Furthermore, their relatively low thermal expansion coefficient makes them

useful for shell and tube heat exchangers, and the improved stress corrosion cracking resistance in chloride containing environments of temperatures above - 50°C and below 250°C.

2.3.1. Development and Grades of Duplex Stainless Steels

Development of stainless steels goes back to the first decades of the 20th century in UK and Germany. First stainless steel grades were only rich in Cr. Following inventions of martensitic and ferritic grades, austenitic grades were developed by Ni alloying and became the most popular stainless steel grades.

The first reference to ferritic-austenitic structure was recorded in 1927 [45]. The first commercial DSS alloy 453E (25% Cr – 5% Ni) was designed by Avesta Jernverk in 1929, however an unintentionally produced grade (20% Cr – 8% Ni – 2.5% Mo) by a French company, J. Holtzer, in 1933, during production of an austenitic grade (18% Cr – 9% Ni – 2.5% Mo) is found to be the most significant because analysis of this casting had found that this alloy was not sensitive to intergranular corrosion (IGC) in various corrosive media due to its relatively higher volume fraction of ferrite in an austenitic matrix with respect to austenitic stainless steel grades [46].

Nickel shortage promoted new duplex designs during 1950s, but a real impact came in 1970s, after the introduction of AOD refining process, which leads to a better control of alloy chemistry including oxygen and sulphur, and consequently a better weldability. 22% Cr standard grade was developed in Germany and Sweden. Higher alloyed DSS grades began to be produced in 1980s. While standard DSS grades have pitting resistance equivalent numbers (PRE_N) of 35, super DSS grades have PRE_N higher than 40, where:

$$PRE_N = \%Cr + 3.3\,\%Mo + 16\,\%N, \tag{12}$$

Due to tungsten alloying to some grades of super DSS a modified PRE definition can also be utilized, namely:

$$PRE_W = \%Cr + 3.3\,(\%Mo + 0.5\,\%W) + 16\,\%N, \tag{13}$$

2.3.2. Wrought DSS

DSS possesses bi-phase microstructure consisting almost equal percentages of δ-ferrite and austenite. The material can be provided in as-cast and wrought forms. Both grades have been increasingly employed for a variety of application, such as heat exchangers (the tubes and the case), pressure vessels, storage tanks, desalination systems, rotators, impellers, shafts, construction and piping assemblies in off-shore platforms, digesters and other equipment in the pulp and paper industry, chemical tankers and reaction vessels Figure 21. ASTM standards for DSS products can be seen in Table 2.

2.3.3. Grade 2205

22% Cr standard DSS grade (2205) was developed in the early 1970s. It has soon found widespread use owing to insensitivity to IGC upon welding because of the balanced microstructure especially due to nitrogen (N) addition. Today, even after development of other higher alloyed DSS, grade 2205 keeps its popularity due to its optimum pitting corrosion resistance to price parameter. Nevertheless, beside its price and performance, grade 2205 is interesting for research and development activities because its relatively less complicated microstructure provides basic physical and metallurgical information for other grades as well.

Figure 21. Some applications where DSS is employed; manufacturing of a column (reaction) vessel in GAMA Industrial Manufacturing and Erection Co.(upper left, from the author's collection), a heat exchanger (upper right), an off-shore-plant (photo taken by Øyvind Hagen, Statoil).

In wrought grades, the balanced microstructure, which is free from any secondary phases, are obtained by a proper alloying and solution annealing followed by quenching. Wrought grades have typical rolling texture because of hot rolling process before the heat treatment.

2.3.4. Microstructure

Chromium (Cr), nickel (Ni), molybdenum (Mo) and nitrogen (N) are most important constituents in the grade 2205, which affect the microstructural features and consequently properties of the material.

On one hand Cr and Mo in the steel are in charge of improving the localized corrosion resistance by the formation of passive oxy-hydroxide films [47, 48]. They extend the passive range and reduce the rate of corrosion. They increase the pitting resistance of the material [49]. On the other hand they enhance precipitation of intermetallics, such as sigma (σ) and chi (χ) phases, if the steel is alloyed with them more than certain compositional upper limits. They both are ferrite (δ) stabilizers, whereas Ni and N stabilize the austenite (γ). In order to maintain the phase balance, δ stabilizing elements are balanced with Ni and N. However, if Ni and N contents exceed a certain level, then volume fraction of γ increases well above 50%, with the consequence that Cr and Mo are enriched in the δ grains. This makes δ transformation to undesirable intermetallic phases, such as sigma (σ) and chi (χ), favorable when the material is exposed to temperatures 650 – 950°C [1, 5, 50]. Spinodal decomposition of δ due to excessive Ni [51] and precipitation of Cr-nitrides due to excessive N [52] are other problems during thermal treatments of the alloy. Whereas Ni does not have a direct effect on corrosion properties, N increases pitting and crevice corrosion resistance by moving the electro potential in the noble direction.

Stainless steels solidify as either γ or δ. Primary crystallization is classified in 5 different modes from “a” to “e” according to Cr_{eq}/Ni_{eq} ratio of the material (Figure 22). During solidification, DSS is first solidifies as δ (Figure 23). The solid state transformation is diffusion controlled [53]. γ is Ni and N enriched whereas Cr and Mo are found in δ. The nucleation rate of γ in δ is very high. However, transformation could not take place until the sufficient nuclei form at around 1150°C. The relations between the nucleation rate and austenite fraction with temperature are given in **Error! Reference source not found.**. The formation of γ crystals occurs at δ grain boundaries, where Ni is rich and Cr is depleted due to segregations during the solidification. Reconstructive (diffusive) δ to γ phase transformation continues taking place down to the temperatures about 450°C, where diffusion significantly slows down in equilibrium conditions.

The diagram in Figure 23 illustrates that the chemical composition of δ and γ will be different depending on the temperature. This is about the solubility limits for these elements. Partitioning of elements is one of the driving forces of secondary transformations during thermal treatments. Most of these transformations take place within δ, because diffusion rates of elements in BCC lattice are almost 100 times faster than the rates in FCC lattice of γ.

Table 1. DSS grades with their nominal chemical compositions in weight percentages; italics are maximum permissible values.

	UNS	C	Si	Mn	P	S	Cr	Ni	Mo	Cu	W	Co	N	$PRE_{N/W}$
Lean	S31500	*0.03*	*2.0*	*2.0*	*0.030*	*0.03*	18.0-19.0	4.25-5.25	2.50-3.00	-	-	-	-	23
	S32304	*0.03*	*1.0*	*2.5*	*0.040*	*0.04*	21.5-24.5	3.0-5.5	-	0.05-0.60	-	-	0.05-0.20	25
	S32404	*0.04*	*1.0*	*2.0*	*0.030*	*0.01*	20.5-22.5	5.5-8.5	2.0-3.0	1.0-2.0	-	-	0.20	31
Standard	S31803	*0.03*	*1.0*	*2.0*	*0.030*	*0.02*	21.0-23.0	4.5-6.5	2.5-3.5	-	-	-	0.08-0.20	34
	S32205	*0.03*	*1.0*	*2.0*	*0.030*	*0.02*	22.0-23.0	4.5-6.5	3.0-3.5	-	-	-	0.14-0.20	35
High Alloy	S31200	*0.03*	*1.0*	*2.0*	*0.045*	*0.03*	24.0-26.0	5.5-6.5	1.2-2.0	-	-	-	0.14-0.20	38
	S31260	*0.03*	*0.8*	*1.0*	*0.030*	*0.03*	24.0-26.0	5.5-7.5	2.5-3.5	0.2-0.8	0.1-0.5	-	0.10-0.30	38
	S32550	*0.04*	*1.0*	*1.5*	*0.040*	*0.03*	24.0-27.0	4.5-6.5	2.9-3.9	1.5-2.5	-	-	0.10-0.25	38
	S32900	*0.08*	*0.8*	*1.0*	*0.040*	*0.03*	23.0-28.0	2.5-5.0	1.0-2.0	-	-	-	-	33
	S32950	*0.03*	*0.6*	*2.0*	*0.035*	*0.01*	26.0-29.0	3.5-5.2	1.0-2.5	-	-	-	0.15-0.35	36
Super	S32520	*0.03*	*0.8*	*1.5*	*0.035*	*0.02*	24.0-26.0	5.5-8.0	3.0-5.0	0.5-3.0	-	-	0.20-0.35	41
	S32750	*0.03*	*0.8*	*1.2*	*0.035*	*0.02*	24.0-26.0	6.0-8.0	3.0-5.0	0.5	-	-	0.24-0.32	41
	S32760	*0.03*	*1.0*	*1.0*	*0.030*	*0.01*	24.0-26.0	6.0-8.0	3.0-4.0	0.5-1.0	0.5-1.0	-	0.20-0.30	>40
	S39226	*0.03*	*0.8*	*1.0*	*0.030*	*0.03*	24.0-26.0	5.5-7.5	2.5-3.5	0.2-0.8	0.1-0.5	-	0.10-0.30	>40
	S39274	*0.03*	*0.8*	*1.0*	*0.030*	*0.02*	24.0-26.0	6.0-8.0	2.5-3.5	0.2-0.8	1.5-2.5	-	0.24-0.32	42
	S39277	*0.03*	*0.8*	-	*0.025*	*0.002*	24.0-26.0	6.5-8.0	3.0-4.0	1.2-2.0	0.8-1.2	-	0.23-0.33	42
Hyper	S32707	*0.03*	*0.5*	*1.5*	*0.035*	*0.01*	26.0-28.0	6.5	4.8	-	-	1.0	0.40	49

Table 2. ASTM standards for products made of DSS.

Grade	Seamless and welded tube and pipe	Flanges	Fittings	Plate, sheet and strip	Bar	Forgings
2304	A789, A790	-	-	A240	-	-
2205		A182	A182, A815		A276, A479	A182
2507					A276	
2707		-	-	-	-	-

Secondary phases may have detrimental effects on mechanical and corrosion properties of DSS. Cr-nitrides (Cr_2N and CrN), intermetallic σ and χ phases, Cr-rich ferrite (α') and secondary austenite (γ_2) are most important secondary phases as far as the grade 2205 is considered. Secondary phases may precipitate at the grain boundaries and in δ grains in the temperature range between 300 and 1100°C.

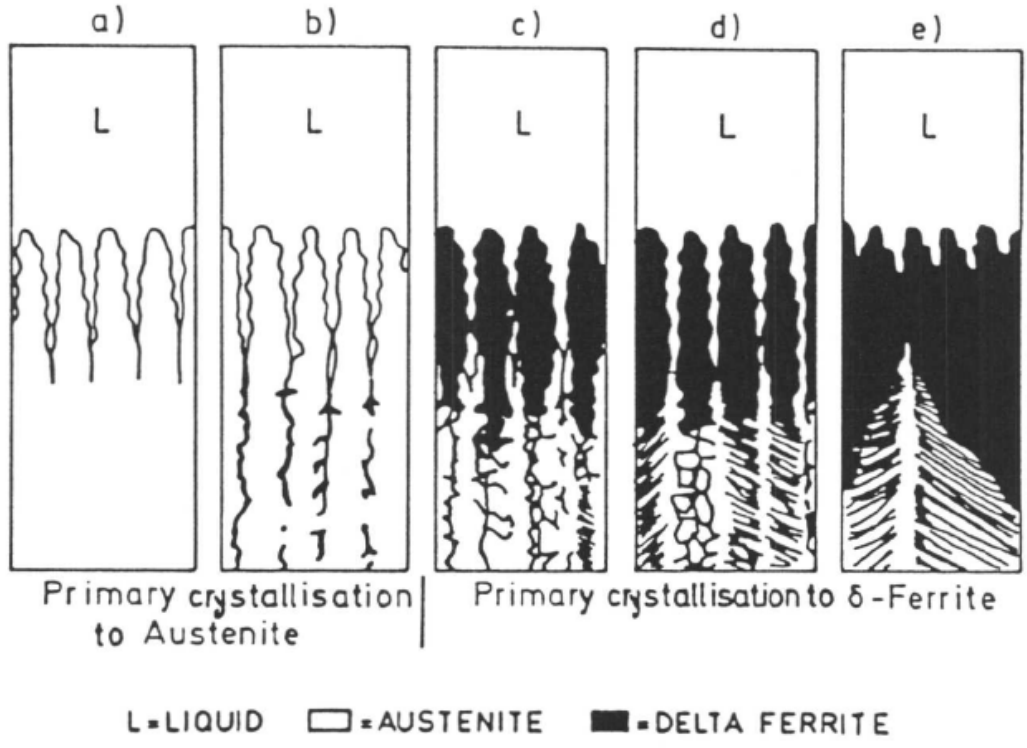

Figure 22. The schematic representation of the crystallization modes of stainless steel weld metal according to Kujanpää et al. [54]. Mode a and b primary crystallization to γ and modes c to e primary crystallization to δ.

N solubility in δ is relatively high at high temperatures. However its solubility drops as the material cools down and δ grains may be supersaturated in N depending upon the cooling rate. Cr-nitride does not normally precipitates after solution annealing treatment; however FZ and HAZ of weldments are prone to nitride precipitation due to rapid cooling from single phase regions [55]. Cr_2N formed in HAZ has been stated to affect corrosion resistance of DSS [56].

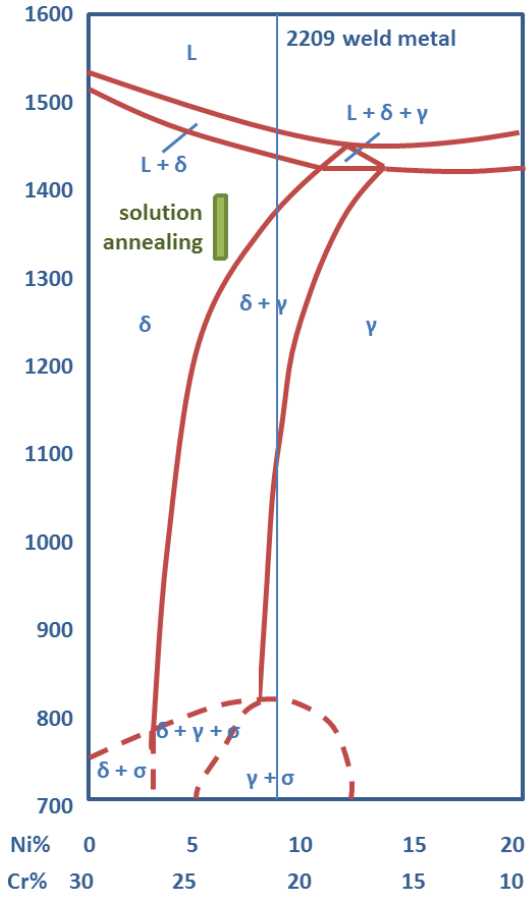

Figure 23. Ternary Fe-Cr-Ni constitution diagram at 70% Fe.

Cr and Mo enriched ferrite promotes the formation of intermetallic phases at temperatures around 500-900°C, which are very detrimental to the mechanical properties and the corrosion resistance of the duplex stainless steels. Cr and Mo rich σ-phase is a hard precipitate that leads to embrittlement to the material. At about 900°C, ferrite decomposition to σ may take a couple of minutes especially in super DSS. When δ transforms to γ or γ_2, retained δ becomes enriched in Cr and Mo and this promotes σ formation, which progresses through the destabilized δ.

Spinodal decomposition of α' occurs between the temperature range 300 and 525°C. Decomposition of δ is considered to be the reason of hardening and 475°C-embrittlement.

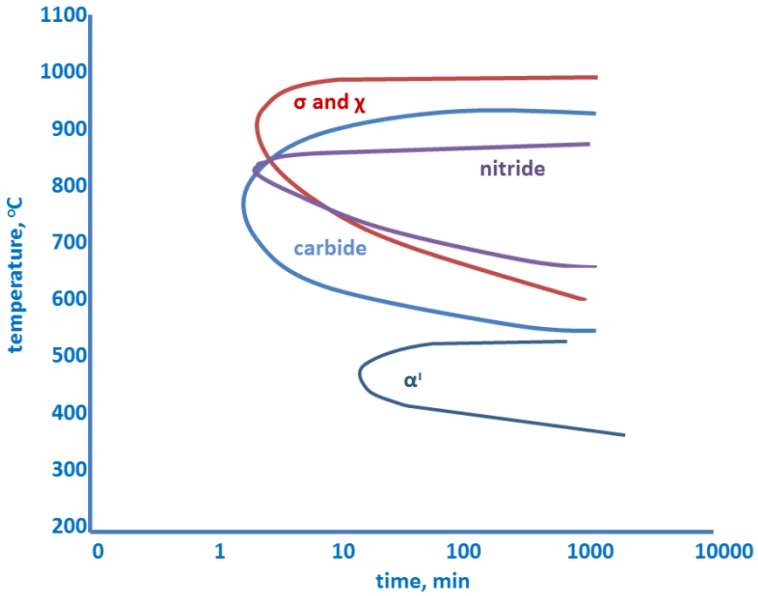

Figure 24. Continuous cooling transformation diagram of DSS Gr 2205.

2.3.5. Properties

Mechanical properties of duplex stainless steels are very good especially compared to austenitic stainless steels. The typical mechanical properties are summarized in Table 4. Mechanical properties of SAF duplex stainless steels.

The yield strength of duplex stainless steels is very high than that of austenitic steels. The high strength introduced by the δ-ferrite phase, yet the strength of DSS is also higher than that of ferritic stainless steels. Therefore, it can be concluded that the duplex microstructure contributes to the high strength since there exists a mutual hindering of the growth of grains leading to a fine grain structure. Furthermore, nitrogen in austenite gives rise to interstitial solid solution hardening, and this may cause to austenite having a higher strength even than δ-ferrite. The overall high strength of DSS can be linked to the presence of δ-ferrite phase, small grain size, formation of hard secondary austenite, and interstitial and substitutional solution hardening. Away from the microstructural features, cold deformation can improve the yield strength, tensile strength, and hardness of the duplex stainless steels, while it reduces the elongation slightly.

A smaller grain size and a two phase austenitic ferritic microstructure that prevents grain growth, gives Sandvik duplex stainless steels increased toughness and strength (in particular, very high proof strength). Figures in the table below apply to material in the solution annealed condition at 20ºC.

Table 3. Crystallographic data for various phases that possibly exist in DSS

Phase		Nom. Chem. Formula	%Cr	%Ni	%Mo	Formation T, °C	Formation Location	Lattice Type	Lattice Parameter, Å	Space Group
Ferrite	**Δ**	-	27.4	8.7	4.0		-	Cubic	2.86 – 2.88	Im3m
Cr-rich ferrite	**α'**	-	65	2.5	13	300-525	δ	Cubic	2.877	Im3m
(Primary) austenite	**γ (γ_1)**	-	26.6	9.6	3.3	< 1250	δ	Cubic	3.58 – 3.62	Fm3m
Secondary austenite	**γ_2**	Type 1	same as δ			< 650	δ	Cubic		
		Type 2	24.3	11	3.4	650-800	δ and δ/γ			
		Type 3				700-800	with σ			
Sigma	**Σ**	Fe-Cr-Mo	30	4	7	600-1000	δ/γ	Tetragonal	8.79 / 4.54	$P4_2/mnm$
Chi	**X**	$Fe_{36}Cr_{12}Mo_{10}$	25	3	14	700-900	δ/γ	Cubic	8.86 – 8.92	I43m
Laves	**R**	Fe_2Mo	25	6	35	550-650	δ and δ/γ	Rhombohedral	10.90 / 19.34	R3
Pi	**Π**	$Fe_7Mo_{13}N_4$	35	3	34	550-600	δ	Cubic	6.47	$P4_132$
Cr-nitride	**Cr_2N**	$(Cr,Fe)_2N$	72	6	15	700-950	δ	Hexagonal	4.80 / 4.47	P31m
	CrN	(Cr,Fe)N						Cubic		
Tau	**T**	-				550-650		Orthorombic	4.05 / 4.84 / 2.86	Fmmm
	H	$(Fe,Cr)_2(Mo,Nb,Ti,Si)$						Hexagonal		
Epsilon	**E**	Cu-rich					δ			
	G	> 14% Si	25	5	4	300-400	δ/α'			
Carbides	**$M_{23}C_6$**	$M_{23}C_6$	58	2.5	12	650-950	δ/γ	Cubic	10.56 – 10.65	Fm3m
	M_7C_3	M_7C_3				950-1050	δ/γ	Hexagonal	4.52 / 6.99 / 12.11	Pnma

Table 4. Mechanical properties of SAF duplex stainless steels.

Grade	UNS	W- Nr	$R_{p0.2}$, N mm^{-2}	R_m, N mm^{-2}	A, %	HRC
2304	S32304	1.4362	400	630 – 820	25	30
2205	S32205	1.4462	485	680 – 880	25	28
2507	S32750	1.4410	550	800 – 1000	25	32
2707	S32707	-	700	920 – 1100	25	34

2.3.6. Welding Metallurgy

The ratio of austenite to δ-ferrite is quite critical to preserve the advanced mechanical properties. The duplex microstructure is produced by the adjustment of the δ and γ stabilizing alloying elements [57]. Duplex stainless steels contain high amount of alloying elements which have great effect on mechanical properties. However, high alloy content result in complex phase transformation mechanisms [58]. Decomposition of δ-ferrite and formation of intermetallic phases and precipitates as well as austenite at between 600 – 1200^{o}C, may cause decrease in toughness and corrosion resistance [59]. The microstructure depends on the alloy composition and thermo-mechanical treatment and to preserve the desired properties, it should be equal mixture of austenite and δ-ferrite.

Cooling rate is one of the most important affecting factors for as-welded microstructure of DSSs, which has upper and lower limits in order to have desired metallurgy. Low cooling rates reveal formation of intermetallic phases, whereas high cooling rates may give δ-ferrite content more than 60%. Cooling rate can be adjusted by welding heat input for a specific composition and thickness of the base metal to be welded.

Heat affected zone, HAZ, of DSS is narrower than austenitic stainless steels. DSS weldments have about 50 μm-wide HAZ, which correspond only a couple of grains. Therefore, it is hard to test the impact toughness properties of DSS HAZ by conventional methods [60].

2.4. The Property; Fatigue Crack Propagation

DSS have a good combination of mechanical and corrosion properties, such as strength, toughness, IGC, pitting and crevice corrosion resistance. Due to its relatively higher strength, chloride stress-corrosion cracking and pitting resistance, DSS has been preferred to austenitic stainless steels enclosing and constructive assemblies where especially chloride attack is a consideration. Although DSS have superior behavior in terms of crack resistance [61], they are still susceptible to chloride-induced corrosion fatigue.

Welding is a necessary process in fabrication of enclosing and constructive assemblies. Welded joints usually constitute the weakest spots through the assembly in terms of fatigue

failure. Fatigue damage may occur at weldments even under modest in-service stresses due to notch effect of weld discontinuities. Figure 25 illustrates the notch effect of weld cap and root, and representative stress concentration levels. The effect of stress concentration at these critical locations arising from variations in the weld geometry profile and stress distribution through the weldments cannot be neglected when evaluating the fatigue conditions.

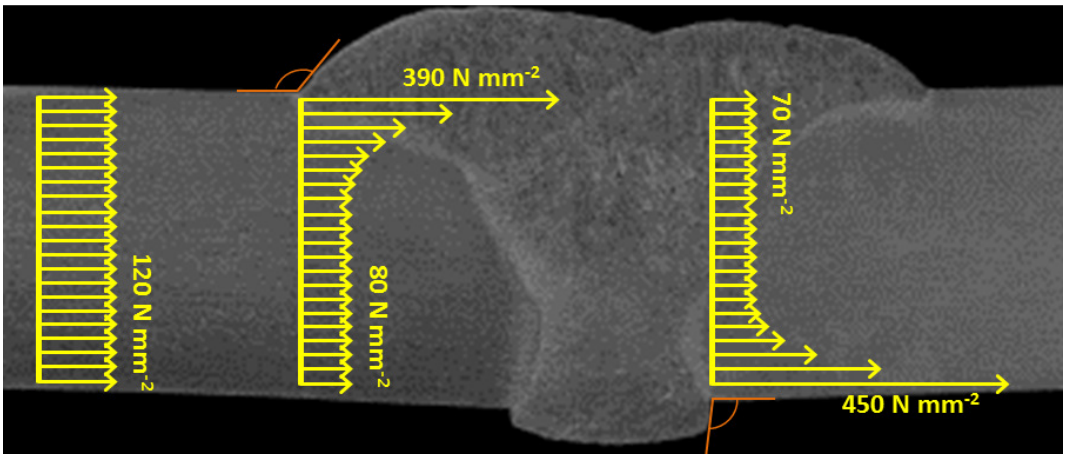

Figure 25. Notch effect due to the weld root protrusion and the weld throat.

In order to improve the fatigue properties of weldments, certain post-weld processes have been proposed, purposing a reduction in the notch effect due to the weld root protrusion and the weld throat; grinding the weld throat [62, 63, 64], water-jet eroding [63, 64] or dressing (remelting) it using GTAW and PAW [65] are mostly studied processes. Baptista *et al.* [62] have observed that the fatigue strength of specimens of throat ground joints was higher than the one of the as-welded specimens for austenitic and duplex stainless steel alloys both in air and under chloride attack. Although arc dressing has also been observed an effective process, today only weld throat dressing is accepted by standards [66]. Keyhole based hybrid welding processes are also found to be effective, providing a good control over the weld profile [67].

The fatigue failure progress on "defect free" matrixes can basically be divided into five stages:

1. Crack nucleation ($a < a_m$),
2. Microstructurally small crack propagation ($a_m < a \leq a_p$),
3. Physically small crack propagation ($a_p < a \leq a_l$),
4. Long crack propagation ($a_l < a \leq a_c$), and
5. Final fracture;

where a is the characteristic dimension of an equivalent crack in a component, a_m is the smallest crack length that is observable by an electron microscope (order of 0.1 micrometre), a_p is the smallest crack length for physically small cracks (order of 10 micrometre), a_l is the

smallest crack length for long cracks (order of a millimetre) and a_c is the critical crack length at which component fracture occurs. Stages 1 to 3 are involved in the "fatigue crack initiation" phenomenon whereas stage 4 is considered as "fatigue crack propagation" by definition.

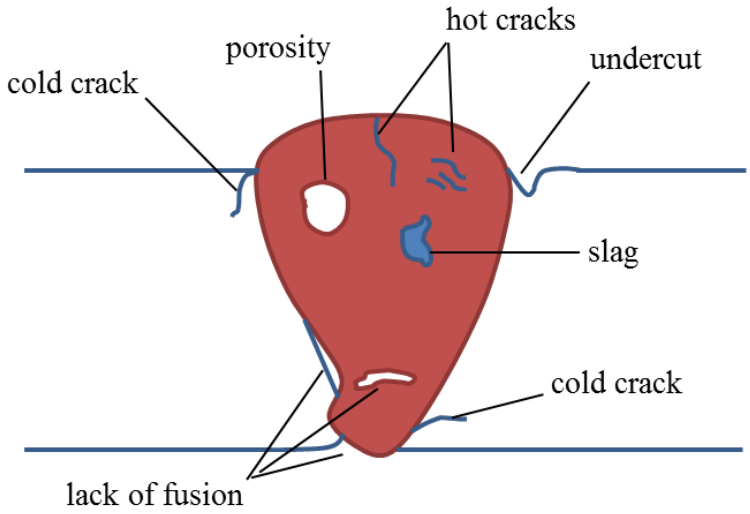

Figure 26. Drawing showing the various regions on the HAZ in a single-pass weld and the possible defects.

All welding joints include discontinuities, which may not be detectable by a non-destructive inspection procedure. Slag inclusions, gas pores, lack of penetration and undercut are common discontinuities, as well as linear defects, such as fabrication (hot) or post-weld (cold) cracks and lack of fusion (Figure 26). A linear discontinuity may be above the critical size for crack initiation (Figure 27). Therefore analysis for fatigue crack propagation behaviour is the key issue rather than crack initiation for a damage tolerant design or fitness for service (FSS) assessment.

2.4.1. Fatigue Crack Propagation

Cracks are inevitable in engineering structures. Damage tolerant design philosophy aims to estimate a safe load and crack length that will predict the failure in an estimated service life. The crack propagation rate can be determined following the definition;

$$\frac{da}{dN} = C\sigma_a^m a^n, \tag{14}$$

where C is a constant, σ_a is the alternating stress and a is the crack length. m has been estimated in different investigations to be from 2 to 4 and n varies from 1 to 2.

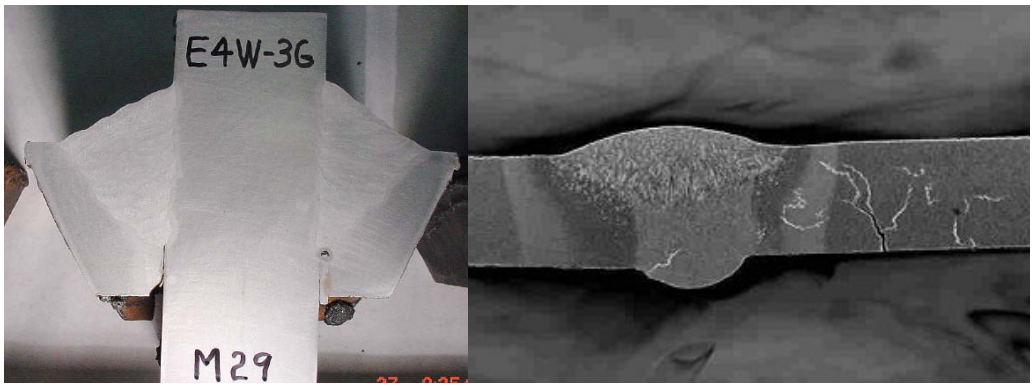

Figure 27. Typical open-surface weld discontinuities; lack of penetration (left – from Oakland Bay Bridge Pile Connection Plate Welding Investigation Report [68]) and cracks (right – from Huijbregts Corrosion Consultancy, www.hbscc.nl).

Crack propagation rate at a series of changing stress levels can be expressed by a crack propagation rate versus the range of stress intensity factor, which is the range between maximum and minimum stress intensity factors. In other words, the range of stress intensity factor (ΔK) governs the crack rate. A cycling load varies with constant amplitude between its maximum and its minimum values. Corresponding stress intensity factors (K) can be calculated from the stress (σ) and crack length (a) as;

$$K = \sigma\sqrt{\pi a}, \tag{15}$$

The range of stress intensity factor is defined as the difference between them. If minimum stress applied is compressive, then minimum stress intensity factor is taken as zero. That is;

$$\Delta K = K_{max} = \sigma_{max}\sqrt{\pi a}, \tag{16}$$

Under cycling loading, if the crack length is determined at a certain number of cycles in real time, and the crack growth rate data (da/dN) is plotted against the actual range of the stress intensity factor (ΔK), and then a schematic representation of crack growth rate versus range of stress intensity factor is obtained (Figure 28). It is a sigmoidal curve, where three different regions are characterized, namely slow crack growth (stage I), steady-state (stable) crack growth (stage II) and unstable crack growth (stage III).

The first region is bounded by a threshold value ΔK_{th}, below which crack does not propagate [69]. Once initiated the crack growths at and above ΔK_{th} along high shear stress planes (Figure 1). This first stage is called slow or short crack growth stage. In stage I the crack propagates until it is decelerated by a microstructural barrier, like grain boundaries or microstructural discontinuities, and thus grain refinement or mechanical and thermal processes, which contribute to an increase in the number of such barriers, provide an improvement in the fatigue strength.

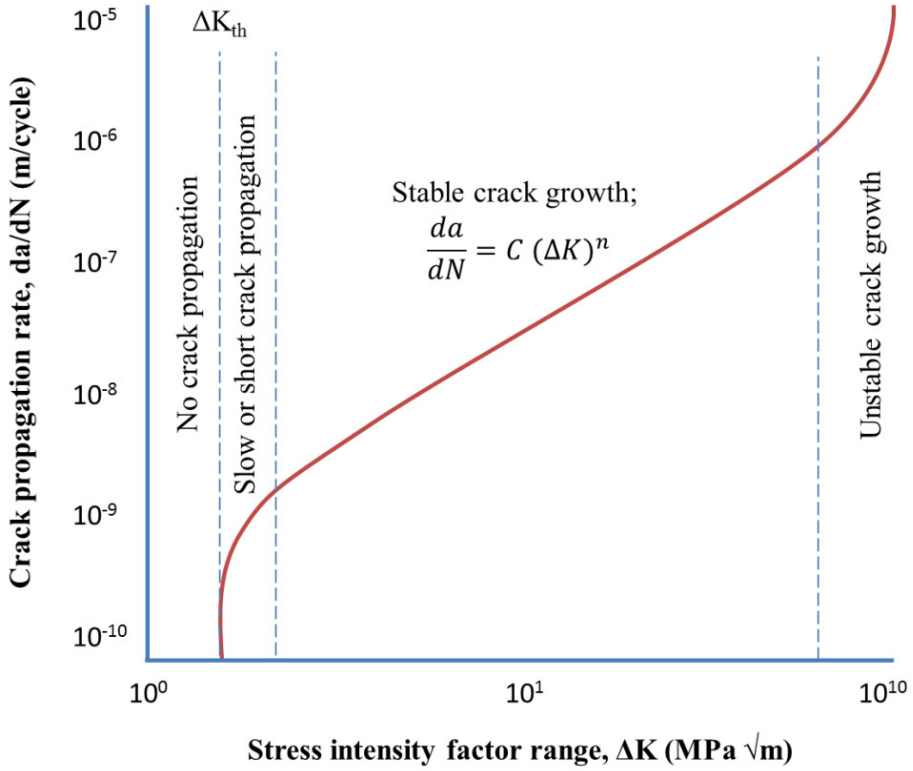

Figure 28. Schematic representation of fatigue crack growth behaviour.

As defined in the Equation 16, the stress intensity factor, K, increases as a consequence of crack growth and/or an increase in the stress level. An increase in K leads to activating slips in different planes close to the crack tip, where the stresses are concentrated. Crack path is oriented perpendicular to the applied stress, whereas it is 45^o with respect to the applied stress during the stage I (Figure 29). The second stage represents a linear relationship between logarithmic values of the crack growth rate and the range of stress intensity factor as follows:

$$\frac{da}{dN} = C\ \Delta K^n, \tag{17}$$

where n is the slope of the curve at second stage and C is estimated by extending the straight line to ΔK of 1 MPa m$^{1/2}$. The definition is referred to as Paris-Erdoğan Law [70].

Ductile materials represent striations on the fracture surface. Striations are formed as a consequence of successive blunting and re-sharpening of the crack tip during the stable crack growth stage.

Unstable crack propagation is observed in the last region, where K_{max} approaches the fracture toughness of the material (K_{ic}).

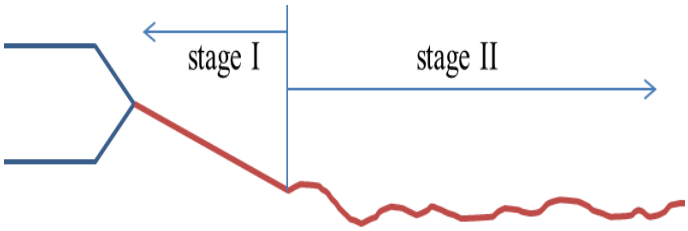

Figure 29. Fatigue crack propagation stages; short crack growth (stage I) and stable crack growth (stage II).

Paris-Erdoğan law provides a connection between fracture mechanics and fatigue [71]. Once K is known for the component, then fatigue life of it can be calculated by taking the integral of the equation 17 between the limits of initial and final crack size:

$$N_f = \frac{1}{A\sigma_r^n \pi^{n/2}} \int_{a_i}^{a_f} \alpha a^{-n}\, a^{-n/2}\, da, \tag{18}$$

where σ_r is the difference between maximum and minimum stresses.

2.4.2. Localized Corrosion

Corrosion processes may be classified as two general types, namely general and localized. General corrosion may occur in a broad range of environments, ranging from fully immersed medium with high chloride ion content to a thin moisture film with low chloride ion content [72]. General corrosion behaviour of stainless steels is principally determined by factors, such as temperature, acidity, chloride ion concentration, and redox potential. Cr(III)-rich passive film provides the corrosion resistance of DSS [73]. Souto *et al.* [74] have studied the nature of the passive film on a DSS alloy and observed it to comprise Cr(III), Fe(II)/Fe(III), and Ni(II).

Contrary to general corrosion, chemical attack is localized during pitting and crevice corrosions. The initiation of localized corrosion is to occur at inclusions, Cr-depleted zones around grain boundaries, intermetallic phases and discontinuities that may damage the passive film. Temperature of the media and chloride concentration of the media are again primary determinants of the localized corrosion process. Manganese sulphide (MnS) inclusions, which usually form at the δ/γ grain boundaries, are preferential sites for the initiation of localized attack. In low N-containing alloys, since the proportions of Cr and Mo are comparatively higher in δ, pits prefer to propagate into γ (Figure 30). In high N-containing alloys, pits may propagate preferentially into δ. Sedriks [75] proposed that lowering the Mn content below 0.5 wt.% in DSS could work concerning localized corrosion resistance.

Figure 30. Crevice corrosion test on duplex alloy 2205 stainless steel in 1 mol dm^{-3} NaCl illustrating preferential attack on austenite phase [76].

The most common methods for ranking the susceptibility of alloys to localized corrosion are PRE_N and the critical pitting (CPT) or crevice (CCT) temperature [77]. PRE_N accounts for the influence of Cr, Mo, N and W (if there is) contents on localized corrosion susceptibility, whereas CPT and CCT defines a threshold temperature beyond which pitting or crevice corrosion takes place for a specific medium.

2.4.3. Corrosion Fatigue of DSS Welds

Generally corrosion problems of as-welded DSS are associated with the HAZ [78]. The principal reason for the corrosion susceptibility is Cr depletion in the δ grains in DSS, leading to a decrease in the resistance to localized corrosion [56]. Cr depletion may be due to the formation of secondary phases.

Fatigue strength of a material drops in a corrosive medium. This is linked to the corrosion properties of the material. The ratio between the fatigue limits that corresponds to the ones in corrosive medium and in air can be correlated with the pitting resistance of the material.

DSS takes advantage of synergic effect of electrochemical and mechanical benefits of δ in media containing chloride resides. When DSS are subjected to stress, γ is more likely to be deformed, owing to its lower yield strength. Meanwhile δ behaves like anode and provides protection to γ, which behaves like cathode.

2.4.4. Fatigue Crack Propagation Behaviour of DSS

Combining high fatigue strength and high chloride-induced corrosion resistance, DSS has been increasingly interested by design engineers for structural and enclosing assemblies, which give service in corrosive media. The material owes such superior properties relative to austenitic grades to δ phase. However δ is prone to excessive hardening by formation of intermetallic and other secondary phases. The effect of spinodal decomposition of δ to α^{l} [79, 80, 81, 82, 83] and precipitation of brittle σ and χ phases [84, 82] have been widely studied.

In weldments, crack initiation can be suppressed by controlling the microstructure of weld metal and HAZ ensuring that the fracture toughness is sufficiently high for the stress levels to be experienced.

The welded structures are often subjected to dynamic service loads including cyclic and/or random fluctuations. The fatigue behaviour of the welded structures is complicated by numerous factors intrinsic to the nature of welded joints. Stress concentrations generally occur at the locations of crack-like defects and at weld toes, with the latter owing to variations in the weld geometry profile. Such discontinuity stresses generally exceed the nominal values, and if proper care is not taken, these critical areas can become the sites of crack initiation, with subsequent crack propagation causing structural failure.

CHAPTER 3

EXPERIMENTAL STUDIES

3.1. General

This chapter on experimental studies and work includes 7 sections. Firstly, the base and the filler metals are introduced in terms of delivery conditions, standardization and chemical compositions. Next section deals with fabrication of the weldments. Measured (welding power, linear welding speed, cooling rate) and calculated (heat input) welding parameters are described in that section. This section is followed by descriptions of Ferritescope and residual stress analyses, which were executed before sectioning the welded plates. Inspection and testing procedures for the basic integrity and quality assessment are then addressed. ISO 15614-1 [85] is referred for qualification of the welding procedures. These preliminary works and studies are followed by sections that describe the methodology and procedures for comprehensive characterization of the weldments in terms of microstructure and micro-hardness. The last section (3.8) is the main focal issue of the thesis, as it concerns fatigue crack propagation tests in both laboratory air and NaCl solution.

3.2. Base and Filler Materials

11-mm thick DSS grade 2205 plates were subjected to the investigation. The plates were delivered from Outo Kumpu with heat number 490288 and conformed to ASTM A240 S32205 and EN 10088-2 X2 CrNiMoN 22-5-3 (1.4462). They are sectioned for welding works and base metal characterization as well. Elemental analysis of the base metal gave data that was consistent with the material certificate as per the standard EN 10204 type 3.2. Ni-enriched duplex filler wire was employed during HPAW and GMAW operations. Welding wire was delivered from ESAB with lot number IT21640. 1.2 mm-diameter filler wire is standardized as per SFA/AWS 5.9 ER2209 and ISO 14343-A G 22 9 3 N L. Promoting γ formation, excess Ni is preferred in filler wires. The chemical constituents of the base metal and filler wire were tabulated in Table 5.

Table 5. Major alloying element constituents in weight fractions in the base material (S32205) and the welding wire (ER2209).

wt %	***C***	***Si***	***Mn***	***P***	***S***	***Cr***	***Ni***	***Mo***	***N***
S32205	*0.015*	*0.39*	*1.6*	*0.023*	*0.001*	*22.8*	*4.8*	*2.6*	*0.19*
ER2209	*0.010*	*0.45*	*1.5*	*0.020*	*<0.01*	*22.9*	*8.7*	*3.1*	*0.17*

Microstructural and mechanical characterizations of the base metal were conducted together with the weldments, as described in subsections 3.3 to 3.9.

3.3. Welding Procedures

The plates were sectioned and bevelled for butt welding operations. PAW was applied on square-groove butt joint and the root gap was 0.5 mm in order to stabilize the operation, which requires equilibrium between the pressures of the orifice gas and the metal vapour through the keyhole. Conventional bevel angle, root face and gap sizes were introduced to V-grooved butt joint for the GMAW performance. A joint design was developed specifically for HPAW considering convection and dilution processes. Bevelling details for all three techniques are given in Figure 31.

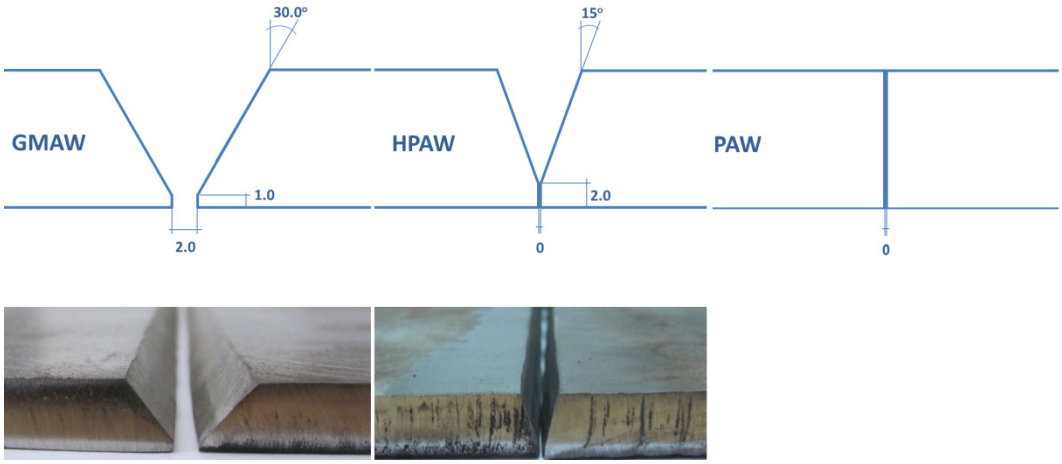

Figure 31. Edge preparations for butt welding processes of 11.1 mm-thick plates using three different methods; (from left to right) GMAW, HPAW and PAW.

Bevelled pieces were joined by GMAW, PAW and HPAW at the flat position. The pieces were clamped to a welding platform and the torch was driven by the movement of a single-axis translation stage (Figure 32). The contact tube distance and bevel axis were manually set prior to performances since a seam tracking system was unavailable.

A single arc exists between the filler wire electrode and the work piece in GMAW and between the tungsten electrode and the work piece in PAW, whereas two different arcs exist simultaneously in HPAW. They have straight polarity direct current between the work piece and the tungsten electrode and reversed polarity direct current between the welding wire electrode and the work piece. A lanthanated tungsten electrode, 3.2 mm in diameter, was used for the plasma arc. Neither hot nor cold filler wire was used during PAW. Welding parameters employed during operations were given on the Table 6.

An argon-2% O_2 gas mixture was applied for shielding of the solidifying weld metal and HAZ in all welding processes. Shielding gas flow rates were 14, 21 and 21 litres per minute

for GMAW, PAW and HPAW, respectively. High purity argon (99.999%) was used as orifice gas with the flow rate of 4.5 litres per minute during HPAW and PAW performances, and the orifice diameter was 3.2 mm.

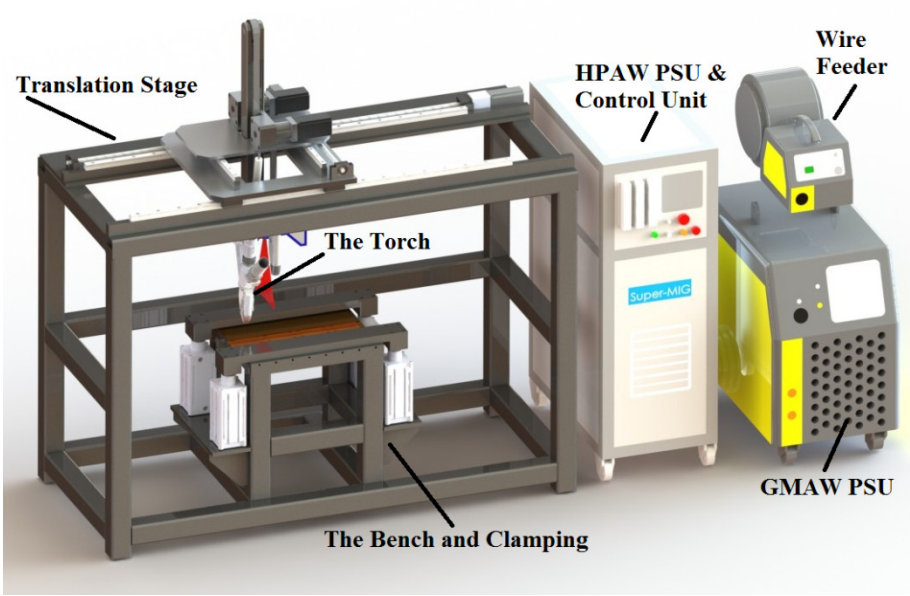

Figure 32. A simple layout for the system employed for mechanized welding.

Table 6. Welding parameters.

		GMAW	HPAW	PAW
Wire feeding speed, WFS	m min^{-1}	8.9 – 10.1	17.8	*N/A*
Wire-arc current	A	210 – 230	320	
Wire-arc potential	V	22 – 24	27	
Plasma-arc current	A	*N/A*	190	190
Plasma-arc potential	V		15	15
Linear welding speed, LWS	cm min^{-1}	35 – 40	50	20
Heat input, per pass	kJ mm^{-1}	0.67 – 0.70	1.09	0.51
Heat input, total	kJ mm^{-1}	2.77		
Cooling rate	^{o}C s^{-1}	108.3 – 75.7	27.1	33.1

Assembling the plates in a way that root gaps were kept closer than the width of the arc column enabled us to obtain stable keyholes during PAW and HPAW. Consequently the plasma arc could impinge on the joint, melt the material and create the weld pool. In the keyhole technique, since the molten pool is prevented from spilling by its surface tension, normally no backing is required for materials having thicknesses up to 6 mm. Ceramic backing was utilized to support the weld pool not only during the root pass of GMAW but also single-pass keyhole welding of the plates that were 11 mm-thick.

Cooling times were recorded between 1300 and 200^{o}C by plunging Type K-chromel thermocouples with ceramics sheath into the weld pool and switching off the arc at the same time. The diameter of thermocouple wires were 1.0 mm. A data acquisition system (SCXI 1112-8 channel thermocouple amplifier with in SCXI 1000 chassis) was used to record temperature versus time data at the sampling rate of 10 Hz. Cooling rates were calculated and presented in Table 6 and cooling curves are represented in Figure 39.

3.4. Ferritescope Analysis

A Fisher Ferritescope was employed on FZ and HAZ to measure the fraction of ferromagnetic (δ-ferrite) phases in as-welded specimens before sectioning them for metallographic examination and destructive testing. A ferrite number (FN) was assigned to each zone in weldments obtained by each method. In order to produce non-trivial and reproducible FN outputs, calibration and practice of the instrument were undertaken as per ASTM A799 [86], ASTM A800 [87] and AWS A 4.2 [88]. The measurements were then compared with the fractions estimated through metallographic examinations.

3.5. Residual Stress Analysis

Residual stress distributions on each weldment were non-destructively determined applying Magnetic Barkhausen noise (MBN) technique. Stress-Tech Rollscan-μscan 500-2 and the probe 4316 were employed during the analyses. MBN amplitudes were calibrated during a uniaxial tensile testing by fixing the MBN probe on the specimen. Yelbay et al. [89] describes the details of the calibration and measurement procedures for welding joints.

3.6. Welding Integrity Assessment and Procedure Qualification

Integrity assessments and procedure qualifications of weldments were executed in accordance with the requirements of standard ISO 15614-1 [85]. Testing included both non-destructive testing (NDT) and destructive testing, which were in accordance with the requirements of the Table 1 in the standard.

Liquid penetrant testing was applied to support the visual inspection and to examine possible weld surface discontinuities. The integrity of the weldments was confirmed using radiographic inspection, where X-ray radiographic examination was recorded on radiographic films. The test was done according to ASTM E1742 [90] and films were evaluated as per the requirements and definitions in ASME BPV Code Section IX [91]. The quality level employed for radiography was 2 % (2-2T using hole type IQI).

Welded plates were then sectioned and tested according to following standards and codes:

- Transverse bend test in accordance with AWS B4.0 A1 [92],
- Transverse tension test in accordance with AWS B4.0 A2,
- Charpy impact test in accordance with AWS B4.0 A3 and ASTM E23 [93],
- Hardness test in accordance with AWS B4.0 C2 and ASTM E384 [94].

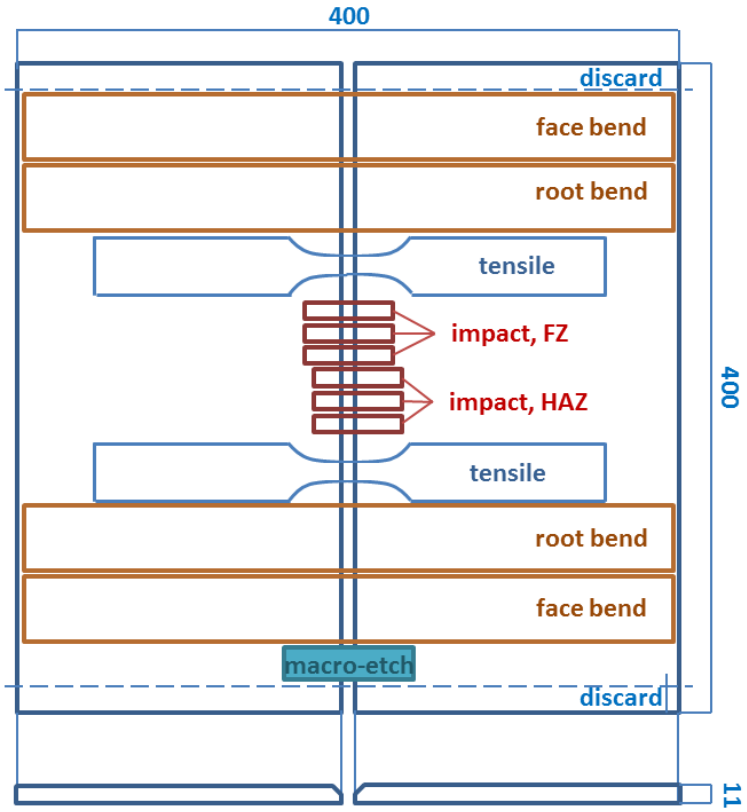

Figure 33. Sectioning plan for destructive testing of welded plates according to ISO 15614-1

Sectioning for test specimens is illustrated in Figure 33. Bend test specimens were prepared for root and face bending. Face bend tests are made with the weld face in tension, and root bend tests are made with the weld root in tension. Specimens were bent to 180^{o} purposing to evaluate the ductility and soundness of welded joints. Bend test is particularly considered to be good at finding linear defects, which would open up on the surface during the testing. Tensile strength of the welded joints was investigated by uniaxial tensioning them to failure. Two sets (FZ and HAZ) of charpy impact specimens were prepared and tested at -50^{o}C. The Charpy specimens were machined to 5x10x55 (mm^{3}) with their 2 mm V-notches transverse to the weld direction, perpendicular to the plate surface and centred at the weld metal and fusion lines at 4 mm below the weld top. Each set was comprised of three

specimens. Instead of classical weld macro-hardness examination, micro-hardness survey using a Vickers indenter at a load of 9.8 N (HV1) was carried out on transverse planes to the welding direction; the spacing between indentations was 0.5 mm.

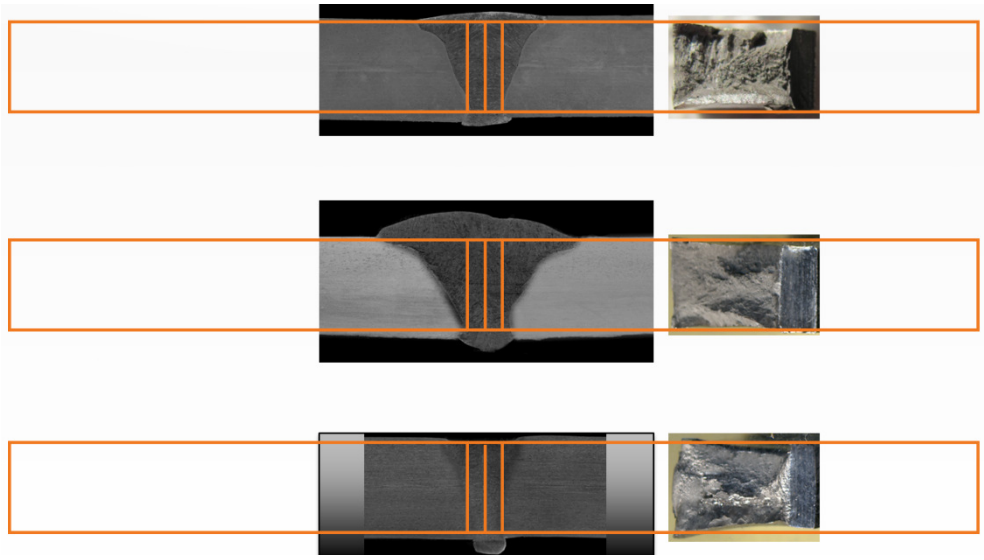

Figure 34. FZ centred CIT specimen configuration for HPA, GMA and PA welds.

3.7. Microstructural Characterisation

Basically three microstructural characterization methodologies were followed; metallography, energy dispersive X-ray spectroscopy (EDX or EDS) and X-ray diffraction (XRD) analysis.

Table 7. Reagents employed to reveal microstructural features during OM examinations.

Reagent	Composition	Procedure	Purpose	Ref.
Beraha II	20 mL HCl 100 mL deionised H_2O 0.3-0.6 g $K_2S_2O_5$	etching at 40 – 60°C	to reveal δ and γ	[95]
Aqua Regia	45 mL HCl 15 mL HNO_3 20 mL ethanol	etching at RT		[96]
KOH	15 g KOH 100 mL deionised H_2O	3 – 5 V 12 sec	to reveal intermetallic precipitates	[97]

Base metal (hot rolled, solution annealed and quenched) were sectioned and three faces were subjected to metallographic examination. The pieces joined using all three welding methods were sectioned transverse to the weld direction for metallographic examinations. Powder samples were obtained from base metal and FZ of weldments to be analysed with XRD.

Specimens were first grinded with various grades of SiC papers for macro-etch examination. The examination allowed us to see the cross section of the weld. Macro-etch examinations also confirmed that there was no any porosity, inclusion or lack of fusion in the weldments.

Macro-etch specimens were grinded once more to prepare them for metallographic examinations. The procedure was followed by polishing using 6, 1 and ¼ μm Alumina colloidal. The specimens were etched with Beraha II, Aqua Regia (Königswasser) and KOH electrolytic reagents to enhance the contrast between δ and γ phases and reveal the σ-phases under optical microscope (OM) and scanning electron microscope (SEM) [98]. Some of typical specimens were left un-etched for backscattering examination by SEM.

The specimens were first examined using OM to measure the size of grains as per ASTM E112 [99] and volume fraction of phases by manual point count as per ASTM E562 [100] and by an image analysis software as per ASTM E1245 [101]. SEM was utilized to detect and observe secondary phases under high resolution. Cr, Ni and Mo concentrations in δ and γ in HAZ and FZ were analysed using energy dispersive x-ray spectroscopy (EDX) system linked to SEM. Analyses were also focused on locations nearby γ_2 and intermetallic precipitates.

X-ray diffractometry was employed for powder samples extracted from fusion zone of all weldments. CuKα radiation was utilized at 2θ range from 20^o to 70^o with the scanning rate of $0.5^o\ min^{-1}$.

3.8. Fatigue Crack Propagation Tests

Fatigue crack growth (FCG) tests were carried out on compact tension specimens prepared from HPA and GMA weldments. The weldment obtained by PAW was omitted due to its obvious high δ content and low impact toughness as a consequence. ASTM E647 [102] was followed during the tests to examine the favourable path of crack growth and to estimate the FCG rate.

ASTM E647 proposes a test method that covers the determination of fatigue crack propagation rates from near-threshold to K_{max} controlled instability. Testing results are expressed in terms of the crack-tip stress-intensity factor range. Crack-tip stress-intensity factor range (ΔK) is defined by the theory of linear elasticity. The thickness and strength of the test material are not limited as long as sufficient planar size is provided in order to prevent buckling and keep the test in elastic conditions.

Various specimen types and geometries are available in accordance with the standard. Middle tension specimen, eccentrically-loaded single edge crack tension specimen and compact specimen are three optional types of FCP test specimens. Compact (tension)

specimen (CT) and corresponding test configurations were preferred during the analysis of fatigue fracture kinetics since it has the advantage over other specimen types in that it requires the least amount of test material to evaluate crack propagation behaviour. This specimen is a single-edge-notch specimen loaded in tension. CT specimen and test configurations are defined and described in Annex A of the standard.

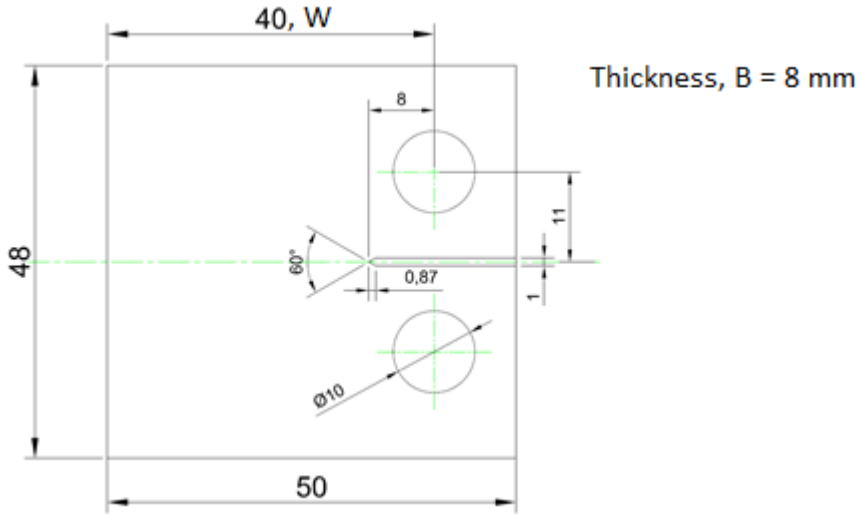

Figure 35. The geometry and dimensions of the CT specimen employed during FCG tests.

Purposing to examine the effect of γ_2 on FCP behaviour of the FZ, specimen size was considered and set to be 8 mm. Therefore, the FZ formed by the fill passes would be subjected to the crack propagation. The load to be applied was set considering the planar size of the specimen, yield strength and fracture toughness properties of the material. The second reason for reducing the thickness was to get a small B/W (Figure 35) ratio in order to reduce the effect of a through-the thickness distribution of residual stresses acting perpendicular to the direction of crack propagation. For the CT specimen the following is required in the Annex:

$$(W - a) \geq \frac{4}{\pi}\left(\frac{K_{max}}{\sigma_{YS}}\right)^2, \tag{19}$$

Rectangular pieces centred the fusion zone were sectioned from the welded plates, and the thickness of the pieces were reduced to 8 mm. Then, compact tension (CT) specimens were machined to the geometry in accordance with the standard. The notch was located so that a crack would initiate in the centre of FZ and propagate through the centre of FZ during the test. Orientation of the notch was L-T (concerning the rolling direction of the plates) and the depth was 8 mm from the central axis of the holes. The notch was obtained by an automated high precision saw cutting system. Schematic representation and orientation of the CT specimens can be seen in Figure 35 and Figure 36. Finally, faces of the specimens were grinded and polished with the same procedure applied for metallographic examination.

An MTS servo-hydraulic machine with a capacity of 100 kN equipped with Instron 8500 and controlled by the Fast Track program was employed during tests. Physical crack size (a), which is a linear measure of a principal planar dimension of a crack, was measured visually by travelling optical microscope with a sensitivity of 9.12 x 10^{-3} mm, which is lower than the requirement by the standard (0.1 mm).

Specimens first pre-cracked using K-increasing process under a mean force of 5500 N and with amplitude of 4500 N and in laboratory air (R = 0.1). Tension-tension loading was conducted during pre-cracking and testing since it is not recommended in the standard for tension-compression testing due to the uncertainties introduced into the loading experienced at the crack tip. Pre-cracks of 1.00 – 1.20 mm were formed after between 30000 and 40000 cycles. A cycle (N) is assumed as the force variation from the minimum to the maximum, and then to the minimum force under constant amplitude loading.

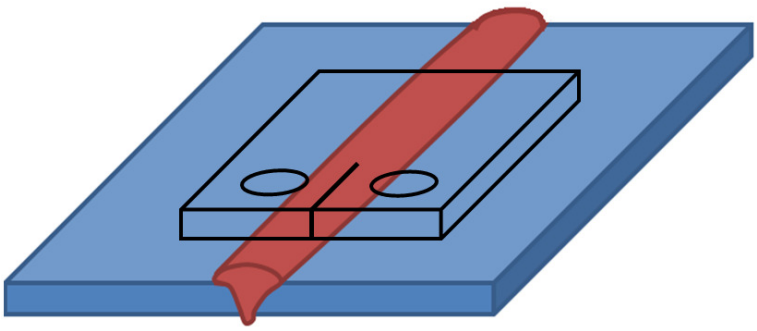

Figure 36. Representation of the orientation of CT specimens prepared from GMA and HPA weldments.

FCG tests were carried out in two different media; laboratory air and 3.5% NaCl aqueous solution. Crack lengths were grown to the range of 0.5 - 0.6 W with K-increasing method under a mean force of 4400 N and with an amplitude of 3600 N (R = 0.1). Loading frequencies were 5 Hz and 10 Hz for testing medium of 3.5% NaCl aqueous solution and 10 Hz and 20 Hz for testing medium of laboratory air. Sinusoidal waveform was conducted for all tests. Crack size measurements were made at recommended intervals by the standard in order to get Δa/ΔN data were nearly evenly distributed with respect to ΔK, as follows;

$$\Delta a \leq 0.04W \text{ for } 0.25 \leq \frac{a}{W} \leq 0.40, \quad (20)$$

The second part of the standard addresses some annexes describing special requirements and comments for testing in aqueous environments, and procedures for non-visual crack size determination, such as compliance method and electric potential difference method, as well as various specimen configurations. Special requirements for testing in aqueous environments are described in Annex A4 in the standard.

Pins and gripping fixtures (holders) were machined from Gr 316 austenitic stainless steel. Painting and rubber coating were applied to the surfaces of these tools to prevent them from the Cl^- attack. The tools were then inspected using dye penetrants for possible surface cracks that would affect the results of the tests. The solution is pumped and poured to the actual crack tip using a plastic pipe. The solution in a reservoir was refreshed in every 2 hours during testing to avoid any significant change in composition of the solution.

The physical crack size (a) was recorded from both sides of the specimen for each number of cycles (N) during the tests. The physical crack size was assumed to be the average of two recordings. This data was first used to obtain "a versus N" curve for specimens subtracted from BM and GMA and HPA welded plates. Fatigue crack growth rate and stress-intensity factor range values corresponding each a and N were then calculated. Fatigue crack growth rate is the rate of crack extension under fatigue loading, expressed in terms of crack extension per cycle of fatigue (da/dN or Δa/ΔN). The rate was determined from the crack size versus elapsed cycle data. Utilizing secant or incremental polynomial methods, which are suitable for the K-increasing (constant ΔP) test, are recommended in the standard.

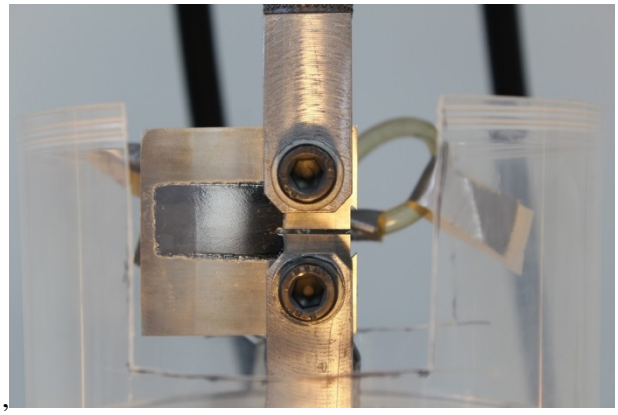

Figure 37. Fatigue crack propagation test setup. NaCl solution was supplied by a pipe during the test.

Stress-intensity factor range (ΔK) is the variation in the stress-intensity factor in a cycle, that is

$$\Delta K = K_{max} - K_{min}, \tag{21}$$

and stress-intensity factor (K) is defined as

$$K = \sigma\sqrt{\pi a}, \tag{22}$$

The reader should be aware that these K definitions do not include local crack-tip effects, like crack closure, residual stress and blunting. ΔK values were calculated using the following expression;

$$\Delta K = \frac{\Delta P}{B\sqrt{W}} \frac{(2+a)}{(1-\alpha)^{\frac{3}{2}}} (0.886 + 4.64\alpha - 13.32\alpha^2 + 14.72\alpha^3 - 5.6\alpha^4), \quad (23)$$

where $\alpha = a/W$, and this expression is valid for $a/W \geq 0.2$.

Fatigue crack growth threshold, ΔK_{th}, is an asymptotic value of ΔK at which da/dN approaches to zero. The practical definition of ΔK_{th} is given as that ΔK, which corresponds to a $\Delta a/\Delta N$ of 10^{-10} m cycle^{-1}. Firstly, a best-fit straight line from a linear regression of log $\Delta a/\Delta N$ versus log ΔK using five data points of approximately equal spacing between growth rates of 10-9 m cycle^{-1} was obtained. ΔK value, which corresponds to a growth rate of 10^{-10} m cycle^{-1} using the best-fit line, was then calculated. This value was assumed as ΔK_{th} as per operational definition of this test method.

Specimens were completely separated after FCP tests, side sections (S-T) and fracture surfaces (L-T) were examined under SEM for fractography. Striation measurement was carried out on the fracture surfaces of specimens. Striation measurements were done at ΔK values from 25.50 to 48.67 MPa$\sqrt{m}$. $\Delta a/\Delta N$ records were compared with the results of these measurements to ensure the data was consistent.

CHAPTER 4

RESULTS

4.1. Process Metrics and Macro Features

11.1 mm-thick DSS plates were joined in 4 passes of GMAW and in a single pass of HPAW and PAW. Macro sections of weldments are shown in Figure 31. The ratio of penetration of weld bead to its width (aspect ratio) was calculated as 0.6 (average of passes), 1.5 and 2.5 for GMA, HPA and PA welds, respectively.

In addition to the composition of shielding gas (18% CO_2 + Ar, remaining), arc potentials (22 – 24 V) and current amplitudes (210 – 230 A) utilized for 1.2 mm diameter filler wire were suitable for stable spray transfer metal deposition during GMAW. Heat input (H) per pass was in a range of between 0.67 and 0.70 kJ per mm of joint length. Overall heat input was calculated as 2.78 kJ mm^{-1} for the multi-pass GMAW. Total arc time was recorded as 10.4 minutes and overall operation duration was recorded as 18.4 minutes, including inter-pass pauses to wait for the work piece cooling down to 180°C. Joining was completed with approximately 900 grams of filler.

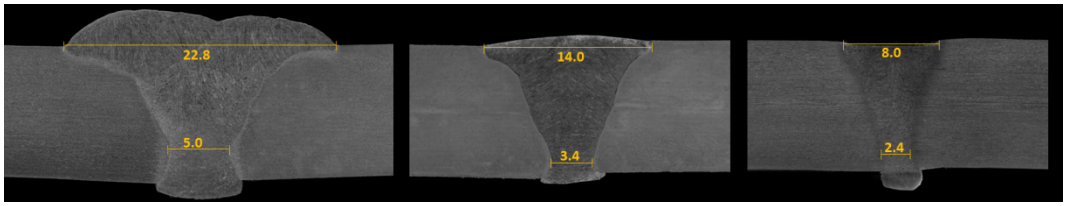

Figure 38. Macro–etch specimens of (from left to right) GMA, HPA and PA welds. Dimensions are in millimetres.

In order to fill the bevel under high LWS, wire feeding speed (WFS) was set to 17.8 meter per minute during HPAW, providing wire current amplitude of 320 amperes. 316 grams of metal was deposited to the joint bevel in 2 minutes of overall process time. The keyhole was achieved by a plasma arc at 190 A and 15 V. Total heat input of the process was calculated as 1.09 kJ per mm of joint length.

PAW was applied without filler wire on square-groove butt joint and the root gap was 0.5 mm in order to stabilize the operation, which requires equilibrium between the pressures of

the orifice gas and the metal vapour through the keyhole. However 1 mm of protrusion at root side yielded an insufficient throat that was approximately 0.5 mm below the plate surface line after this autogenous welding process. The process was completed in 5 minutes and 0.51 kJ of heat was introduced to a millimetre of joint. Heat input values can be seen in Table 6 and welding efficiency metrics are graphically presented in Figure 61.

Macro sections of the weldments can be seen in Figure 38. Cap size and minimum root gap are indicated on the Figure. Welding integrity and efficiency are clear on macro-etch photographs of the weldments.

4.2. Cooling Rates

Cooling curves obtained by thermocouple reading and temperature data acquisition during the welding processes are represented in Figure 39. Type K-chromel thermocouples, which are the most common sensor calibration type, are Ni based and exhibit good corrosion resistance. Their melting point is 1370°C and they are reliable and accurate at temperatures up to 1260°C. During the measurements, the thermocouple material was protected with a ceramic protection tube due to the reducing character of the weld pool.

Weld pool temperature was recorded when it was between 1290 and 200°C. Cooling times between 1200 to 500°C were calculated, where primary and secondary solid state phase transformations occur. Dividing durations, cooling rates were calculated. Cooling rates and heat input values are given in Table 6.

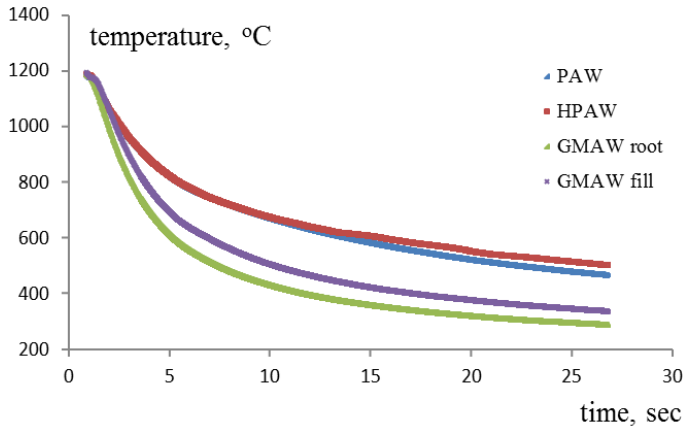

Figure 39. Cooling curves recorded just after switching off the welding arc and in the middle of weld pools.

Cooling rate is determined by the heat input of the welding process and heat transfer conditions through the material. A keyhole was obtained in both PAW and HPAW by high-power-density plasma arc, which supplied deeper penetration with a narrow bead and less

total heat input resulting thinner HAZ. The cooling rate is generally reversely proportional to the heat introduced during welding processes. Since both PAW and HPAW are keyhole based welding methods, aspect ratios of the weldments obtained using these methods were higher than the weldment obtained using GMAW, which is a conduction mode of welding method. Considering the aspect ratios, it was assumed that during HPAW and PAW the heat was transferred as 2-dimensional, whereas during GMAW the heat was transferred as 3-dimensional. Despite having similar heat input values, cooling rate was higher in 3-dimensional heat transfer condition during GMAW then in 2-dimensional heat transfer condition during PAW. Comparing methods HPAW and PAW, 53% reduction in the heat input yielded 22% increase in the cooling rate. Cooling rates just after the completion of the root and the fill passes were also compared and it was seen that pre-heat temperature was more effective on cooling rate of the weld run. 30% reduction was recorded between the root pass, where pre-heat temperature was at room temperature (20°C), and the fill and cap passes, where pre-heat temperature were 180°C.

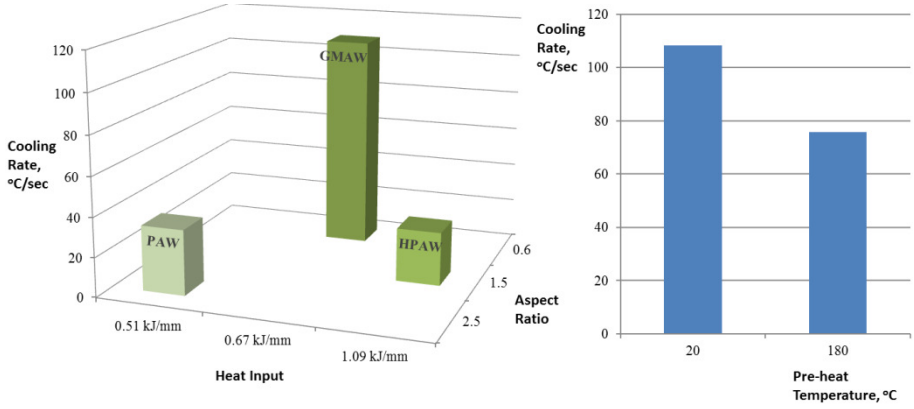

Figure 40. Cooling rates during all three welding processes (left) and varying passes during GMAW (right).

Despite its relatively higher cooling rates, GMAW caused higher proportion of γ in FZ and precipitation of intermetallic phases in HAZ. An explanation for this would be repeating thermal treatments to the material due to the multi-pass welding process. Primary and secondary phase transformations will be discussed in the discussion chapter.

4.3. Fractions of the Primary Phases

Results of quantitative metallography studies and Ferritescope measurements are represented in Figure 41. Autogenous PAW yielded a fusion and a heat affected zone, which contented excessive δ. δ fraction in FZ of HPAW is well below the 70% upper limit, beyond which corrosion and mechanical properties of the material are known to be deteriorated. Depending upon this observation, HPAW might be considered as the only keyhole based welding

technique that provides sufficient base metal dilution with filler metal and consequently proper phase balance [103, 104].

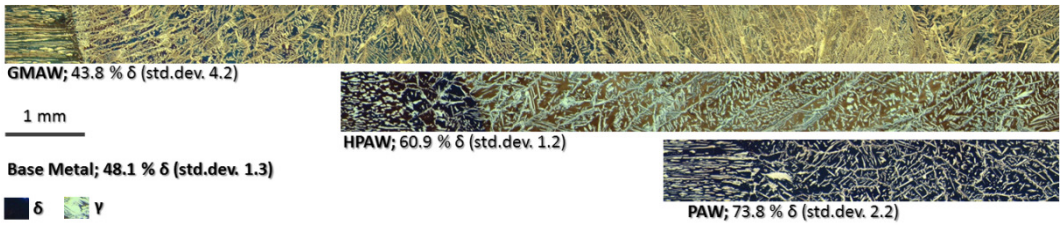

Figure 41. Fusion and heat affected zones of GMA, PA and HPA weldments and unaffected base material under low magnification. δ-ferrite contents in fusion zones of weldments are also indicated below the microstructures.

Although the cooling rate was higher during GMAW process, it leaded to less δ fraction in FZ as compared to the ones of HPAW and PAW. Following passes of the process yielded their own HAZ in former GMAW passes, where γ_W (Widmanstätten Austenite) found opportunity to grow and γ_2 precipitated.

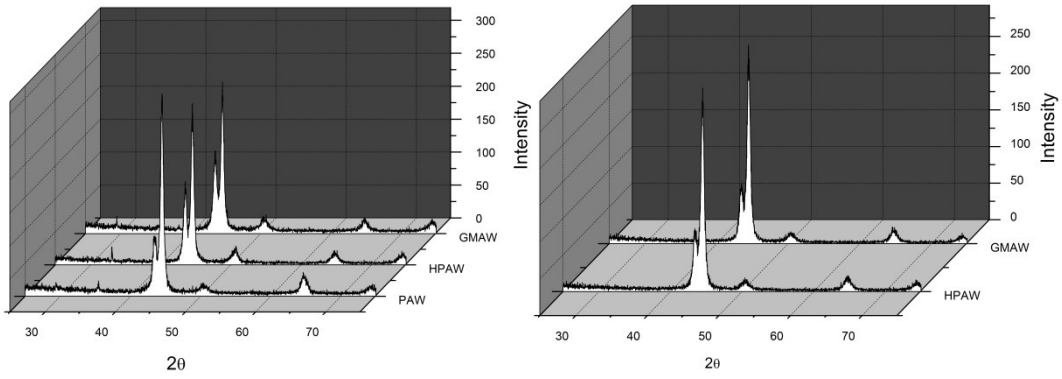

Figure 42. X-ray diffraction patterns obtained from powder samples of as-welded specimens of all welding processes; δ and γ peaks.

4.4. Redistribution of Substitutional Elements

δ and γ grains in FZ of all weldments were analysed using EDX to examine the solute distribution in the as-welded material. The compositions of δ and γ were compared for the weld metals obtained by GMAW, HPAW and PAW in the as-welded condition. Figure 43 represent graphically the solute redistribution in FZ of all three welding processes. Cr and Mo enrichment in δ and Ni enrichment in γ were observed in FZ of all three weldments. High-cooling-rate caused suppression of solute redistribution in FZ and partially melted zone

(PMZ) of GMA weldment [52], where Cr-rich precipitates were observed either in δ grains or at δ/δ or δ/γ grain boundaries. The significant depletion of Cr and Mo in and around γ_2 precipitates was another considerable result of EDX analyses. Depletion of Cr and Mo, together with N, locally reduces PRE_N and so pitting and crevice corrosion resistance of the material.

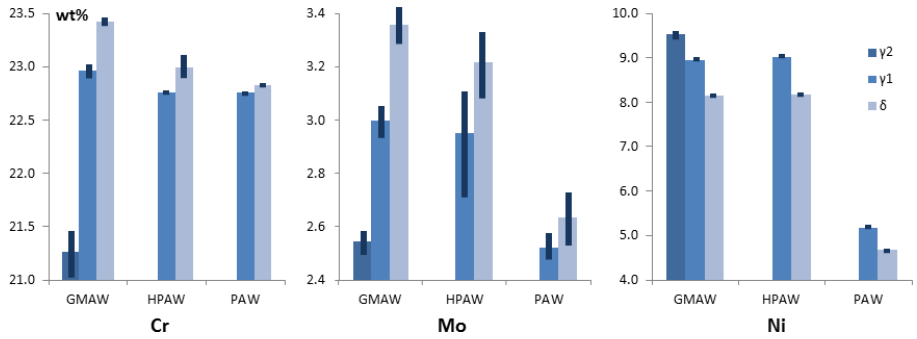

Figure 43. Graphical representations of solute redistribution in fusion zones of weldments.

Nitrogen (N) is also one of the most important elements during evaluation of the pitting resistance of the material as per the following definition;

$$PRE_N = \%Cr + 3.3\,\%Mo + 16\,\%N, \tag{12}$$

PRE_N estimation provides a good approach and comparable value for the pitting resistance behaviour of the material. Cr and Mo were analysed using EDX during SEM examinations, but N.

A limited number of works have been executed to investigate the local N content and establish the partition coefficient of it, which would be defined as the ratio of the N contents between δ and γ. This is due to the difficulties in analysing N at low levels like in DSS [105]. Wavelength-dispersive electron probe microanalysis (EPMA) would provide reliable data for the quantitative analysis of constituent phases of materials, like even γ_2, as long as an extreme care is exercised during the examination and an accurate linear algebraic correction is executed [106]. Moreno *et al.* [107] introduced a methodology for determination of N in δ and γ phases of some non-conventional DSS alloys using EPMA and calibration curves. They also discussed the influence of alloying elements on the N solubility limit. They concluded that the lower Ni and higher Mn content, regarding to conventional DSS alloys, did not significantly affect the N solubility in δ.

In the present work, N content was assumed to be same in the phases that subjected to the investigation in FZ of GMAW and HPAW and close to the contents given in the chemical composition data of the filler metal, which was 0.17 wt.%. PRE_N indices of individual phases presented in FZ of GMAW and HPAW were tabulated in Table 8. As it can be seen in the table, PRE_N index for γ and δ phases in FZ of HPAW are approximately balanced and both

are higher than 35, which is required for standard DSS, whereas index for γ_2 in FZ of GMAW represents a low value, which means γ_2 leads to relatively weaker spots in FZ as far as pitting and crevice corrosion resistance are concerned.

Table 8. PRE_N indices of the phases δ, γ and γ_2.

	GMAW				HPAW			
	Cr	**Mo**	**N**	**PRE_N**	**Cr**	**Mo**	**N**	**PRE_N**
δ	23.42	3.36	0.17	***37.23***	22.99	3.22	0.17	***36.34***
γ	22.96	3.00		***35.58***	22.76	2.95		***35.22***
γ_2	21.26	2.54		***32.36***	N.A.			N.A.

4.5. Secondary Phases

DSSs are prone to transformation of primary phases (usually δ) to secondary phases, if they are exposed to temperatures ranging from 300 to 900°C [1, 108, 55, 109]. Intermetallic phases, carbides, nitrides, α' (Cr-rich ferrite) and γ_2 are considered to be the secondary phases in the microstructure of DSS. Thermodynamic and kinetic conditions of secondary phase formation are determined by the chemical composition, thermal and sometimes mechanical [111, 112, 113, 114, 115] process history of the material.

Table 9. Average chemical composition of intermetallic precipitates in heat treated weld metals [50].

	Aging	**Fe**	**Cr**	**Ni**	**Mo**	**Si**
σ	800°C, 3 hrs	54.0	34.3	4.1	6.5	1.2
	900°C, 30 min	55.1	34.8	4.0	5.1	0.9
R	700°C, 3 hrs	36.0	21.6	3.5	35.5	3.4
	800°C, 5 min	33.2	19.8	3.3	39.2	4.5
	800°C, 3 hrs	37.6	16.4	3.2	38.6	4.1
	700°C, 3 hrs	42.7	26.3	3.7	24.9	2.4
	800°C, 30 min	43.4	24.6	3.6	25.8	2.7
χ	800°C, 5 min	49.3	27.8	3.4	17.8	1.6

DSS is known to be susceptible to spinodal decomposition of δ grains when are exposed to temperatures between 300 and 500°C [109]. Cr-rich ferrite (α') is the product of the spinodal decomposition and leads to high hardness and strength, low ductility and toughness [114]. This aging process is sometimes called as 475-embrittlement, and such embrittlement is not

only a problem for DSS but also for as-welded austenitic stainless steels since they include a fraction of δ phase in their FZ [115, 116].

Armas *et al.* [117] observed that fatigue life of the aged DSS samples were lower than the as-received (quenched and tempered) ones. Extensive hardening of δ grains and micro-cracks, which were rapidly formed at the δ/γ boundaries due to the accumulation of slip bands operated in γ grains, were commented to be the principal reason for relatively bad performance of aged DSS. Moreover, these researchers observed that aging benefited to high-temperature fatigue performance of DSS and they proposed that the cycling stress applied at high temperatures (500^{o}C) could dissolve decomposed phases (α and α^{l}) in δ grains and therefore the cyclic softening was enhanced (Figure 44).

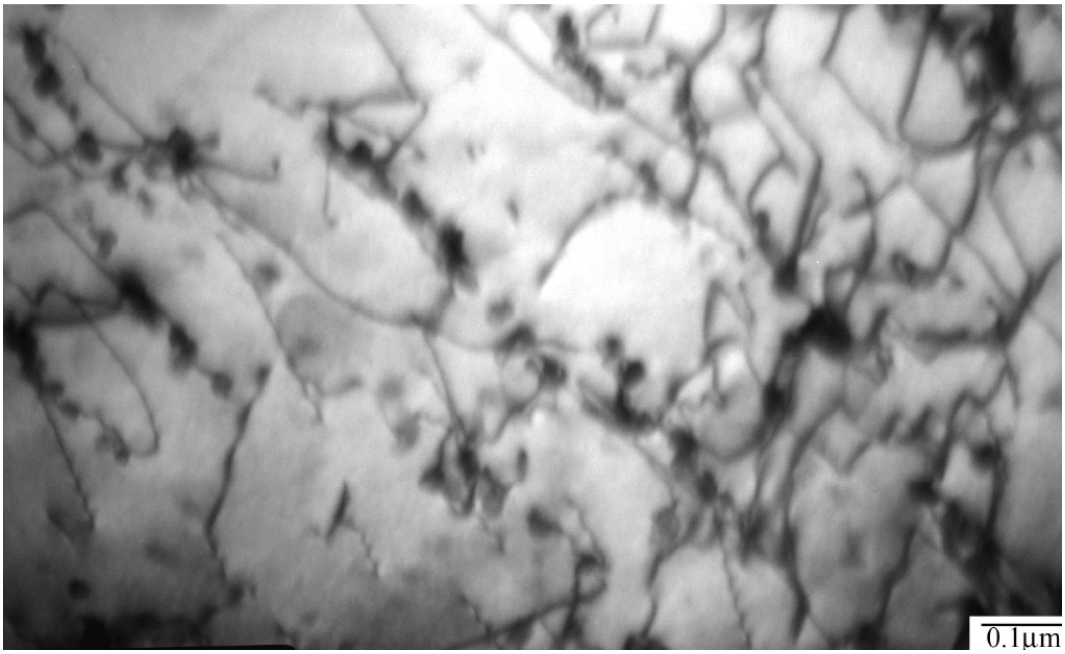

Figure 44. TEM micrographs of an aged δ grain after high-temperature fatigue test. High dislocation density and incoherent precipitates can be seen [117].

Micro-hardness examinations on individual phases (δ and γ) revealed that thermal treatment during welding operations with single and multiple passes was not considerably decomposed δ phase in as-welded DSS.

DSS is highly susceptible to precipitation of intermetallic phases due to their high Cr and Mo contents and high mobility of such elements in δ. Intermetallic precipitates were detected on δ/δ and δ/γ grain boundaries in HAZ of GMA weldment during metallographic investigations in the present study (Figure 47). However, intermetallic precipitation was observed to be significantly suppressed in HAZ of HPA and PA weldments. Metallography work was supported by XRD analyses and charpy impact toughness tests. XRD patterns of GMA and HPA welds are presented in Figure 48. Although, there was no a clear pattern for

σ-phase, there was a noticeable difference in the patterns of specimens extracted from the welded plates using these 2 different welding methods.

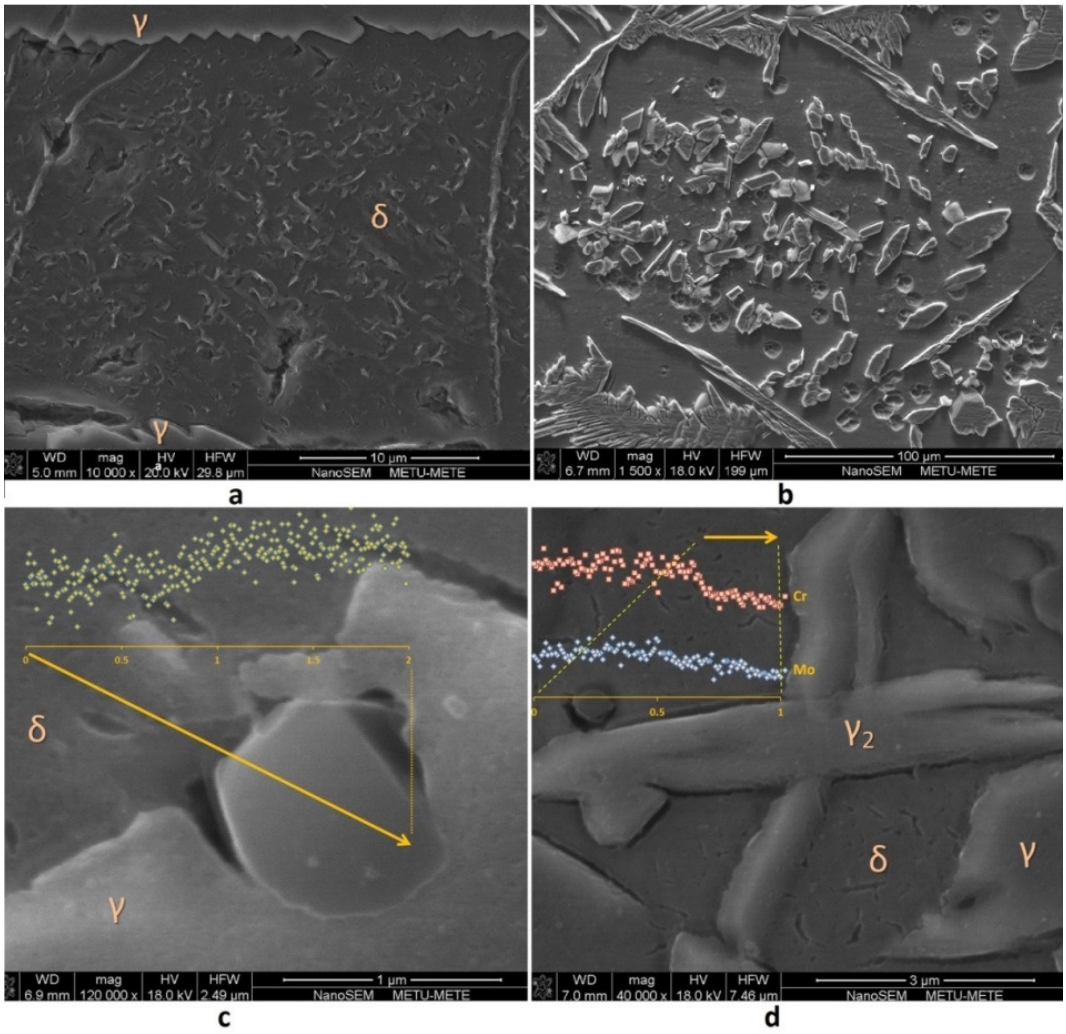

Figure 45. GMA and PA weld metal microstructures revealed by the Beraha etchant. (a) Cr_2N precipitates in δ grains in HAZ of GMA. (b) Cr_2N provides a preferred location for γ_2 precipitation. (c) The advancing γ phase boundary is pinned by a Cr-rich precipitate in GMA weld metal. (d) Intragranular γ_2 precipitates in acicular form in GMA weld metal. EDS analysis of γ_2 has shown that concentrations of Cr and Mo were significantly low, which may lead sensitization.

Karlsson *et al.* [50] identified three different intermetallic phases in the heat treated weld metals, namely tetragonal σ-phase [118, 119], rhombohedral R-phase [120] and cubic χ-phase [121]. σ-phase is the intermetallic phase being formed in the largest volume fractions compared to the other intermetallic phases and at all aging temperatures. A summary of the results of elemental analysis of intermetallic precipitates in the weld metal obtained by acid-

rutile coated CrNiMoN 22 5 3 type stick electrodes are given in Table 9. As it can be seen in the table, σ was found to be rich in Cr but only slightly enriched in Mo, R had a high Mo and Cr and χ had an intermediate composition as compared to former two.

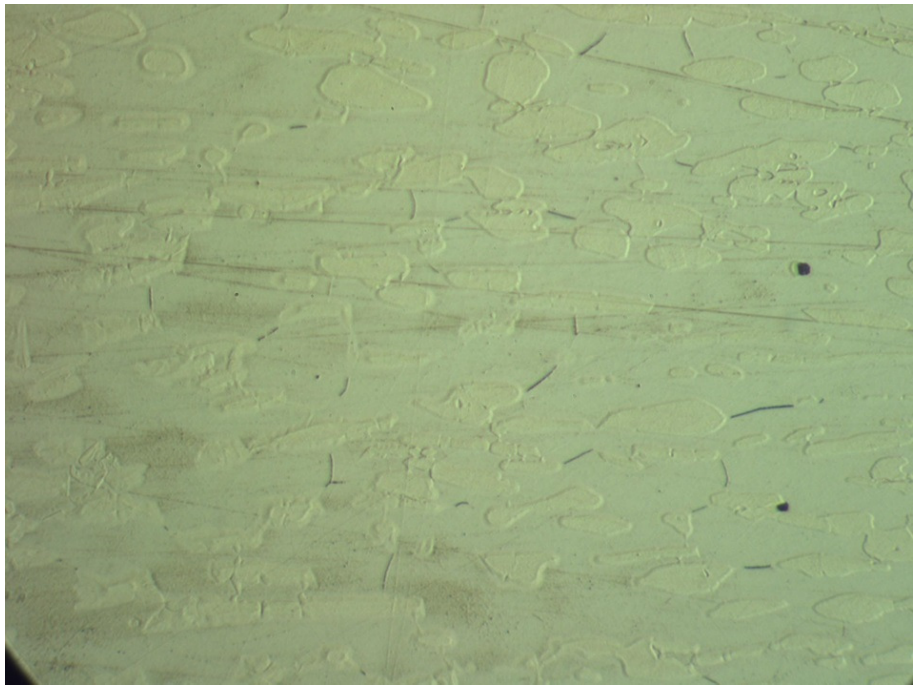

Figure 46. Viella, GMAW HAZ, intermetallic phases

Like γ_2 precipitates, it was analysed that the formation of intermetallic phases also resulted in Cr and Mo depletion in the neighbourhood of them. The EDX analyses of these intermetallic phases and neighbourhood of them were in good agreement with those reported in literature [50].

Other secondary phases, such as τ-phase, π-phase, Cu-particles, $M_{23}C_7$, M_7C_3, Cr_2N and CrN, have also been identified previously in DSS BM and WM [1]. Cr-nitride precipitates were observed in FZ and HAZ of GMAW and PAW in addition to intermetallic precipitates and γ_2 in the present work. Nitride precipitation was observed more in HAZ of GMA welds, probably due to rapid cooling during the process. Kokawa *et al.* [55] observed rod-like Cr_2N precipitates, which were parallel to the cleavage {100} plane in δ, were more coherent along their long facets than at their tips and the tip of these precipitates could act as sinks for H and might be preferential sites for initiation of hydrogen cracking.

Although nitride precipitation appear to be insignificant compared to precipitation of intermetallic phases in as-welded DSS, its precipitation kinetics has still an importance due to the eutectic reaction;

$$\delta = \gamma_2 + Cr_2N, \tag{23}$$

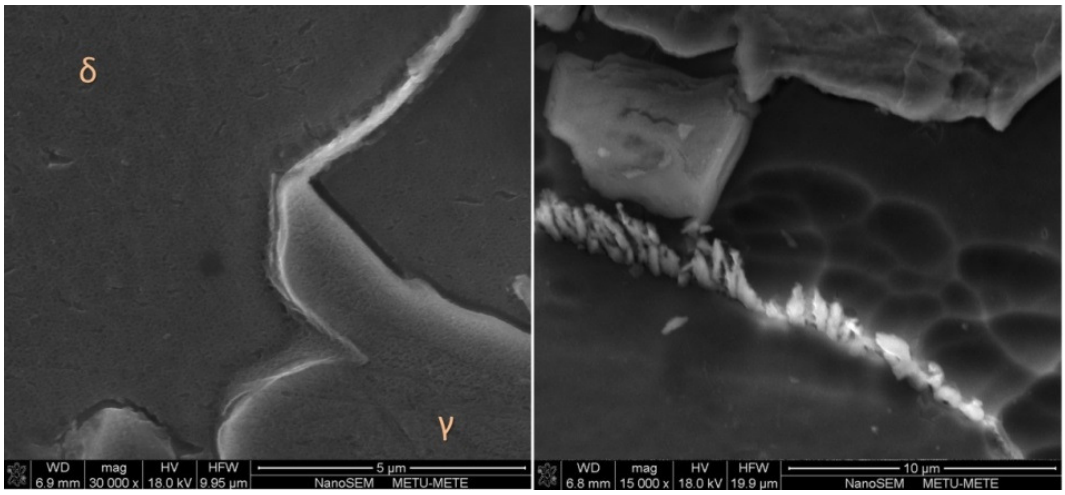

Figure 47. Intermetallic precipitations formed in δ/δ and δ/γ grain boundaries in the HAZ of the GMA weldment.

Nucleation of Cr_2N takes place at dislocations, inclusions, δ/δ and δ/γ grain boundaries, and precipitation occurs from the δ [55]. Being in this metastable condition, when the material is reheated by successive passes during a multi-pass welding, intragranular nitrides dissolve and γ_2 starts to precipitate [122]. On one hand, the γ_2 precipitation has been observed to improve the impact toughness [123]. On the other hand, it has been proposed that the chemical composition of γ_2 compromises the corrosion resistance [122].

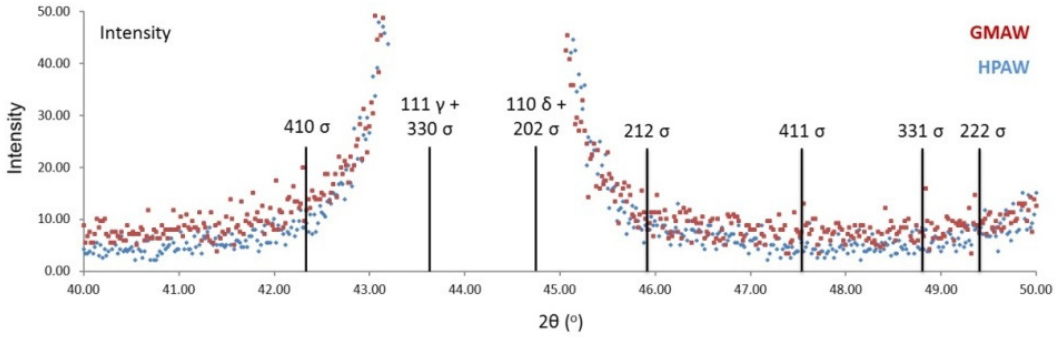

Figure 48. X-ray diffraction patterns between 2θ 40° and 50° obtained from powder samples of as-welded specimens of GMAW and HPAW, and locations of σ-phase peaks.

Formation of γ_2 in the multi-pass welds of the super DSS has been reported to be closely related to Cr_2N dissolution, where N liberated facilitates the γ_2 nucleation [123, 124]. Nilsson and Wilson [125] have proposed another mechanism, in which γ_2 and small equiaxed particles of Cr_2N precipitate in cooperation. During the present study, Cr-rich precipitates were observed together with γ_2 precipitates (Figure 45 (c)). Chemical composition of Cr_2N precipitates and δ matrix is given in Table 10. EDX analyses concluded that these

precipitates were not only rich in Cr but also in Mo, and Fe and Ni contents were relatively low. XRD was not sufficient to detect such low-fraction phases and a comprehensive identification of such phases would be possible using TEM.

Table 10. Chemical composition of the nitrides and ferritic matrix for UNS 32550 [52].

Element	δ	Cr_2N
Cr	27.01 ∓ 0.29	78.97 ∓ 2.47
Fe	61.27 ∓ 0.22	11.12 ∓ 1.43
Ni	6.08 ∓ 0.23	0.70 ∓ 0.38
Mo	3.74 ∓ 0.10	7.49 ∓ 0.69
Cu	1.63 ∓ 0.14	0.36 ∓ 0.23
Si	0.26 ∓ 0.03	0.37 ∓ 0.27
V	0.098 ∓ 0.004	0.99 ∓ 0.08

4.6. Residual Stress

Employing Magnetic Barkhausen Noise (MBN) technique, residual stresses were analysed in the transverse of as-welded plates. Through-thickness or longitudinal analyses were not executed, concerning the transverse path is the most effective one during FCP through the centre of the welds.

MBN technique is applicable to ferromagnetic materials that include small order magnetic regions called magnetic domains [89]. Therefore its application to DSS would give an incomplete data, which is only obtained from δ grains [126]. However, the purpose of the residual stress analyses was framed in selection of the CT specimen location throughout the weld lines, obtaining a general impression about the macro and micro residual stress conditions, and their strain hardening consequences.

Residual stresses measured on weldments by Magnetic Barkhausen Noise Analysis are represented in Figure 49. All three as-welded specimens had tensile stress fields at HAZ and the fusion line, whereas they presented near-zero or compressive stress distribution with distance from the weld. PAW provided the lowest stress magnitudes at both the fusion and the heat affected zones. The residual stresses are narrow for the autogenous PAW and broader for HPAW and GMAW. The maximum residual stress, which was detected in the fusion line of the GMA weldment, was nearly the same as the yield stress of the base material. The GMAW process had the highest peak probably due to the hardest microstructure. Residual stress field widened with the greater heat input, which was maximum for the whole GMAW process.

Magnetic Barkhausen Noise analyses represented a relatively lower tensile (PAW and HPAW) or slightly compressive (GMAW) residual stress fields in the middle of welds, which probably would affect the FCP behaviour of the specimens. Results of residual stress analyses were in a line with previous researches on stainless steels [127]. The possible effects of determined residual stresses will be discussed in the discussion chapter.

4.7. Hardness

The extent of microstructural alteration in HAZ with respect to the base material depends primarily on the welding wire composition and dilution, the amount of the heat input by the welding process and the power density of the welding process. Vicker's hardness indentations were obtained from the fusion zone to the base metal in which maximum hardness values were obtained as 279 and 310 HV1 for HPAW and GMAW, respectively, at the fusion lines (Figure 49). HAZ dimensions observed via both optical metallography and these hardness maps were proportional to the thermal cycles that the material was subjected during one HPAW or PAW pass and four GMAW passes. Micrographs showing HAZ for both techniques revealed not only thinner HAZ in HPAW and PAW joints but also less grain coarsening and intermetallic precipitation at γ / δ and δ / δ grain boundaries (Figure 46).

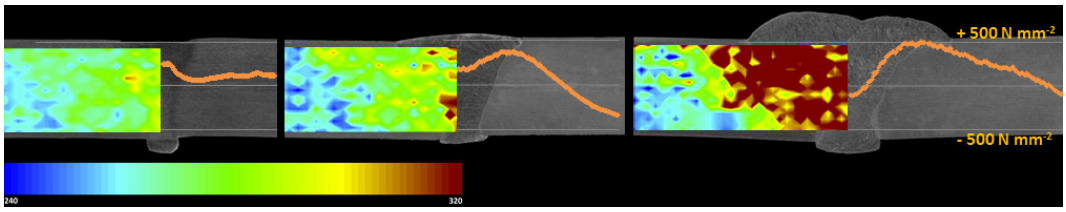

Figure 49. Hardness maps and residual stress profiles on macro sections of the weldments; (from left to right) PAW, HPAW and GMAW. The maximum hardness value and the broadest thermo-mechanical affected zone were recorded for the weldment obtained by GMAW.

A detailed micro-hardness investigation was also carried out on δ and γ grains in FZ of all weldments at a load of 0.49 N (HV0.05). The purpose of this investigation was to see individual contributions of these grains to the strain hardening.

4.8. Impact Toughness

Charpy impact energies at – 50°C of mid-FZ and FL specimens of three welding methods were tabulated in Table 11. Testing temperature was selected to examine the welded specimens at the near-transformation temperature for DSS and make a clear comparison. All welding specimens had significantly less toughness values as compared to BM. While HPAW and GMAW specimens were above the ductility limit, which is assumed to be 27 J for BM and 47 J for WM according to European norms, PAW FZ provided toughness that was lower than the limit probably due to it's the highest δ fraction, which was above 70%. Due to its low toughness values, PAW was dismissed from further mechanical

characterization, including FCP tests. FZ specimens of GMA and HPA weldments absorbed comparable impact energies during testing. Impact toughness and hardness properties of GMAW and HPAW specimens will bring together with the obtaining from microstructural characterization work and be discussed in terms of hardening phenomena.

Table 11. Charpy impact toughness energies (at -50°C) in Joules with maximum deviations. The charpy specimens were machined to 10x10x55 (mm^3) with their 2 mm V-notches at fusion zones, FZ, and fusion lines, FL, of weldments.

	BM	**FZ**			**FL**		
		GMAW	***HPAW***	***PAW***	***GMAW***	***HPAW***	***PAW***
Impact Energy	240.1, 6.6	92.3, 4.4	107.7, 9.6	23.6, 2.7	71.7, 7.1	148.7, 6.9	61.4, 6.5

FZ charpy impact fracture surfaces included varying proportions of cleavage and dimple characters (Figure 50). Appearance of fracture surfaces were in line with impact energies recorded for each specimen.

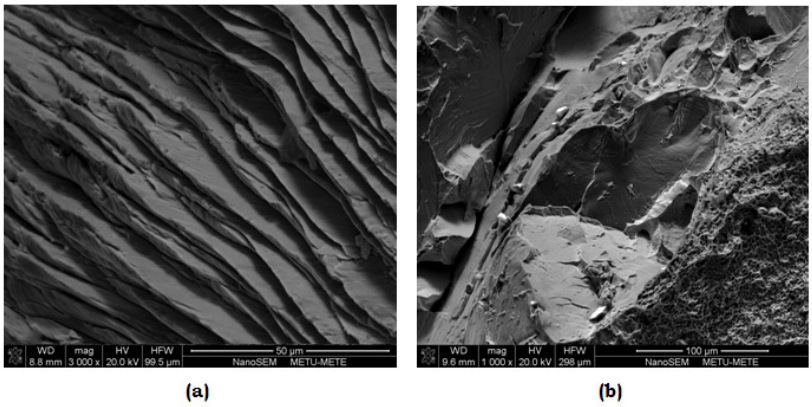

Figure 50. Fracture surfaces from the HAZ of GMA weldment (left) and the FZ of PA weldment (right) after Charpy impact toughness testing.

4.9. Fatigue Crack Propagation

In the previous sections, the fundamental microstructural and mechanical features of GMA, PA and HPA weldments have been reported. Young et al. [128] studied the effect of γ content and its morphology on the impact toughness and FCP behaviour of DSS Gr 2205. They observed that the as-welded material, which was obtained employing LBW, had the highest FCP rate and ΔK_{th} value due to excessive δ (75%) in FZ of the weldment. Since PAW also yielded excessive δ content in FZ, this method was dismissed during FCP tests in the present study.

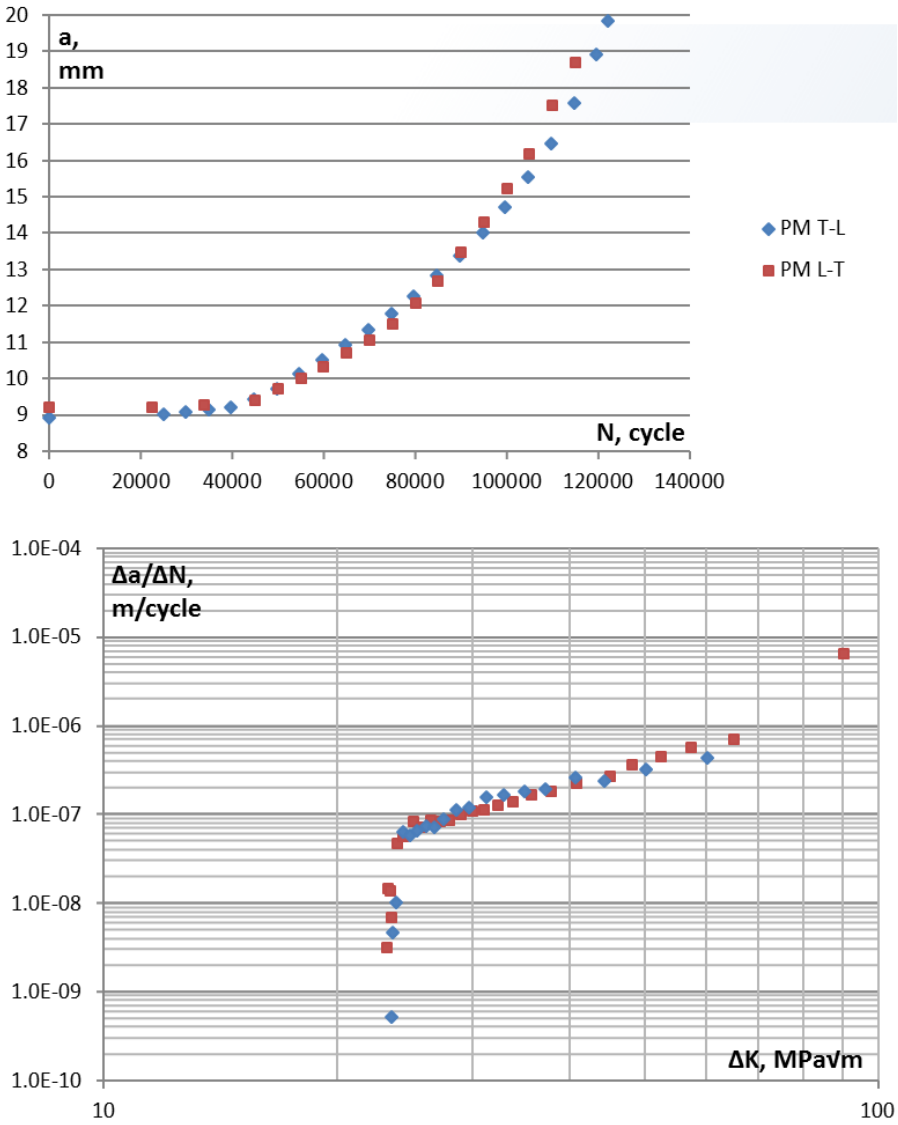

Figure 51. Graphs of crack length with respect to the number of cycle and crack propagation rate with respect to the stress intensity factor range; BM, R=0.1, 20 Hz and in laboratory air.

Fatigue crack propagation of wrought DSS in the solution annealing condition and L-T and T-L orientations has been studied by Tolungüç [104]. A couple of additional tests were executed to determine the Paris-Erdoğan coefficients (Figure 51). BM was tested only in laboratory air and with the frequency of 20 Hz. Wrought and as-welded DSS did not represent any diversity to the basic theory of FCP with respect to the fact that FCP rate of the material increases with the increase of stress ratio, R [131, 132], and that means FCP rate is sensitive to variation in stress ratio. In the present study, tests were executed with one stress ratio value being 0.1 for specimens of both BM and WM.

Processing the data, regression equations for BM were obtained as follows;

L-T; $\frac{\Delta a}{\Delta N} = 4.90 * 10^{-11}(\Delta K)^{2.27}$, (24)

T-L; $\frac{\Delta a}{\Delta N} = 2.00 * 10^{-11}(\Delta K)^{2.52}$, (25)

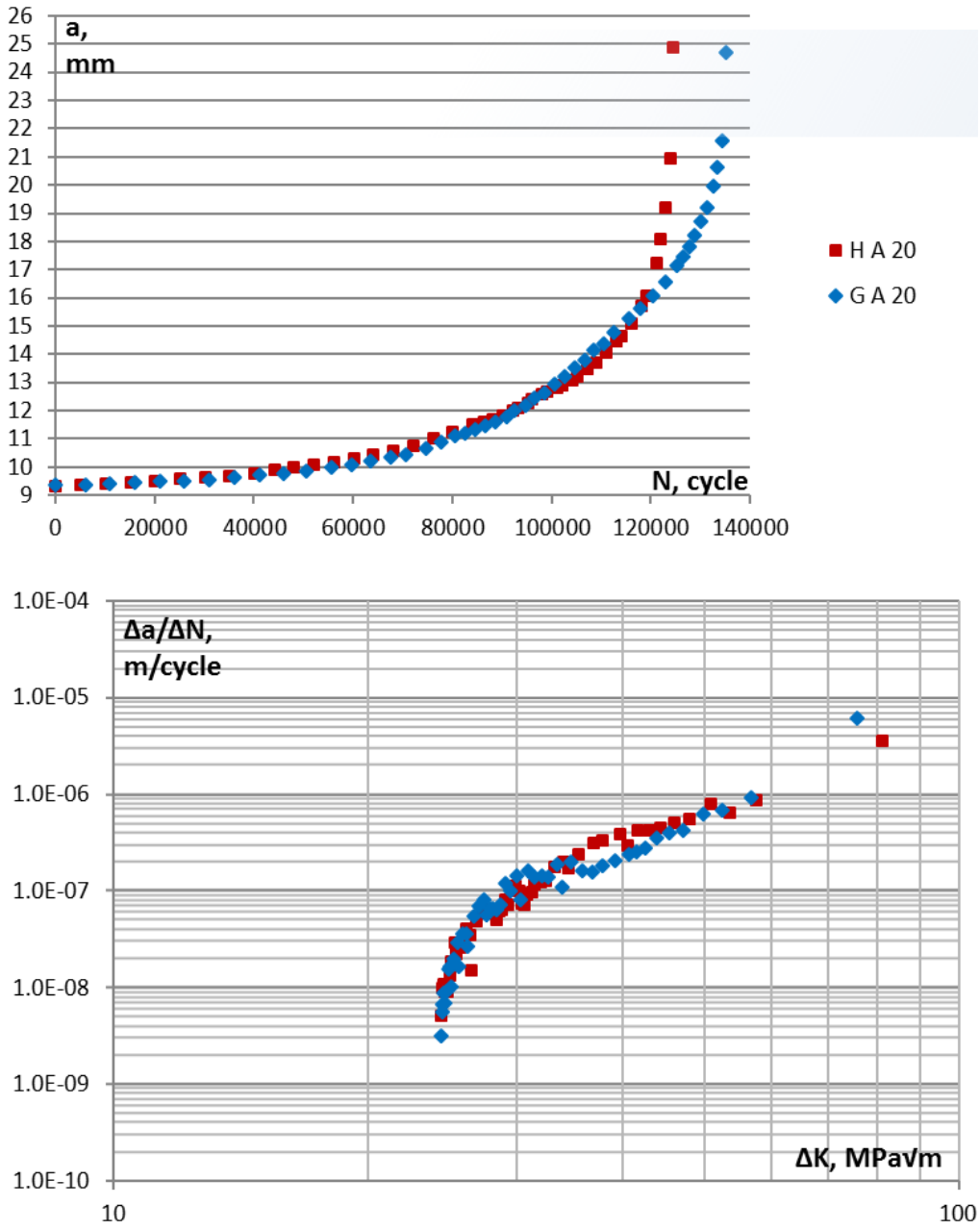

Figure 52. Graphs of crack length with respect to the number of cycle and crack propagation rate with respect to the stress intensity factor range; GMAW (blue dots) and HPAW (red dots), R=0.1, 20 Hz and in laboratory air.

Increments of the crack length (Δa) at nearly regular cycle intervals of ΔN were measured visually and especially near-threshold region, cycle intervals were kept at about 5000 cycles.

Therefore "Δa/ΔN" representation was preferred instead of da/dN throughout the manuscript, but technically these two representations were same as in usual cases.

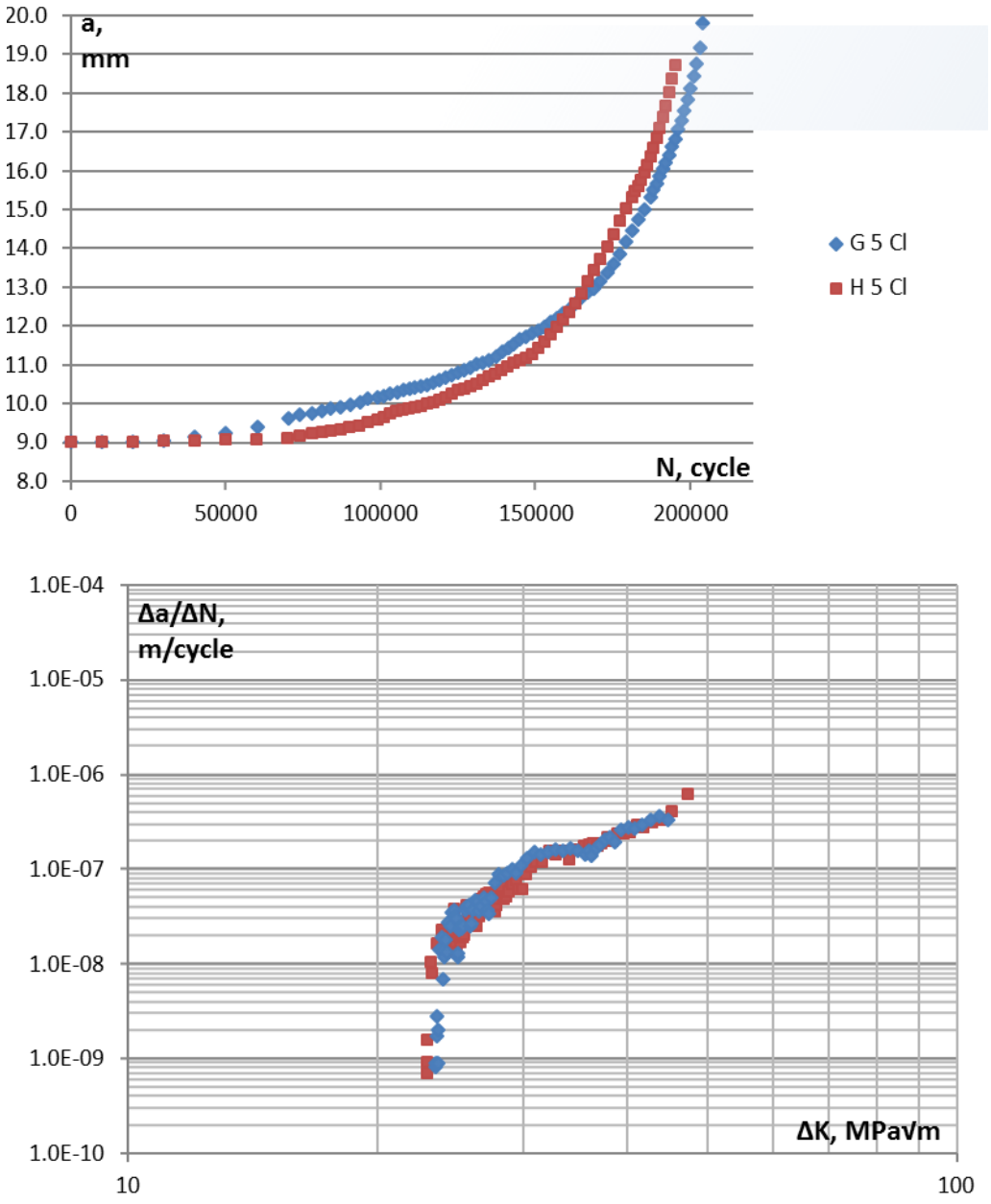

Figure 53. Graphs of crack length with respect to the number of cycle and crack propagation rate with respect to the stress intensity factor range; GMAW (blue dots) and HPAW (red dots), R=0.1, 10 Hz and in 3.5% NaCl solution.

CT specimens, which had welding joints in the middle were subjected to FCP test with three different testing conditions in terms of the environment (in laboratory air and under Cl^- attack) and the loading frequency (20, 10 and 5). Curves for the crack propagation progress

with respect to number of loading cycles and rates of crack propagation with respect to stress intensity factor range are represented in Figure 52, Figure 53 and Figure 54.

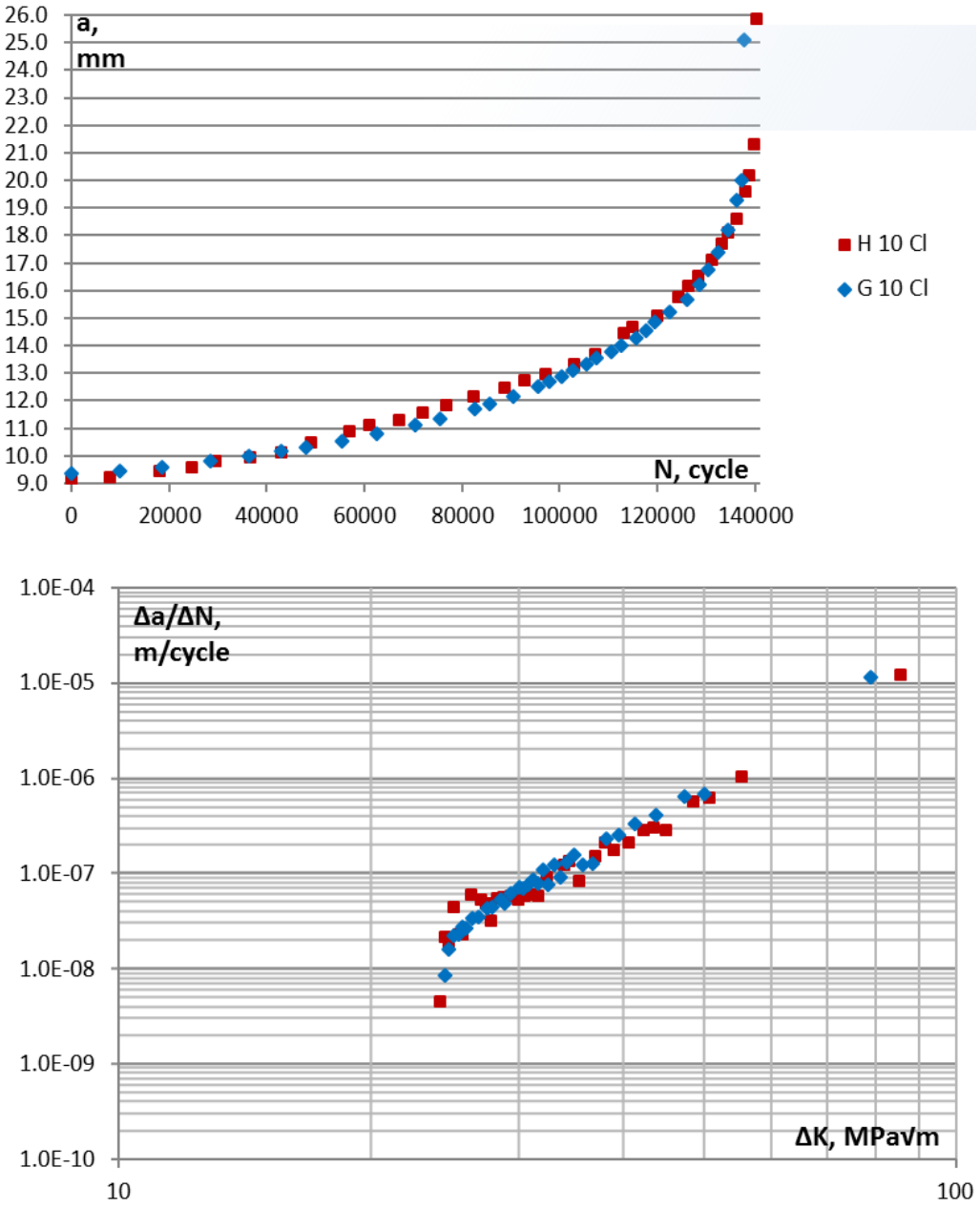

Figure 54. Graphs of crack length with respect to the number of cycle and crack propagation rate with respect to the stress intensity factor range; GMAW (blue dots) and HPAW (red dots), R=0.1, 5 Hz and in 3.5% NaCl solution.

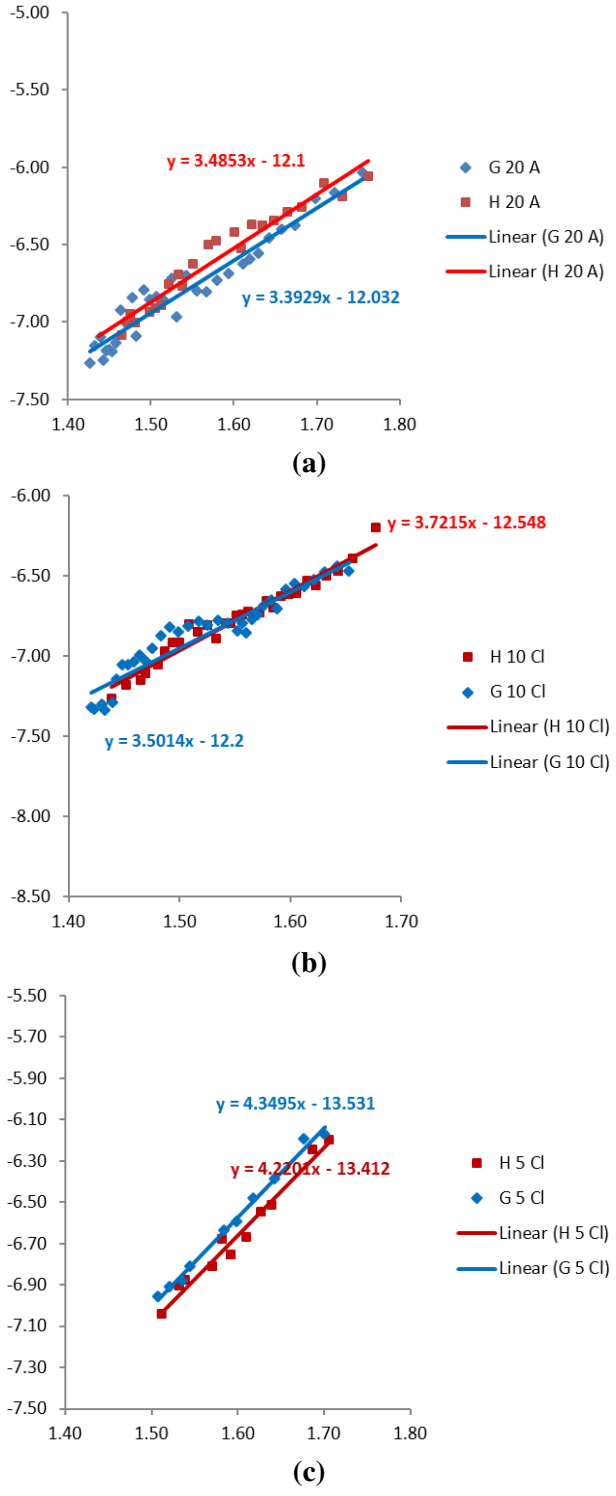

Figure 55. Graphs of crack propagation rate with respect to the stress intensity factor range in logarithmic scale; (a) 20 Hz in laboratory air {R^2_{G20A} = 0.9317, R^2_{H20A} = 0.9491}, (b) 10 Hz {R^2_{G10Cl} = 0.9568, R^2_{H10Cl} = 0.9053} and (c) 5 Hz in 3.5% NaCl solution {R^2_{G5Cl} = 0.9930, R^2_{H5Cl} = 0.9770}.

Testing conditions and codes of the specimens are tabulated in Table 12.

Table 12. Specimen coding followed during FCP tests.

	Welding Method	Environment	Stress Ratio, R	Loading Frequency, Hz
G A 10	GMAW	Laboratory Air	0.1	10
H A 10	HPAW			
G Cl 10	GMAW	3.5% NaCl		
H Cl 10	HPAW			
G Cl 5	GMAW			5
H Cl 5	HPAW			

Regression equations from the data of these WM tests were obtained and Paris-Erdoğan relationship parameters were calculated from the log ΔK versus log Δa/ΔN data (Figure 55) in accordance with the equation 17. The data is tabulated (Table 16) and graphically represented in Figure 84.

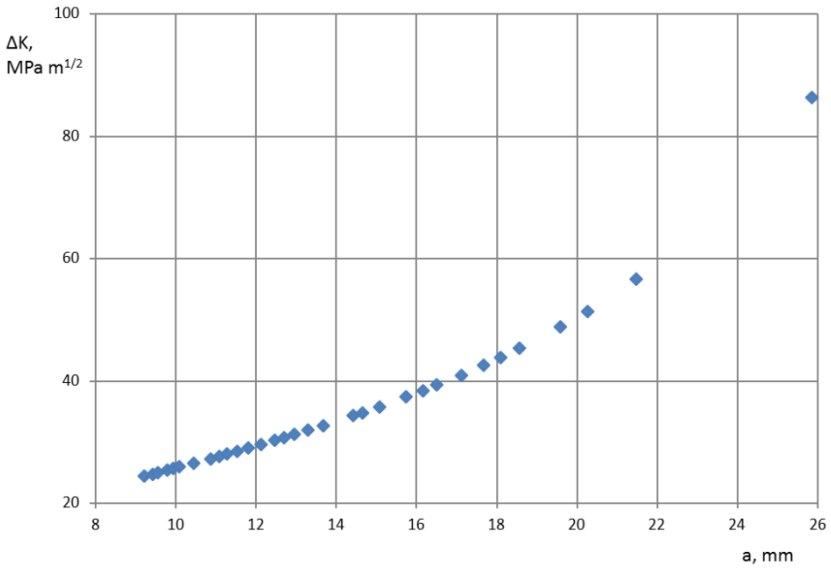

Figure 56. K-calibration (stress intensity factor range, ΔK, versus crack length, a) curve.

K-calibration was done using the applied-K (fixed-force crack-extension-force) curve for the specific specimen configuration employed in the present study. This curve was obtained to assess the effect of angular misalignment and/or residual stresses on ΔK to ensure that a comparison between GMA and HPA weldments would be rational. The curve relates the stress-intensity factor to crack size. Comer [129] observed a good agreement between the stress intensity factor ranges obtained from a 2D model (ANSYS) and manually calculated ones.

Comer [129] investigated the corrosion fatigue crack propagation resistance of a super DSS (Zeron 100) weld metals fabricated utilizing two conventional arc welding methods. He employed both ΔK-increasing and ΔK-decreasing methods during FCP tests. The investigation presented that the ΔK-increasing tests yielded more conservative ΔK_{th} values as compared to the ones from ΔK-decreasing tests Figure 57. Crack closure influence was considered to be the reason of such a difference in ΔK_{th}. With regard to the ΔK-decreasing method, ΔK_{th} was found at a relatively long crack length hence, closure due to contact between the fracture surfaces in the wake of the crack tip was significant. Unlike ΔK-decreasing method, a zone of residual tension remains after cyclic compression, therefore the crack propagates easier than through a zone that has compressive residual stress field. ΔK-increasing method was employed during the present research.

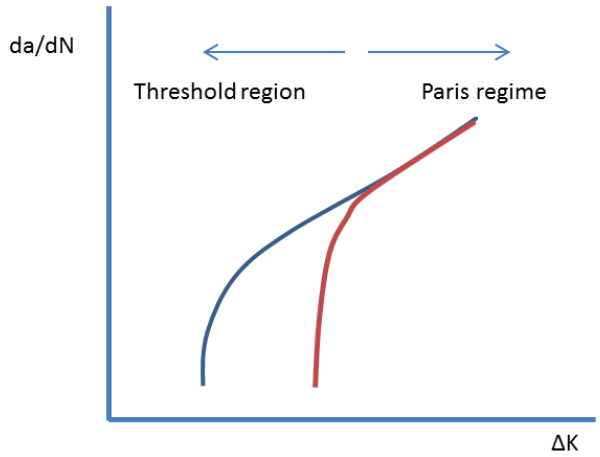

Figure 57. Schematic of ΔK-increasing (blue) and ΔK-decreasing (red) curves and corresponding representative ΔK_{th} values.

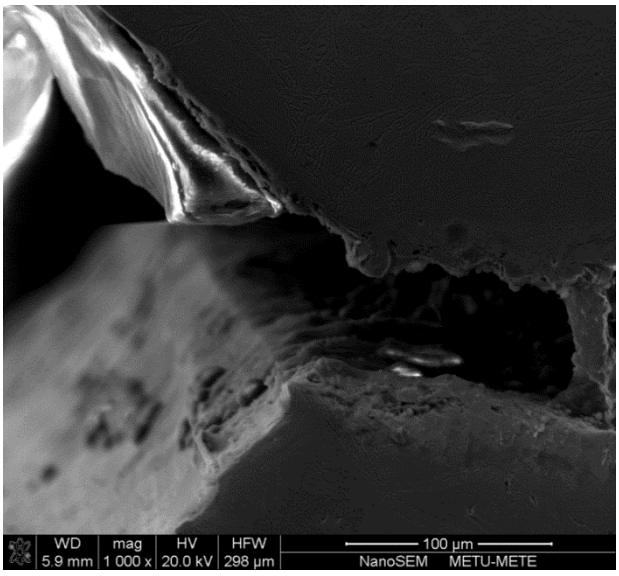

Figure 58. Beginning of the pre-crack at the tip of the notch in HPAW CT specimen.

Striations on fracture surfaces of some of the specimens that correspond to specific ΔK values were measured and Δa/ΔN recordings were investigated in terms of consistency. It was observed that data records were consistent especially at low crack propagation rates, where crack propagation was more stable (Figure 59).

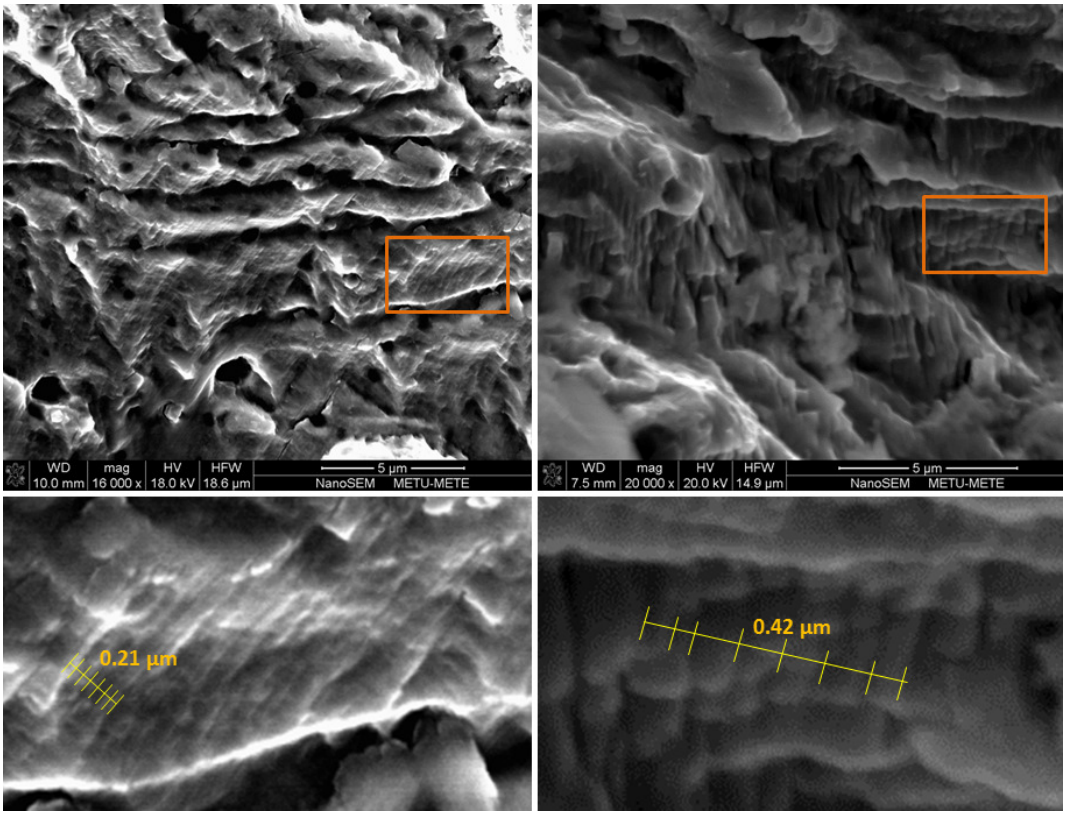

Figure 59. Striations in γ grains on the fracture surface of GMAW CT specimen.

The results firstly show that FCP rate in FZ of both weldments increases when the specimens are immersed in the sour environment. FCP resistance is the highest during the tests in air as far as the testing condition is concerned. Secondly, FCP rates for GMAW specimens are observed to be lower than HPAW specimens in air and under chloride attack at high loading frequencies, whereas rate for HPAW specimen is lower than that for GMAW specimen under chloride attack at low loading frequencies.

Final fracture surfaces of CT specimens in Figure 60 show that despite the loss of plasticity caused by the welding, the fracture surfaces still possessed ductility, as evidenced by the appearance of dimples, which are typical of ductile fracture. Micro-slag inclusions were observed in some of the dimples. According to EDX analyses, these particles were likely stable oxides and silicates, which were expected to be formed during welding process.

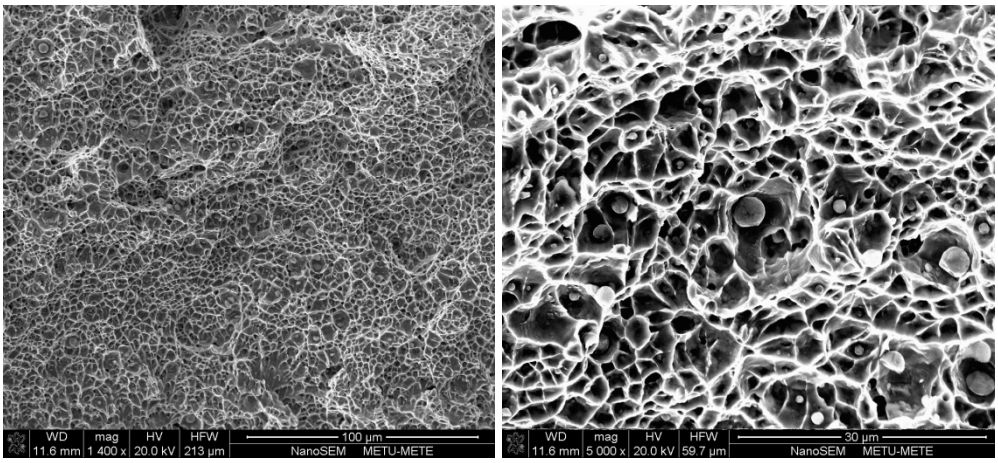

Figure 60. Final fracture surface of CT specimens. EDX analyses of the micro-slag inclusions provided the information that they could be stable oxides and sulfides of Mn and Si.

CHAPTER 5

DISCUSSION

5.1. General

Secondary austenite (γ_2) has controversial effect on mechanical and corrosion properties of DSS. Formation of the phase is normally inevitable in conventional melt-in fusion welding techniques and for thick plates of DSS since the welding process can only be completed in multi passes. Intragranular γ_2 does not precipitate during solidification of FZ. Successive passes apply a heat treatment to former ones and γ_2 precipitates in the heat-affected zone of these formerly solidified passes.

The role of γ_2 during FCP in air and sour service application has been the principal subject during this present study. A γ_2-free single-pass weldment was necessary for benchmarking. Single-pass welding of thick plates is only possible if a high-power-density fusion welding method is employed. On one hand, these welding methods lead to a keyhole, which provides a deep penetration and high depth to width aspect ratio. On the other hand, autogenous (without filler) keyhole welding is known to lead to excessive δ in as-welded DSS, so the principal problem becomes this improper phase distribution that may negatively affect the mechanical and corrosion properties of the material [130]. Autogenous welding process has to be followed by a proper solutionizing treatment [131].

Hybrid (keyhole + melt-in (conduction) modes) welding seemed to be promising since it might provide a single-pass weldment, which was free from γ_2 and had a proper phase balance due to proper degree of dilution of BM and filler metal consisting excess Ni at the same time [132]. Hybrid Laser arc welding (HPAW) method was the only mixture of keyhole and melt-in modes until the year 2004. And due to its high precision requirement for fitting-up of the pieces to be welded, the degree of dilution and consequently δ fraction in FZ are still question marks.

Matus and Zhang [133, 134] first proposed employing plasma and gas metal arc welding simultaneously to increase the operational efficiency. Dykhno and Ignatchenko [135, 136] developed a hybrid welding torch, which utilized a plasma arc, instead of a Laser beam, to obtain the keyhole. This recently developed product has been proved for non-alloy and low-alloy steels, but high-alloy steels.

Experimental studies and the results were described and introduced in the previous chapters. This chapter will focus on principally two subjects. Firstly, welding mode, heat and mass

transfer conditions will be discussed to prepare a platform for expressing the microstructural scenario, including phase transformations and solute redistribution, in as-welded DSS obtained using three different welding methods; GMAW and PAW, and their synergic combination, HPAW. Results of residual stress analyses, tension and impact toughness tests and hardness examinations will then be discussed. Finally, a discussion for FCP behaviors of HPAW and GMAW specimens will be constructed on the hardening phenomena.

5.2. Mode of Welding

As a conventional arc welding process, GMAW operates in conduction (melt-in) mode. During the conduction mode of welding, the arc tends to diverge through the spacing between the tip of the electrode and the work piece. Therefore the effective radius of energy density distribution is high and consequently the fusion effect is limited to surface and sub-surface of the work piece. 11-mm thick plates could be joined by 4 weld passes, namely a root pass, a fill pass and two cap passes during GMAW in conduction mode.

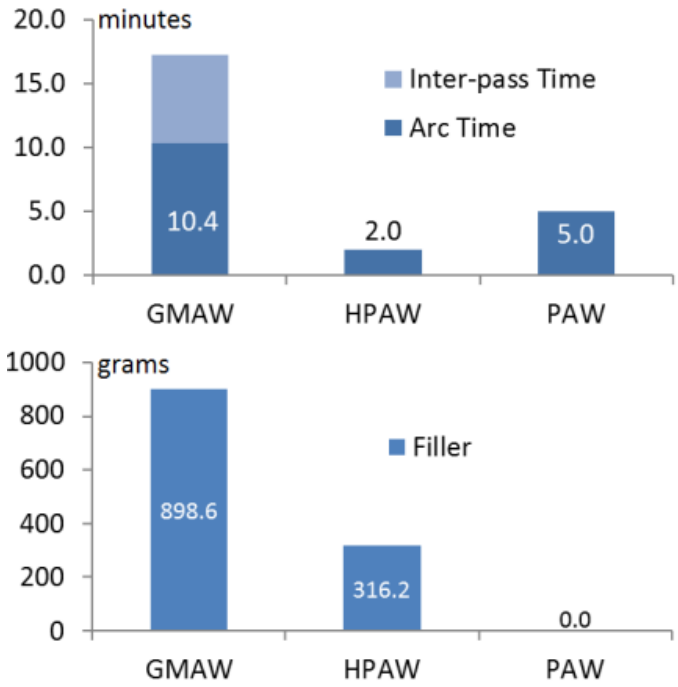

Figure 61. Comparison for welding efficiencies; process completion time in minutes and filler metal deposition in grams during the welding process.

Whereas, in PAW and HPAW, the arc in between the tungsten electrode and the work piece is constricted due to the converging action of the orifice gas nozzle. The plasma arc is technically columnar due to the constriction provided by the nozzle. This constricted arc leads to high specific point energies at the surface of the work piece, which yields a vapour column (keyhole) through the thickness of the work piece. The heat, which is produced by both the anode spot on the work piece and the plasma stream, can be deposited and

transferred below its surface during keyhole mode of welding. The keyhole turns the gradient of surface tension of the weld pool from negative to positive that is normally positive to negative in melt-in (conduction) mode of welding [25, 26, 137], therefore the mode of fusion welding is the principle determinant for the convection in weld pool and penetration as well. Utilizing the keyhole mode, joining the plates having thickness of 11 mm in a single pass was achieved during HPAW and PAW.

Sandor and Dobránszky [138, 139] attempted to prove these direct and reverse turbulences in 2205 DSS weld pool during regular (conventional) and activating flux aided versions of gas tungsten arc (or tungsten inert gas – TIG) welding operations. Utilizing pure argon (Ar) and argon-nitrogen (Ar + 5%N_2) mixture shielding and forming gasses, he commented that the activating flux altered the gradient of surface tension of the weld pool that yielded circulation kept toward the centre line, which is generally called reversed Marangoni convection. Based on the nitrogen sensitivity of the duplex phase balance he could conclude that reversed Marangoni convection increased nitrogen pick-up to the weld pool and consequently ferrite fraction was low and homogenous through cap to root of the fusion zone.

In the present work, nitrogen was involved neither in orifice nor in shielding gas, but the excess Ni in the filler wire would behave as the γ promoter. Fractions of primary phases, which were also homogenous in the present studies, presented that the excess Ni in the filler metal was introduced homogenously throughout the single-pass 11-mm thick weldment due to the reversed Marangoni convection conditions during HPAW.

5.3. Welding Efficiency

Keyhole based welding techniques (PAW and HPAW) provided significantly higher efficiency parameters as compared to that of the melt-in technique, GMAW. Deep penetration capability of the keyhole welding provided the possibility to work with narrower gaps and complete the joining process in a single run without an integrity problem. In the first place, reduced bevel angle for HPAW required less filler wire than the one introduced to the conventional V-groove. Pursuing this further, single-pass welding provided considerably less arc times and no inter-pass pauses, which are beneficial for economy of the welding process.

5.4. Cooling and Supercooling

The microstructure of as-welded DSS is caused by both phase transformations during solidification and consequent solid state transformations, which are mainly controlled by the composition of the material and the cooling rate. Cooling rate is determined by the heat input by the welding process and heat transfer conditions in the material.

Calculated cooling rates between 1200 and 500^{o}C and heat input values are given in Table 6. Taking the preheat temperature constant; cooling rates were inversely proportional to the heat and the size of the bead provided by the welding process. For typical plate dimensions and preheat temperature (20^{o}C), cooling rate of GMAW single-pass was higher than ones for

the single-pass of HPAW and PAW. Cooling rate of following GMAW passes decreased due to the inter-pass temperature of 180°C, but it was still lower than that of HPAW and PAW passes.

Relatively higher cooling rate during GMAW can be explained by both low heat input per each pass and 3-dimensional heat dissipation. However, the total amount of heat introduced during GMAW process was higher than that introduced during welding process of 11.1 mm-thick DSS plates using PAW and HPAW. This not only leads to a metallurgically less stable GMA weldment, but also relatively higher residual stress fields on the weldment (Figure 49).

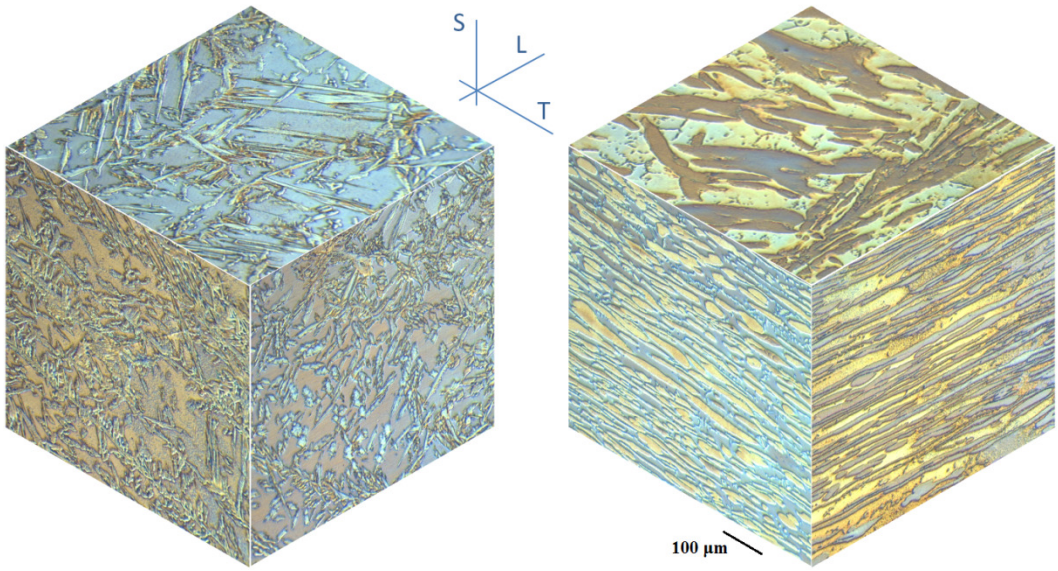

Figure 62. 3-dimensional views of microstructures of the as-welded (left) and wrought DSS Gr 2205.

Cooling rate is the principal determinant for the solidification structure of FZ and solid state phase transformations. In addition to the cooling rate, the soaking temperature and time during repeating weld thermal cycles also governs thermodynamics and kinetics processes in both FZ and HAZ. Therefore fractions of the primary phases (δ and γ) and secondary phases are consequently determined by the cooling and supercooling conditions during the welding operation.

BM is affected by the heat introduced by one cycle of thermal process during single-pass welding, like HPAW and PAW. Due to repeating thermal processes during a multi-pass welding operation, like GMAW, microstructural alteration in both FZ and HAZ becomes more complicated. Solidification structure, solute redistribution, phase balance and secondary phase formations will be discussed in following sections of the chapter.

5.5. Solidification Structure

All three weld metals had a typical DSS weld metal microstructure. Equiaxed grains at the weld centre and columnar grains at sides typically formed the weld metal structure of PA and HPA weldments, typical of competitive epitaxial growth (Figure 38 and Figure 41). Equiaxed dendritic structure in the middle of fusion zone indicates the relatively higher level of constitutional supercooling during the solidification. Equiaxed structure was more clearly observed in the centre line of the fusion zone of PA weldment, where solidification rates are higher than the one during HPAW.

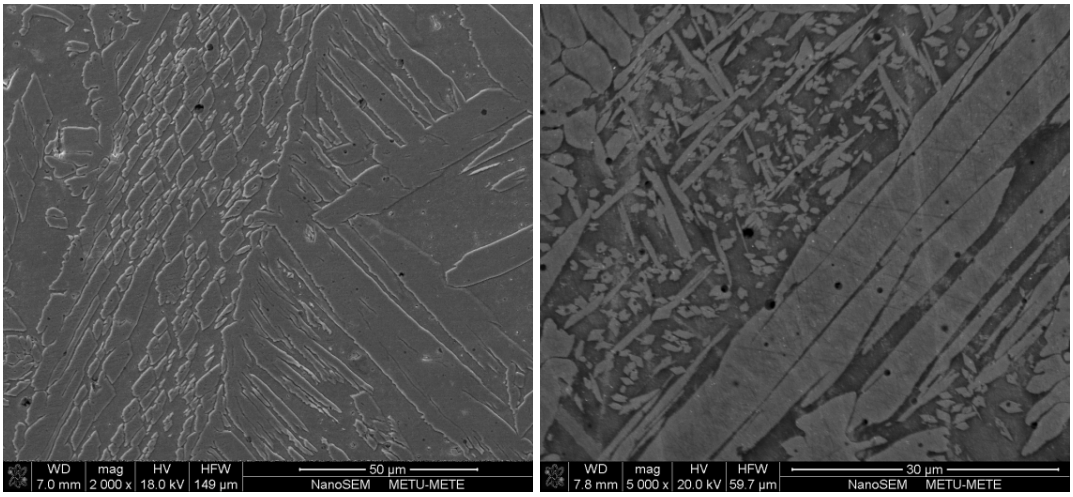

Figure 63. SEM images from FZ of HPAW (left) and GMAW (right) under low magnification. Single-pass HPA weldment is free from intragranular γ_2 precipitations, whereas intragranular γ_2 occupies about 20% of the reheated zones of FZ due to the heat treatment of successive weld passes.

Almost only columnar dendrites were observed in the fusion zone of GMA weldment. Columnar dendrites formed nearly perpendicular to the fusion line in all weldments. This indicates the maximum thermal gradient and so the characteristic of the heat flow, which is 2-dimensional in high-aspect-ratio beads obtained via keyhole formation and 3-dimensional in low-aspect-ratio beads in the GMA weldment.

Two major microstructural differences were observed in fusion zones of weldments obtained using single-pass keyhole (PAW) and multi-pass melt-in (GMAW) welding techniques. Firstly, it was observed that the columnar grains in the fusion zone of GMA weld have considerably smaller grain sizes than HPA and PA welds. Secondly, γ was observed in 2 different forms in FZ of PAW and HPAW, whereas 3 different forms in GMA weld metal. It precipitated incipiently as allotriomorphic austenite (γ_a) that served for the nucleation and precipitation of Widmanstätten austenite (γ_w) in all weldments. Formation of secondary (acicular) austenite (γ_2) within the δ grains in FZ of GMAW made the difference from the FZ of other two weldments.

The difference in columnar dendritic grain sizes might be explained by the difference in cooling rates. During continuous cooling, there is no enough time for the γ to precipitate until the temperature has decreased to about 1150°C, when a sufficient amount of nuclei has been formed at columnar δ grain boundaries [140]. Below that temperature, γ primarily precipitate as allotriomorphic form by a considerable diffusion rate of γ former elements like Ni and N. Diffusion significantly slows down in equilibrium conditions at about 450°C, therefore $\Delta t_{12/5}$ (cooling time in between 1200 and 500°C) parameter can be used to approach to the width of allotriomorphic γ as given in the following equation [57]:

$$W = A\,(\Delta t_{12/5})^{1/2}, \tag{26}$$

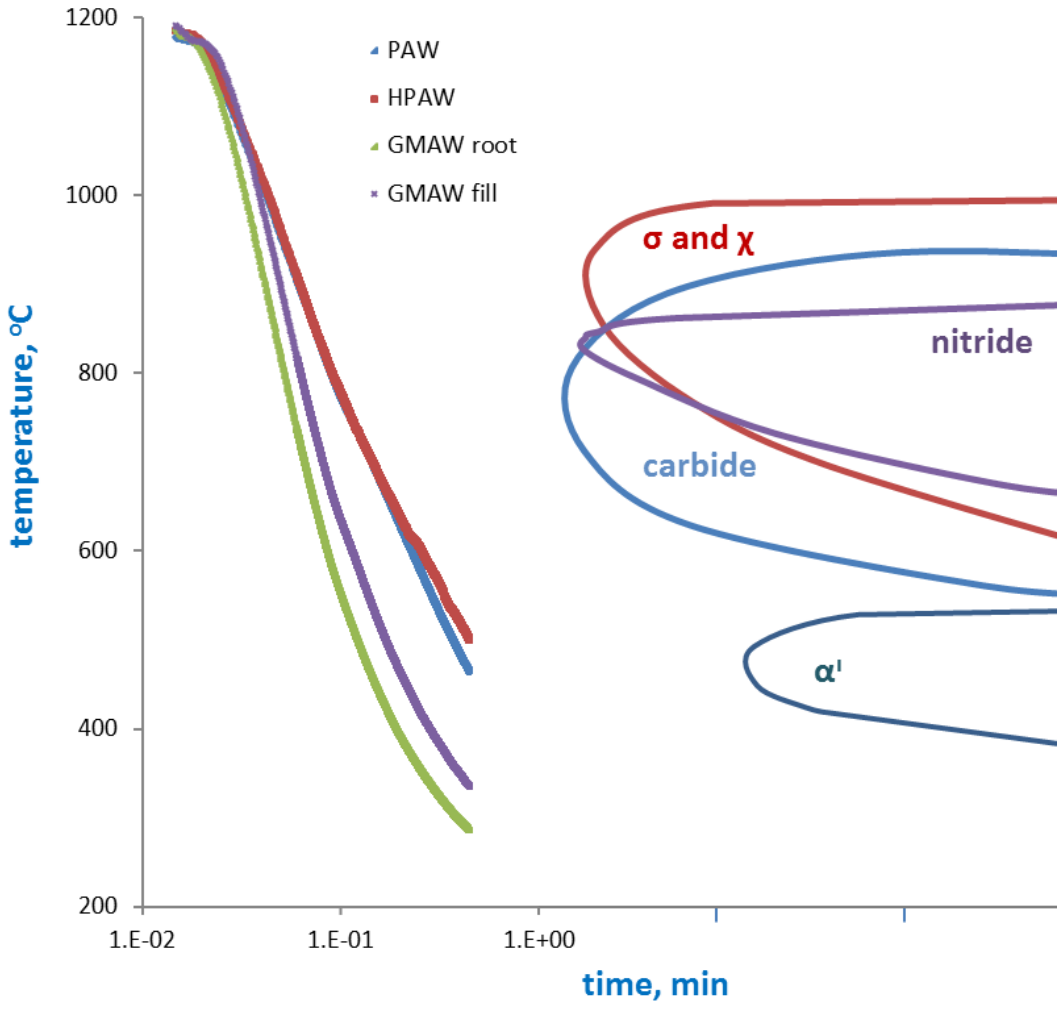

Figure 64. Reproduction of CCT diagram of DSS Gr 2205 and cooling curves of welding methods studied.

Using $\Delta t_{12/5}$ times for HPAW (25.8 sec), PAW (21.1 sec) and GMAW (9.3 sec) in the definition above, it was expected that allotriomophs in HPA and PA weld metals would be at least 1.7 and 1.5 times wider than the ones in GMA weld metal.

5.6. Phase Balance and Solute Redistribution

DSS weld metals, intended for use without post-weld heat treatment (PWHT), are over-alloyed in Ni, which is a γ former element, to ensure formation of a sufficient amount of γ. In this work, ER 2209 filler wire, which typically contains 9% Ni, was utilized during both GMAW and HPAW. On the contrary to these two techniques, no filler metal was utilized during PAW; this was an autogenous welding operation.

DSS solidifies first as columnar and equiaxed δ grains in the fusion zone. During continuous cooling, there is not enough time for the γ to precipitate until the temperature has decreased to about 1100°C, when a sufficient amount of nuclei has been formed at columnar δ grain boundaries [140]. Below that temperature, γ primarily precipitates as allotriomorphic form by a considerable diffusion rate of γ former elements like Ni and N. Diffusion significantly slows down in equilibrium conditions at about 600°C. After the reconstructive transformation of γ from δ, displacive transformation process starts to take place below 600°C. During this transformation process, γ precipitates as Widmanstätten plates toward the centre line of columnar grains. Kinetics of this process is determined by composition gradients in δ grains rather than diffusion of austenite formers, such as Ni and N. Since both allotriomorphic and Widmanstätten precipitates form during solidification of weld beads, they are called as primary austenite (γ_1).

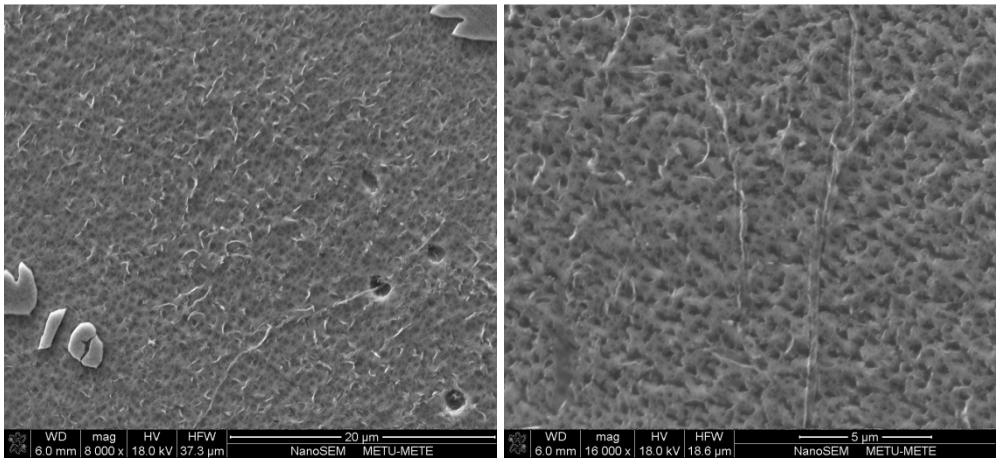

Figure 65. Colony of intragranular nitrides in PMZ and HAZ of GMAW.

Results of quantitative metallography studies and Ferritescope measurements are represented in Figure 41. Autogenous PAW yielded a fusion and a heat affected zone, which contented excessive δ. Ability to use filler metal with excess Ni promoted the formation of γ_1 in FZ under moderate cooling condition of HPAW and even under rapid cooling condition of

GMAW. The content of δ in the FZ is principally determined by both the chemical composition and the cooling rate. Elmer *et al.* [141] observed that the cooling rate dramatically altered the δ fraction through its influence on the amount of solute redistribution that occurred during solidification and through its subsequent influence on the extent of the solid-state transformation of δ.

Despite varying cooling rates, HPA and GMA welds had comparable amounts of γ_1. Moreover, cooling rates during HPAW and PAW were comparable but volume fractions of the phases in the fusion zones were substantially different. Therefore it can be interpreted as that the chemical composition of the weld metal is the dominating factor on the phase fractions rather than the cooling rates. The output of the research by Muthupandi *et al.* [9] supports this interpretation. Intensities of γ and δ peaks in diffractograms obtained from powder samples of the welds conformed to the metallographic observations and Ferritescope measurements. δ peaks had comparable intensities for GMAW and HPAW, whereas they had relatively higher intensities for PAW (Figure 42). The difference in the γ fractions in FZ of GMAW and HPAW was mainly due to γ_2 precipitates, which occupy almost 20% of the reheated zones of FZ.

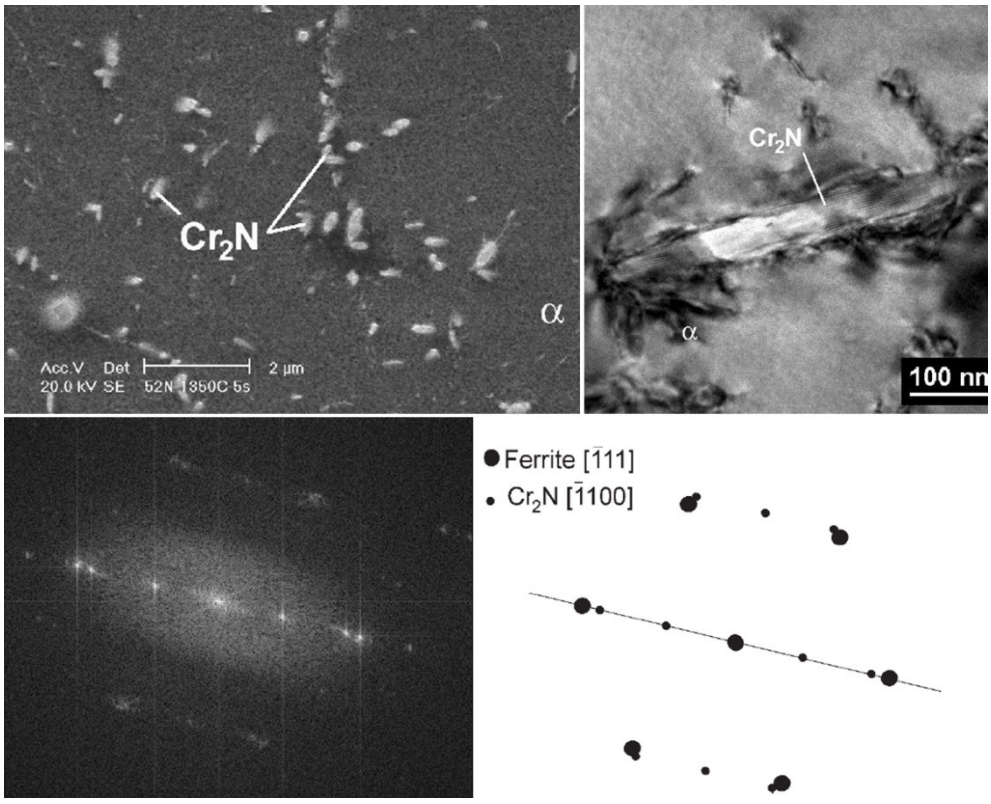

Figure 66. SEM and TEM investigation of a Cr2N rod from a nitride colony in the interior of δ grain in UNS S32550 [52].

δ and γ grains in fusion zones of all weldments were analysed using EDX to examine the solute distribution in as-welded structure. High-cooling-rate caused suppression of solute redistribution in FZ and partially melted zone (PMZ) of GMA weldment [52], where Cr-rich precipitates were observed either in δ grains or at δ/δ or δ/γ grain boundaries (Figure 65). Nilsson and Wilson [125], Kokawa *et al.* [55] and Ramirez *et al.* [52] characterized these precipitates as Cr_2N and reported that the hydrogen-induced cracking susceptibility increased as the density of these precipitates increased in the material. Despite its lower cooling rate, Cr_2N precipitates observed also in PA weldments, probably because autogenous welding caused insufficient austenite phase that could solubilize the entire available N.

Precipitation of γ_2 and Cr_2N and their relationship will be discussed in the following section.

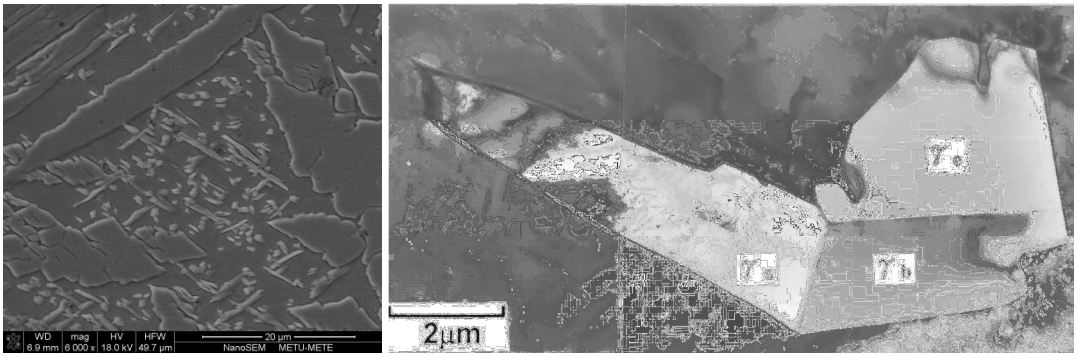

Figure 67. An intragranular γ_2 colony in FZ of GMA weldment and a high-resolution image of an individual γ_2 [142].

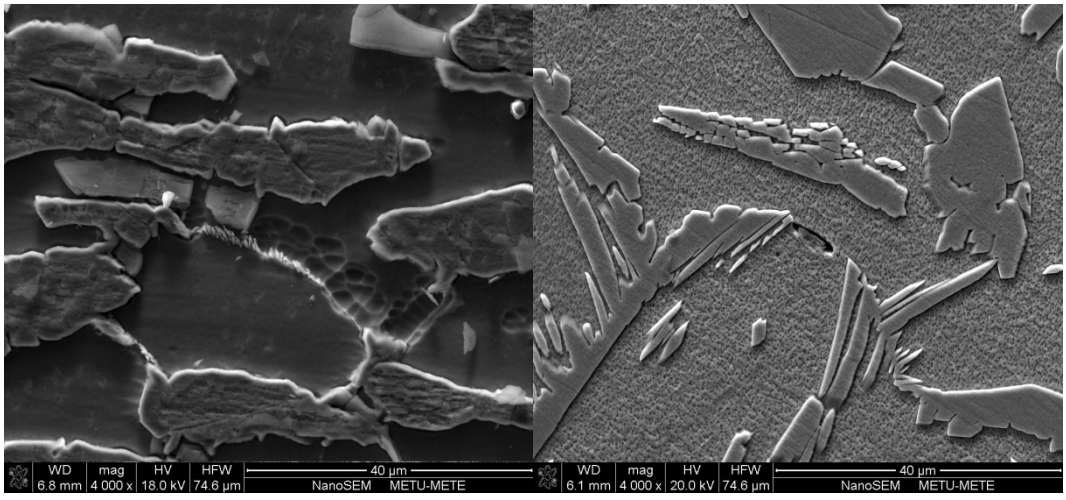

Figure 68. Intermetallic precipitates at δ/δ and δ/γ boundaries in HAZ of GMA weldment (left). HAZ of PA weldment that was free from intergranular precipitates (right).

5.7. Secondary Phases

Taking the inter-pass temperatures (180°C) into consideration, the specimen joined by GMAW was subjected to 4 heating cycles and kept over 180°C for about 5 minutes. Moreover, former passes (root and fill) were subjected to the heat treatment by GMAW cap passes, which motivated intragranular γ_2 nucleation and precipitation in acicular form (Figure 67) in the weld metal. However, acicular γ_2 formation could not be observed in HPA and PA weld metals and cap passes of GMA welds.

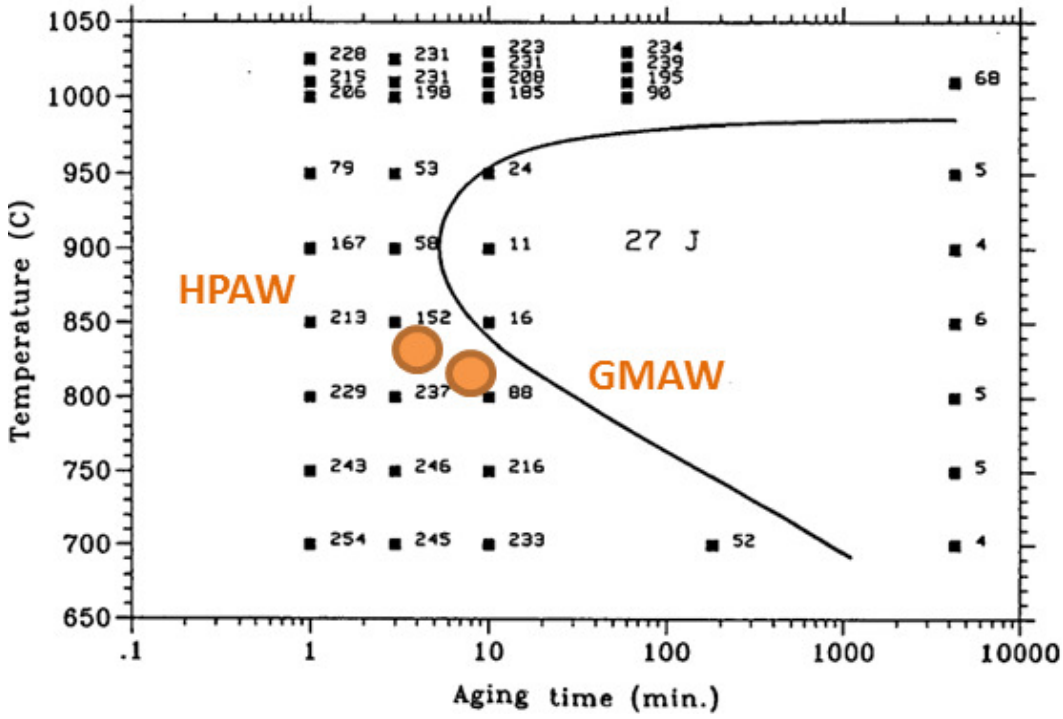

Figure 69. Impact toughness values of DSS specimens exposed to various aging treatments; the curve represents estimated conditions for the ductility limit that is assumed as 27 J [125].

EDX analysis of γ_2 (Figure 45 d) showed that concentrations of Cr and Mo were significantly low, which probably would lead to sensitization [105]. The γ_2 is transformed from δ via a martensitic shear process during repeating thermal cycles [108]. Chemical compositions and preferred orientations of γ and γ_2 are different and γ_2 had lower concentrations of Cr, Mo, and N than the γ [55]. γ_2 precipitates are expected to be more susceptible to pitting attack than γ [143].

Rapid cooling during the welding process leads to a metastable microstructure. δ grains are enriched in N above its solubility limit since there is insufficient γ, which could have

solutionized N, in the as-welded structure. When this metastable as-welded material is reheated by the successive passes during a multi-pass welding operation, dissolution of these intragranular nitrides takes place, where precipitation of γ_2 becomes possible [122, 52]. γ_2 is known to have controversial effects on mechanical and corrosion properties of DSS. On one hand, it improves the toughness of the material [123]. Precipitating intragranular γ_2 is even found to be a process that improves the mechanical properties of DSS [144]. On the other hand, the phase yields chemical inhomogeneity in the microstructure, consequently compromises the corrosion resistance of DSS [122]. Although the proposed heat input limits were obeyed during GMAW in the present study, solute redistribution was observed to be suppressed due to the high cooling rate of the process. As in a line with these former studies, PRE_N index were estimated to be 32.36 for γ_2 in FZ of GMAW, whereas the index was higher than 35 and even reached to 37 for the primary phases.

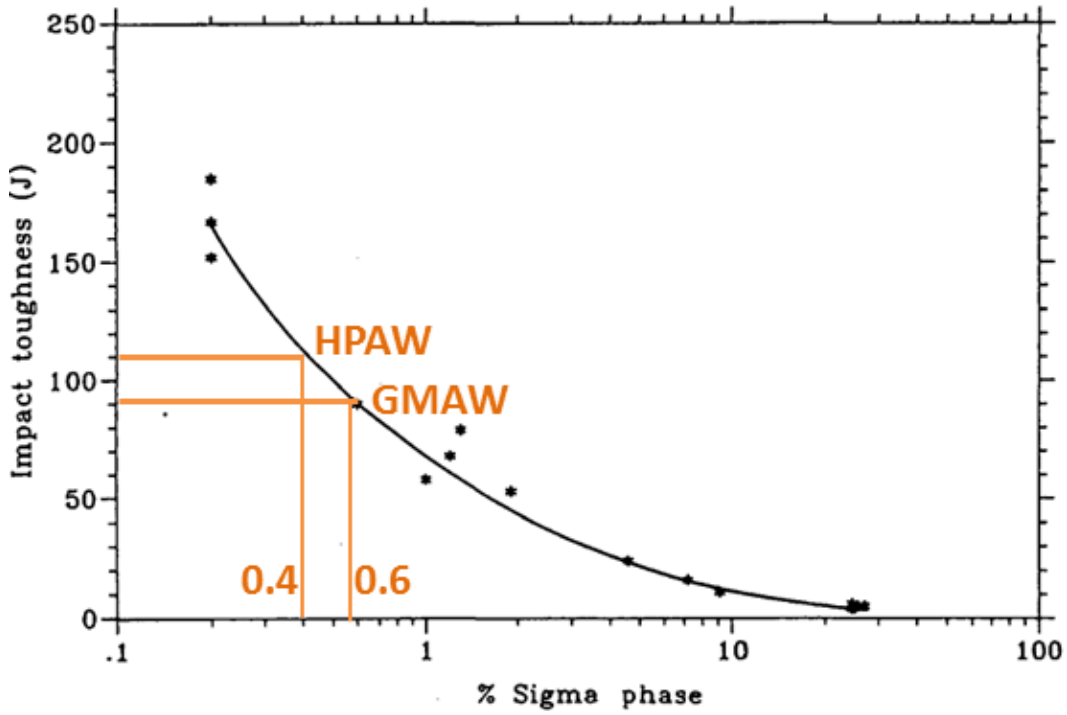

Figure 70.Variation of impact toughness with volume fraction of σ-phase [125].

Secondary phase formation is attributed to the repeating thermal cycles during multi-pass welding process. The temperature of a former weld pass increases above 600°C with the following passes, and this promotes solute redistribution and formation of intermetallic precipitates, as well as γ_2. On the one hand, duration of welding operations could be considered insufficient to drive the precipitation of intermetallic phases [145, 146]. On the other hand, Weisbrodt-Reisch *et al.* [147] observed that precipitation of σ took about 3600 seconds during annealing the DSS material at 800°C, whereas same annealing condition in combination with 1200 N mechanical loading initiated the decomposition of δ to σ and γ_2 in

only 360 seconds. Although the applied load was under the elastic limit, the specimens were plastically deformed due to creep process. During welding, thermal strains evolved in the DSS material and γ was expected to partly undergo dynamic recrystallization whereas δ softened by dynamic recovery that led to an energetically favourable arrangement of dislocations and sub-grains. The sub-grain structure might have enhanced diffusion processes, which governed reconstructive phase transformations [148, 149, 53].

Intermetallic precipitates were detected on δ/δ and δ/γ grain boundaries in GMA weldment during metallographic investigations. However, intermetallic precipitation was observed to be significantly suppressed in HPA and PA weldments. Like γ_2 precipitates, it was analysed that the formation of intermetallic phases also resulted in Cr and Mo depletion in the neighbourhood of them. Negative effects of these intermetallic phases on toughness and corrosion properties of DSS have been reported [5, 150, 151, 152].

Nilsson and Wilson [125] studied the effect of σ-phase fraction on the impact toughness property of DSS (Figure 69). Depending upon their investigation, it would be concluded that intermetallic precipitation was limited below 0.6% fraction during the present studies (Figure 70). In addition to this, intermetallic precipitates were observed more in HAZ than FZ. Therefore precipitation of intermetallic phases was not considered to have primary concern for FCP behaviour of the weldments. As a result, FCP discussion will mostly be based upon the controversial effect of γ_2 in air and sour environment as far as the secondary phases are concerned.

5.8. Hardening

Hardness, strength and impact toughness properties of weldments are given in the previous chapter, as well as microstructural features. Depending upon these data, hardening process is discussed in the present section. The discussion will be based on three hardening processes;

i. Strain hardening with respect to welding distortion and residual stresses,
ii. Precipitation hardening in terms of intermetallic phases, Cr-nitrides and γ_2,
iii. Substitutional and interstitial solid solution hardening.

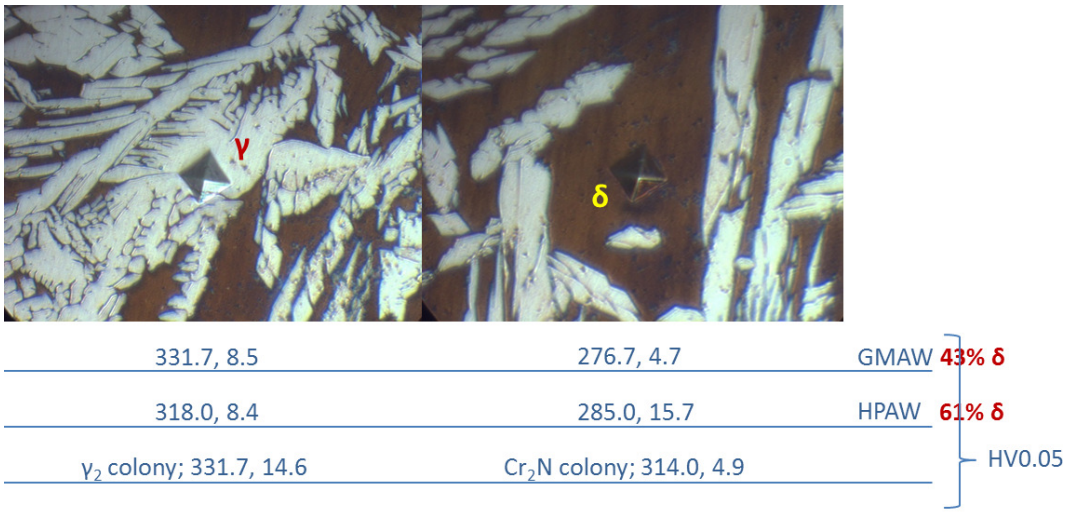

Figure 71. Micro-hardness values of individual grains of primary phases, δ and γ, and colonies of γ_2 and Cr_2N.

The hardness is defined as a measure of the resistance for a local plastic deformation [153], which leads to a stress field. The level of hardness, thus, varies according to the magnitude of stress field, which is introduced by either an external or an internal (residual) stress. Welding induces residual stress fields to the material, as well as surface treatments, such as shot peening, and material deformation processes, such as bending [154]. The thermal and mechanical residual strain in the as-welded material is the primary reason for strain hardening of the material.

Residual stress analyses of weldments in transverse and longitudinal directions provided data that were compatible to total heat input values of welding operations. GMAW introduced the highest total heat input and produced the highest tension and compressive residual stress magnitudes in its weldment.

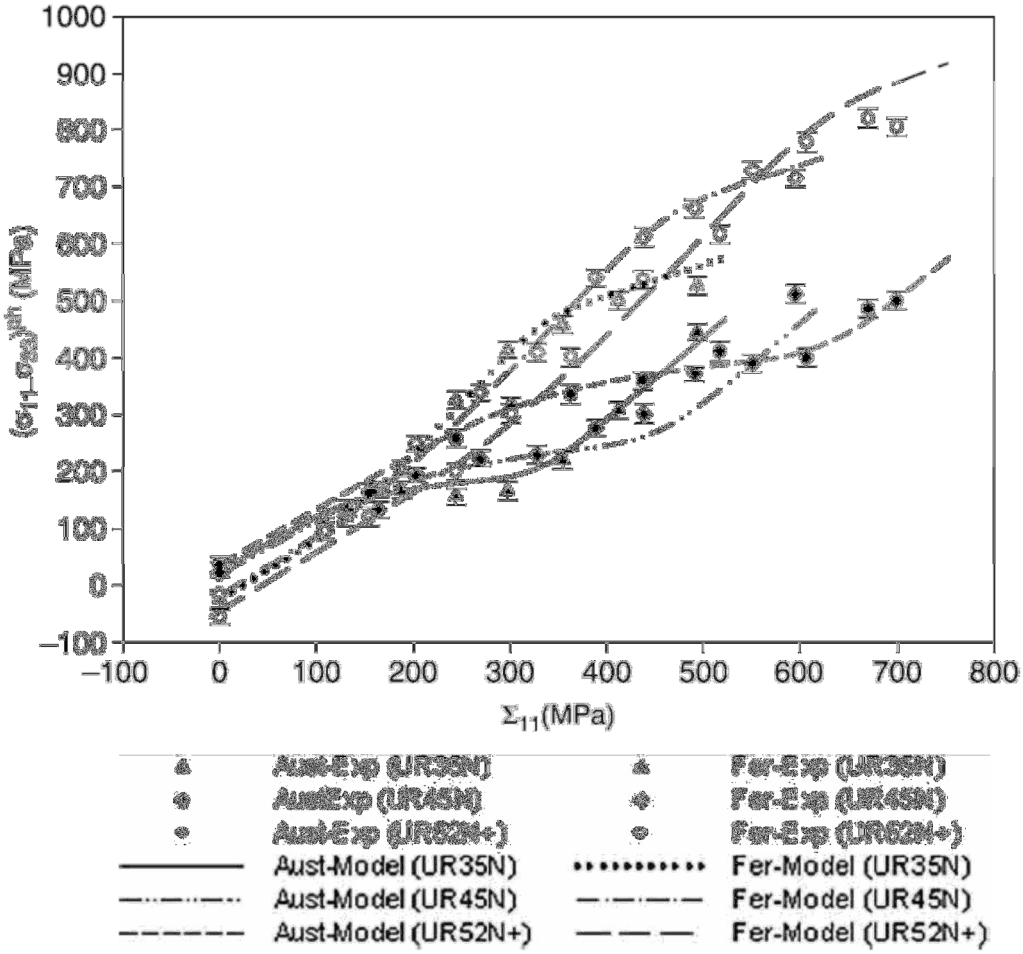

Figure 72. Tensile testing results and comparisons with the model predictions for the steels studied by Dakhlaoui et al. [158]. The evolution of stresses in both phases is represented. Measurements were performed by X-ray diffraction. Chemical compositions of the materials are presented in Table 13.

Hardness increases in the compressive stress field and decreases in the tensile stress field. PAW led to significantly lower residual stress field as compared to HPAW and GMAW. The highest residual stresses were observed in GMA weldments in both tensile and compressive fields. The magnitude of the tensile residual stresses in GMAW HAZ was higher but comparable with the magnitudes as in HPAW. The tensile stress field was observed to span wider area in GMA weldment, and this means thermo-mechanically affected zone of GMA weldment was wider. Nevertheless, residual stress field existing in the middle of FZ is more worth to interest concerning FCP behaviour of CT specimens centred at FZ.

δ and γ phases in DSS have a different response to a thermal strain during heating and/or cooling in a welding process due to their different thermal expansion coefficients. It is known that the micro-stresses are generally tensile in γ and compressive in δ because of the higher yield strength and higher hardening capacity of γ [155, 156]. Micro-hardness measurements of γ grains in the present study confirmed that γ hardened more than δ (Figure 71).

Mean hardness of σ-phase is mentioned as 800 HV in literature [157]. Nilsson *et al.* [122] observed that the hardness was constant until 10% volume of secondary phases and started to increase above that volumetric fraction. Intermetallic phases, such as σ and χ, prefer to precipitate in δ grains and at δ/γ grain boundaries. The average hardness in δ grains in the HPA and GMA weldments were recorded as 285.0 and 276.7 HV0.01 respectively (Figure 71). In combination with the impact toughness data, only neither spinodal decomposition nor precipitation of hard and brittle intermetallic phases could provide a reasonable explanation for relatively high hardness values of GMAW. Furthermore, the presence of intermetallic phases could not be clearly confirmed by XRD probably due to low volumetric fractions of them (Figure 48).

Micro-hardness examinations were also focused on the colonies of γ_2 and Cr_2N precipitates where hardness values were found to be higher than the ones obtained in untransformed δ grains. As far as the secondary phases concerned, not intermetallic precipitates, which have low volumetric fractions and are sparsely distributed, but γ_2 and Cr_2N precipitates may be found to be a considerable reason for the precipitation hardening.

Relatively lower energies for fusion line of GMA weldment then the ones for HPA weldment would be attributed to the precipitation of brittle intermetallics. Calliari *et al.* [157] obtained a correlation between the volume fraction of secondary phases and impact toughness. They commented the main drop in toughness was due to the early stages of precipitation when the only phase detected was χ-phase and σ-phase was still virtually absent. Cleavage areas on the fracture surfaces of V-notched charpy specimens corresponding to δ grains in HAZ of the weldments can also be associated to the embrittlement caused by intermetallic phases (Figure 50). But as discussed above, due to their very low percentages, hardening due to brittle intermetallic phases are not considered to as the primary concern.

Table 13. Chemical constituents (wt%) in the DSSs studied by Dakhlaoui et al. [158].

Designation	**Grade**	**Cr**	**Ni**	**Mo**	**N**
X2 Cr Ni 23 4	UR35N	22.79	4.58	0.17	0.094
X2 Cr Ni Mo 22 5 3	UR45N	22.4	5.4	2.9	0.17
X2 Cr Ni Mo Cu N 25 6 3	UR52N+	25.18	6.46	3.78	0.251

Impact toughness energies obtained from the specimens, in which V-notches were centred at the weld metal and fusion lines of PA, HPA and GMA weldments were represented on Table 11. PAW yielded toughness energies lower than the ductility limit at -50^{o}C because of very high δ content (> 70%) in the weld metal microstructure.

Increasing the N content in DSS has been the most important improvement in modern grades in terms of their mechanical and corrosion properties. N content of the material governs the hardness and ductility of γ phase [159, 83]. Substitutional elements, such as Cr, Ni and Mo,

also have direct and indirect effects on the macro and micro properties of DSS. The effect of the weight fractions of substitutional (Cr, Ni, Mo) and interstitial (N) elements on yield strengths of both phases in three different DSS (UR35N, UR45N and UR52N+; Table 13) can be seen in Figure 72. Dakhlaoui *et al.* [158] observed that increasing the content of N, Cr and Mo, initial hardening of both phases increased.

5.9. Fatigue Crack Propagation

As far as the FCP behaviour is concerned, HPAW has been a good benchmarking to conventional multi-pass arc welding techniques, because it led to,

- comparable but less macro and probably less micro residual stresses in the weldment than the one fabricated using GMAW,
- slightly higher δ fraction, which was under the limits proposed, in FZ,
- relatively lower cooling rate due to 2-dimensional heat dissipation and consequently more balanced solute redistribution, and
- an as-welded DSS that was free from γ_2 and significantly supressed intermetallic precipitation.

This section will be structured through sub-sections, in which these phenomena and their effects will be discussed.

5.9.1. Residual stress effect

Practical experience has indicated not only external stresses introduced during service but also internal stresses accumulated during fabrication processes, such as machining, bending, welding and heat treatment are effective for fatigue performance of the assembly [160, 161]. Surface and sub-surface stresses are also a governing factor for the crack propagation.

Residual stresses were observed to occur in all three weldments, GMAW, HPAW and PAW, because of incompatible thermal strains caused by heating and cooling cycles during the welding operations. Post-weld stress relieving heat treatment was not applied to these weldments because investigating the effect of γ_2 was the primary concern, and if any thermal treatment was to be applied, γ_2 would have precipitated in δ grains in FZ of HPAW and PAW. In fact, γ_2 would be assessed as the primary factor that affects micro residual stress conditions [162] and changing the microstructure with respect to γ_2 would make impossible to see its controversial effect on FCP in both air and sour environment.

The residual stress distribution along the width (perpendicular to the weld line) and length (parallel to the weld line) of the welded plate is shown in Figure 73. The tensile residual stress field makes a maximum at the fusion line and nearby of it through both FZ and HAZ. In opposite to the GMA weldment, these tensile residual stresses make a minimum in the centre line of the weldments. A compressive residual stress field was observed through the centre line of the GMA weldment and the magnitude of the field increases in the direction of welding progress.

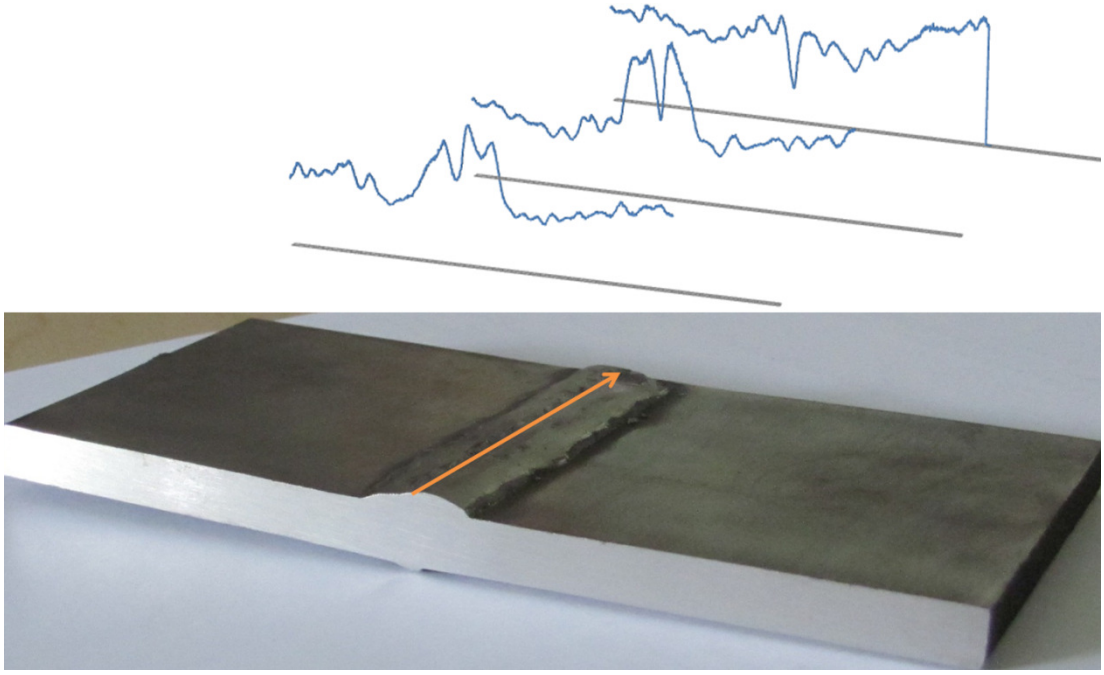

Figure 73. Presentation of residual stress distributions through the plate in two orientations, parallel and perpendicular to the joint line.

It is known that, compressive residual stresses retard the FCP progress [163]. Figure 74 represents an example of the records of fatigue crack closure. In the figure, difference between the lines indicates the modified crack opening displacement with the unloading elastic compliance method, as defined in the following relation;

$$\phi^{\iota} = \phi - \alpha P, \tag{27}$$

where ϕ is the crack opening displacement, ϕ^{ι} is the modified crack opening displacement, P is the load signal and α is the compliance of the cracked specimen.

Parry *et al.* [164] intended to investigate the effect of residual stresses on FCP in as-welded materials. They noticed that stress-relieving heat treatment had no considerable effect on FCP rates under tension-tension loading. Young *et al.* [128] pointed out that residual stresses were more effective on FCP than the microstructural factors; however they concluded that the redistribution of residual stresses during FCP tests should also have taken into the consideration. Shi *et al.* [165] described the welding residual stress redistribution in CT specimens and the crack closure concept. They also observed that welding residual stresses were indicative for FCP rate especially if the crack path was perpendicular to the joint line rather than parallel to it.

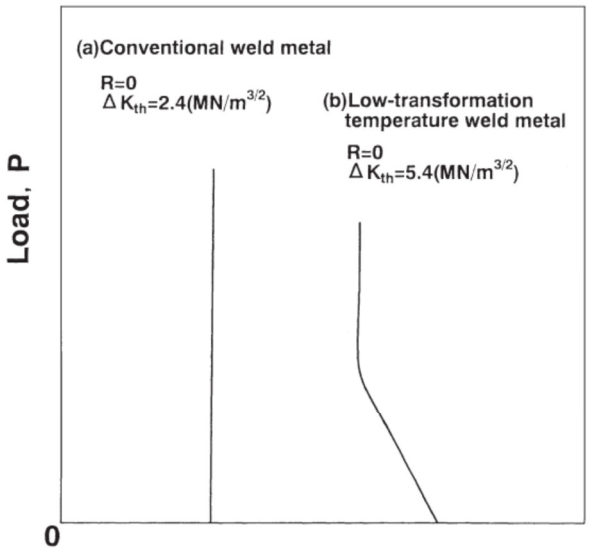

Figure 74. Records of fatigue crack closure by Ohta et al. [163].

On one hand, the compressive residual stresses were noticed as an advantage for GMAW specimens, especially for low ΔK data. On the other hand, machining a notch in the specimen, elastic redistribution of the stresses was expected [166]. Furthermore, residual stress relaxation that occurs during crack propagation [167, 168] was also beyond our observations, and has to be investigated through a case-specific project in the future.

In the present study, the purpose of the residual stress analyses was framed in selection of the CT specimen location throughout the weld lines, obtaining a general impression about the macro and micro residual stress conditions, and their strain hardening consequences. CT specimens were sectioned from the parts of weldments where amplitudes of residual stress fields were as low as and as comparable as possible. Strain hardening conditions as a consequence of micro stresses will be involved in to the discussion in following sub-sections.

5.9.2. δ/γ phase balance effect

Hardness of GMA weld was considerably higher than HPA and PA welds. It was detected by the micro-hardness examination that, relatively higher hardness values of the GMA weldment were due to the higher hardness values obtained at both δ and γ grains. Comparable macro residual stress fields at FL and HAZ of HPA and GMA weldments support the argument that precipitation hardening (secondary phases), solid solution hardening (solute redistribution) and strain hardening are principal determinants for the hardness, toughness and consequently FCP behaviour of as-welded DSS in air, as well as the phase balance and grain size. In addition to their involvement to the hardening, precipitation of secondary phases yield chemical imbalance in the material, hence have indirect effects on corrosion fatigue processes.

Table 14. Changes in the yield strength of DSS and its individual phases after cold working and aging processes [155].

		%	σ_y		
			AR	8%	Aged
γ		57.1	425	805	420
δ		42.9	565	555	675
Bulk	Experienced		545	705	610
	Calculated		485	682	529

Strain hardening of as-welded plates was expected due to the thermal residual strain. It is known that δ is influenced more markedly than γ during aging processes because mobility of solute elements is higher in δ, where precipitation of secondary phases is more favourable (Table 14). Besides, strain hardening capacity of γ is higher than the one of δ (Table 14). Therefore, strain hardening effect was attributed more to γ grains. Micro-hardness readings went along with magnitudes of the residual stress fields existing in the weldments. γ grains in FZ of GMA weldments were observed to be hardened more than the ones in FZ of HPA weldments (Figure 71). Whereas, no considerable difference in the hardness was observed between δ grains in FZ of GMA weldment and the ones in FZ of HPA weldment.

Despite the difference in the hardness of primary phases, there was no preferential path for crack propagation during the tests in the laboratory air (Figure 75 and Figure 76). Cracking was mostly intragranular in both weldments. Secondary cracks were also present, and propagated both in δ grains and at δ/γ grain boundaries (Figure 77). The principle crack propagation micro-mechanism in air was the striation forming in γ grains. Some cleavage is also observed at δ grains (Figure 77).

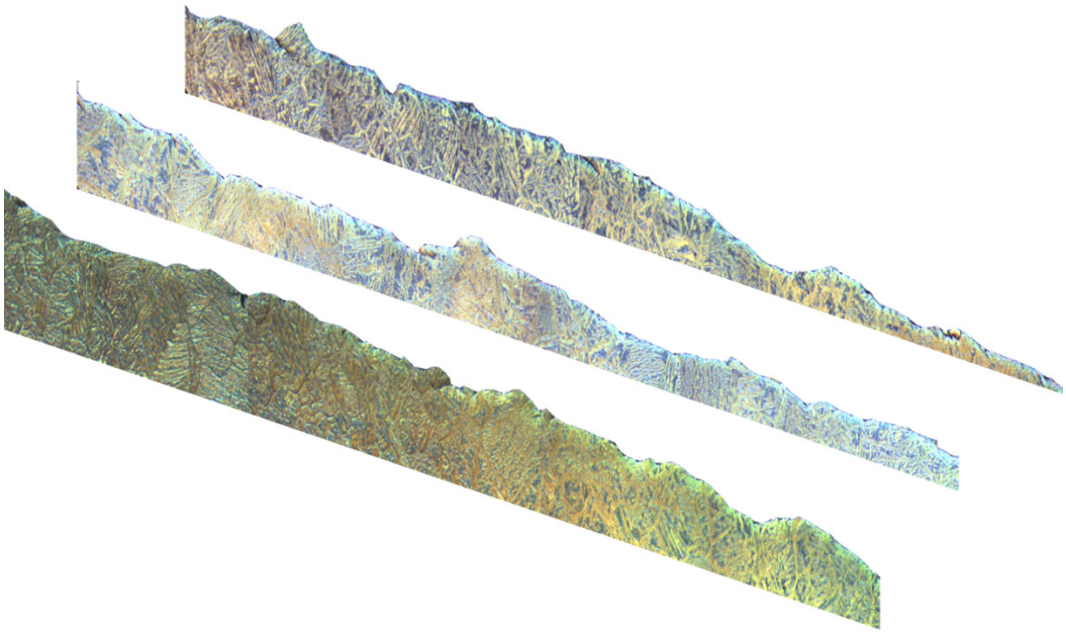

Figure 75. Three different sections sliced from the same weld metal CT specimen. No preferential path for crack propagation progress was observed concerning different phases.

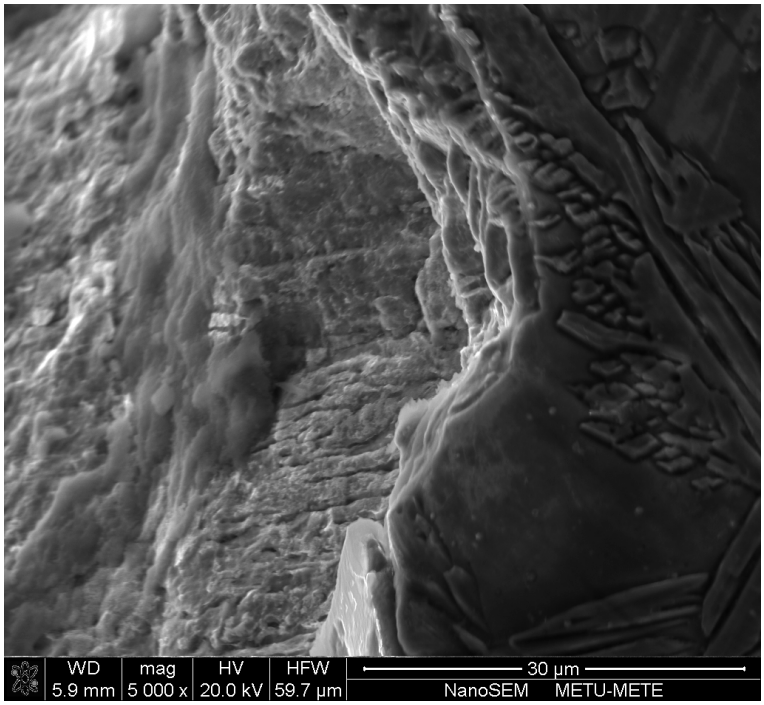

Figure 76. A high magnification side view of the fatigue crack.

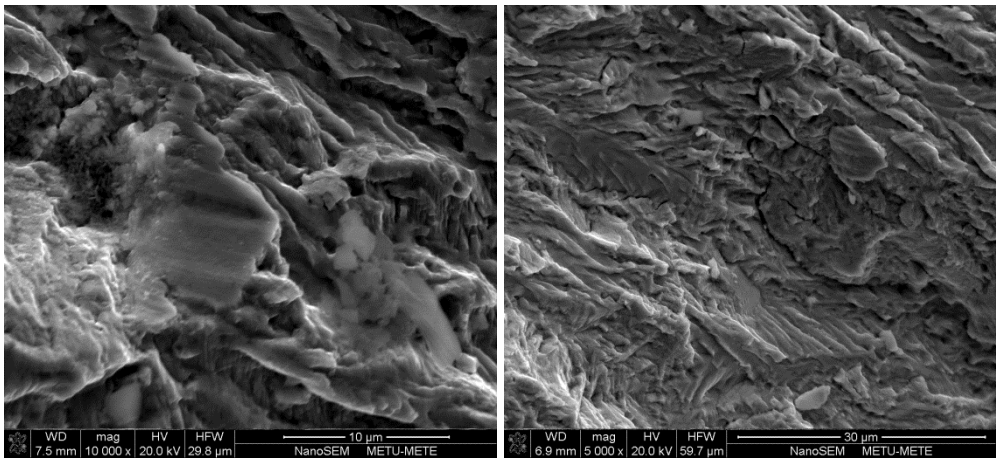

Figure 77. Cleavage at δ grains (left) and secondary cracks through δ grains of δ/γ grain boundaries (right).

Petrenec et al. [173] investigated and compared the dislocation structures in super DSS specimens fatigued to fracture using uniaxial and biaxial cycling loadings with the equivalent strain amplitude. Figure shows the dislocation structures at γ and δ grains in DSS specimen fatigued in symmetrical tension-compression. Dislocation rich and free bands in the grains can be seen. The bands are parallel to {111} in γ grains and primary and secondary slip systems were observed to be (111) [-101] and (-111) [101] respectively, whereas the dislocation structures presented variability in δ grains and mostly vein structures were documented. The difference of the dislocation structures were related to the variation of the active slip systems in both phases by the researchers. FCC lattice of γ leads to only one active slip system and consequently a planar arrangement is produced [174].

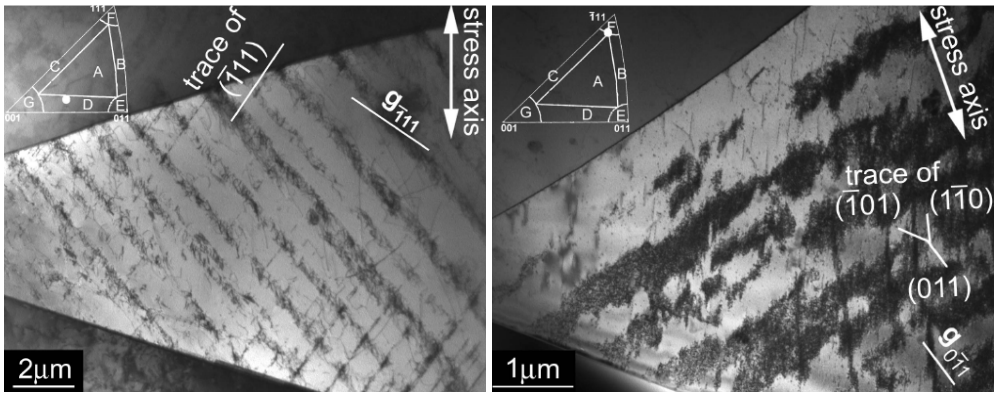

Figure 78. Planar arrangements in γ grains (left) and loop patches of dislocations in δ grains [175].

During examinations on side views of specimens sectioned from both weldments, plasticity marks were only revealed on γ phases at low ΔK values (Figure 79). At high ΔK values, not

only the abundance of these marks increased but also δ grains also contributed to the plastic deformation.

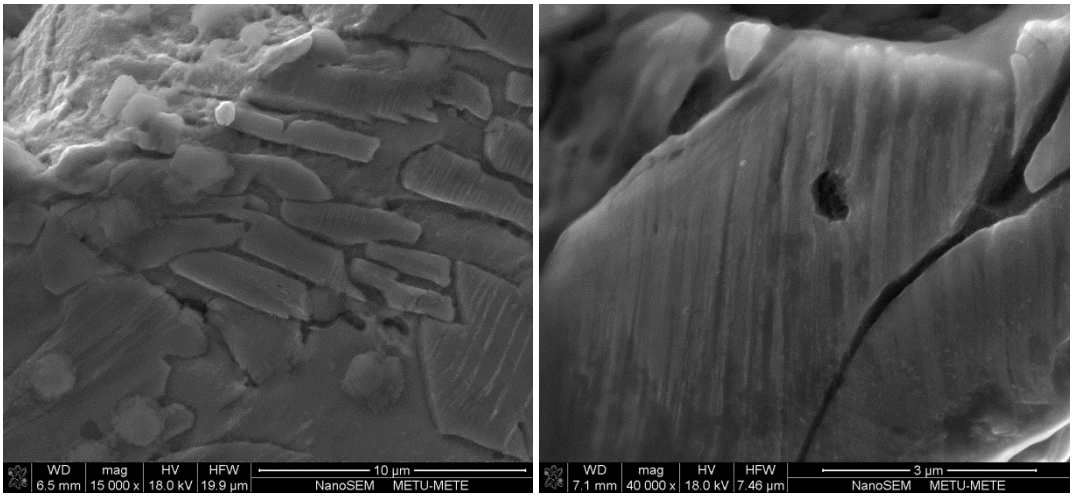

Figure 79. Slip bands on γ grains observed using SEM.

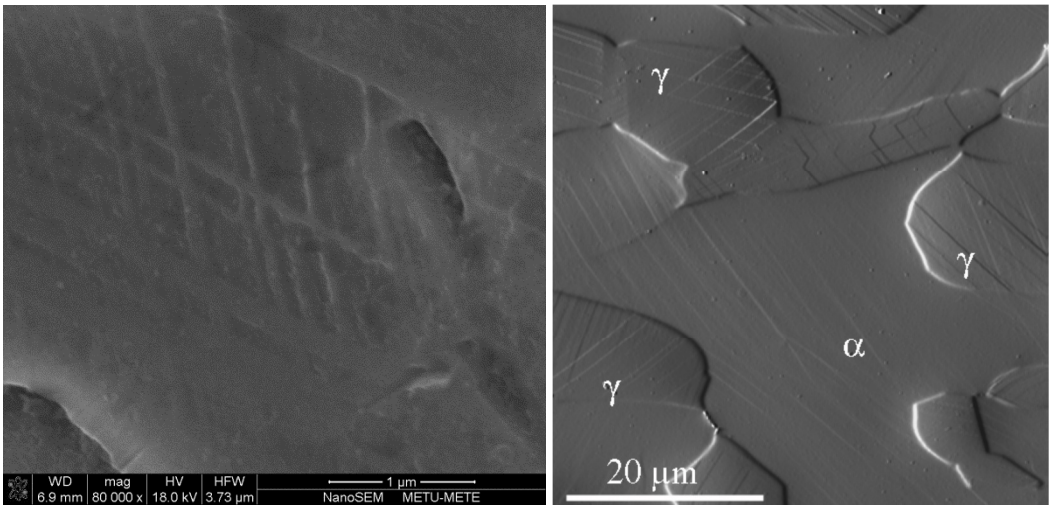

Figure 80. Crossed slip bands on γ grains observed using SEM during the present study (left) and using atomic force microscopy by Serre et al. [176].

It was documented that there was a difference in the morphology of slip bands depending upon whether they were revealed on γ or δ grains. Slip bands were straight and often inclined with respect to the loading axis (Figure 79). Length of these bands was very close to the size of the grains. As the plastic deformation was increased, two slip band set were visible within the γ grains, which were crossed (Figure 80 left). It could be suggested that the dislocation

slip mode was planar in γ, which has been confirmed by atomic force microscopy (Figure 80 right) [173] and TEM (Figure 78) [173, 175].

Curvilinear slip bands were observed on the surface of δ grains at high ΔK values (Figure 81). Some of these bands were connected to the neighbouring γ grain (Figure 81 right), whereas some of them seemed to be originated in δ grains from the plasticity process during testing. Crystallographic compatibility between δ and γ determines the dislocation transfer process in DSS [177, 178]; the Kurdjumov-Sachs (KS) crystallographic relation must be satisfied for such a BCC/FCC system:

$$\{111\}_{FCC} // \{110\}_{BCC} \text{ and } \langle 011\rangle_{FCC} // \langle 111\rangle_{BCC}, \quad (28)$$

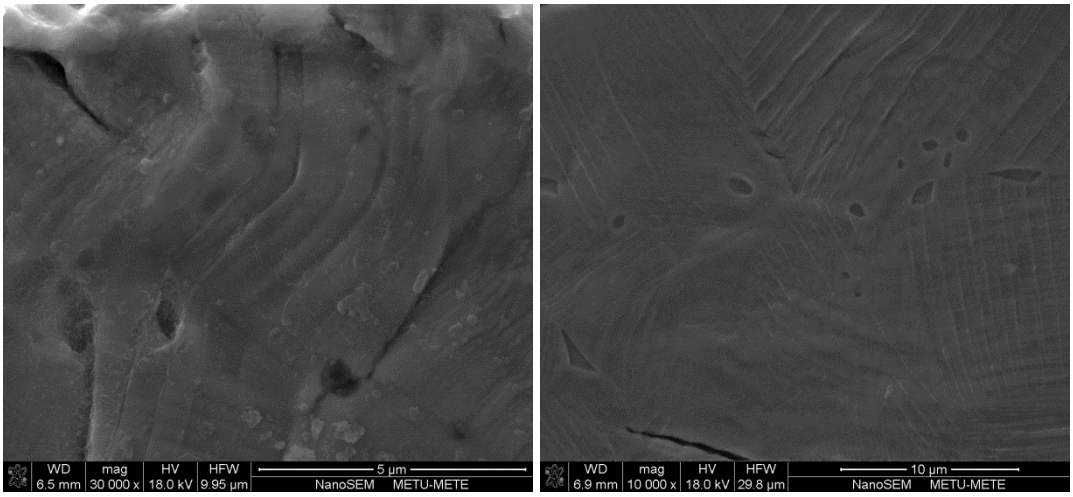

Figure 81. Slip bands on δ grains observed using SEM.

5.9.3. Secondary phases and solute redistribution effect

During side-view examinations, some particles were detected that promoted secondary cracks with the accumulation of slip bands in γ grains (Figure 82). EDX analyses indicated high Si and Mn in these particles, therefore they were probably oxides and sulfides of Si and Mn (Table 15). These inclusions were typical for both weldments and eliminating the formation of them is almost impossible in arc welding operations. Due to their secondary importance, neither intermetallic nor Cr-nitride precipitates' effects on FCP will be subjected in this section, but γ_2.

Paris-Erdoğan relation parameters were measured and calculated from logarithmic transformations of the crack propagation rates with respect to stress intensity factor ranges, in the stable crack propagation stage of the FCP progresses (Table 16). GMAW yielded relatively better performances during FCP test in air and under chloride attack at high loading frequencies.

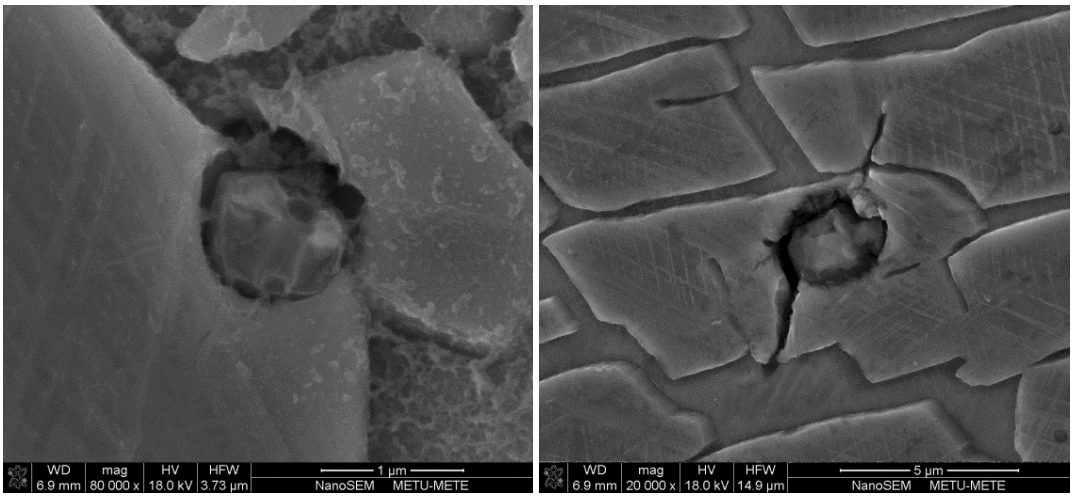

Figure 82. The particles that provide preferential site for side crack initiation in γ grains.

Table 15. EDS analysis of the particles found in γ grains.

	Al	Si	Nb	Mo	Ti	V	Cr	Mn	Ni	Fe
wt %	0.94	3.97	0.55	2.57	5.69	0.60	27.81	13.24	6.38	38.25

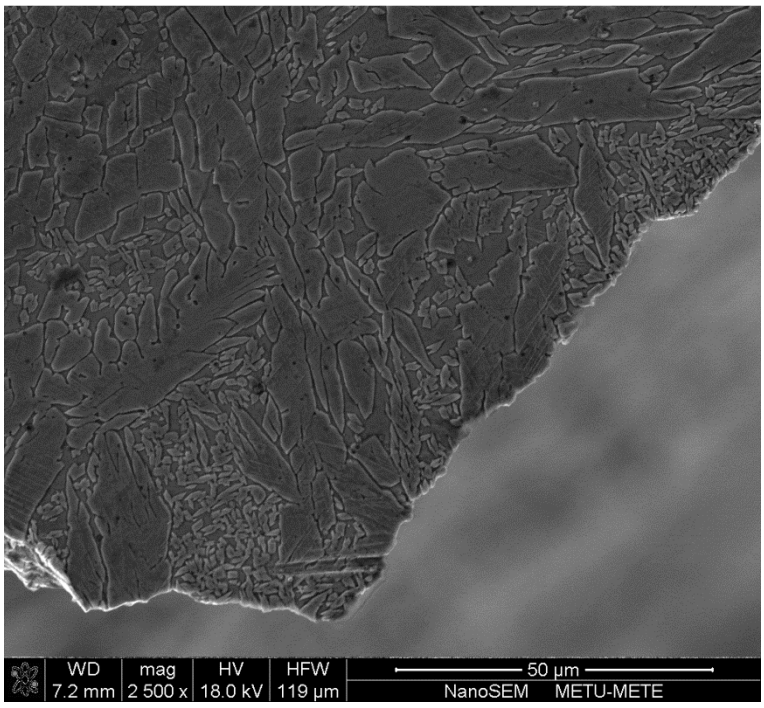

Figure 83. Crack path on CT specimen sectioned from GMA weldment.

Pokluda et al. [176] investigated the fatigue threshold behaviour of the grade 2507 at temperatures -50°C, 20°C and 150°C and observed tortuous crack paths via crack deflection and branching mainly at δ/γ interfaces. They concluded that the fine grained duplex microstructure constituted the principal reason for the high FCP resistance in the near-threshold region.

Table 16. "n" and "C" Paris-Erdoğan definition parameters tabulated with respect to the welding method and testing environment.

	BM		GMAW			HPAW		
	L-T	T-L	A 20	Cl 10	Cl 5	A 20	Cl 10	Cl 5
C	4.90×10^{-11}	2.00×10^{-11}	9.33×10^{-13}	6.31×10^{-13}	2.95×10^{-14}	7.94×10^{-13}	2.82×10^{-13}	3.89×10^{-14}
n	2.27	2.52	3.39	3.50	4.34	3.48	3.72	4.22
ΔK_{th}	23.61	23.25	24.48	23.58	24.58	24.47	23.00	24.25

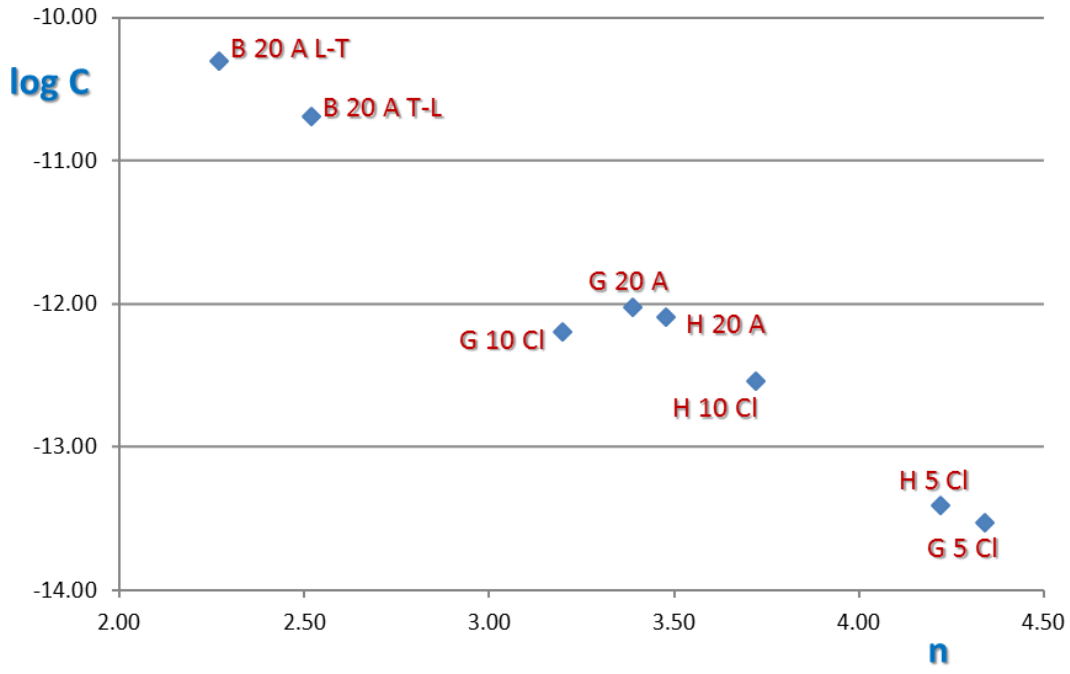

Figure 84. Graphical representation for the welding method and the testing environment incluence on "n" and "C" Paris-Erdoğan definition parameters.

Thanks to relatively fine grain size and γ_2 precipitates in FZ obtained using GMAW, multi-pass weld metal was found to be more successful in air as far as the crack propagation resistance was concerned. It can be seen in Figure 83 that in primary γ grains (allotriomorphic and Widmanstätten) the fractured surface became less tortuous and crack was observed to be deflected more while in progress through γ_2 colonies. The orientation relationships between intragranular γ_2 and δ matrix are close to K–S with small deviations

[173] and if there is no threat for the chemical inhomogeneity, which is yielded by its precipitation process, γ_2 seems to benefit FCP resistance.

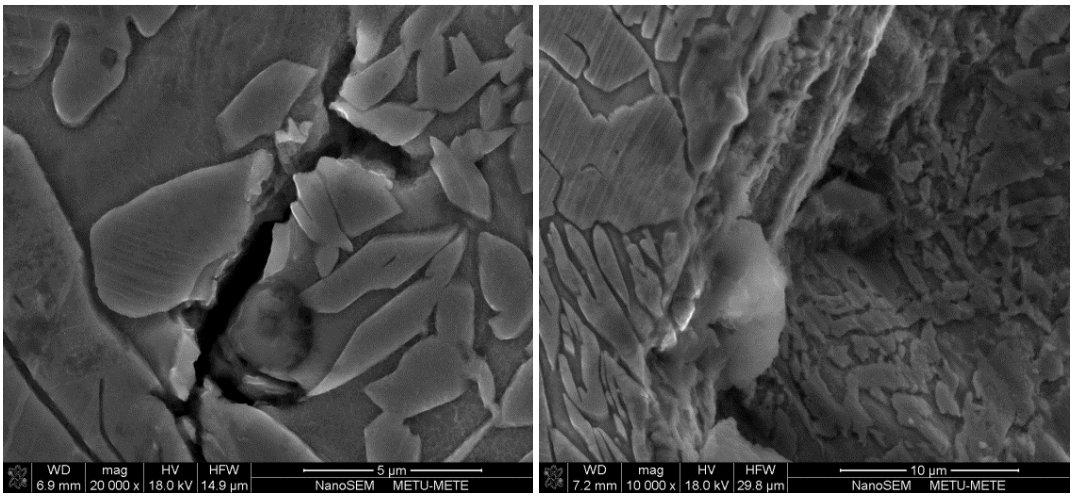

Figure 85. Side-section (left) and fracture surface (right) of the FZ in GMAW specimen. Secondary austenite in acicular form can easily be revealed on the fracture surface.

It was observed that there was no significant difference in the FCP behaviour during the process in laboratory air and sour environments at high frequencies (Figure 84). However, at low frequency of testing, γ_2 indeed generally provided a preferential path for FCP during the tests operated in 3.5% NaCl solution (Figure 85) and this affected the overall behaviour and its indicators (Figure 84).

EDX analyses showed that there was a slight depletion in Cr and Mo in the neighbourhood of γ_2 precipitates. Since the lateral resolution of SEM/EDS is typically 2 to 3 µm, the analysis giving limited data was understandable. Sathirachinda et al. [181] characterised the phases in the grade 2205 by means of SEM/EDS, TEM/EDS, magnetic force microscopy (MFM) and scanning Kelvin probe force microscopy (SKPFM). Immersing the material to HCl, HNO_3, H_2O and $FeCl_3.6H_2O$, it was verified by BSE-SEM graphs and AFM topographies that phase boundaries were preferential locations for dissolution.

During high frequency tests, it could be said that there was no enough time for the attack of Cl^-. Therefore, Cr and Mo depletion and the relatively low local PRE_N index did not make a significant difference concerning the role of γ_2. But still there was a small difference in the FCP behaviour during the process in laboratory air and sour environments at high frequencies. Reduction in the crack growth resistance during low frequency FCP tests in NaCl solution might be related to the hydrogen pickup process. Depending upon atomic force microscopy analyses and micro-hardness examinations, Roychowdhury *et al.* [174] proposed that hydrogen absorption had more significant effect on γ then δ. They observed cracks of 150 to 200 nm in depth in γ grains just after hydrogen charging. Głowacka *et al.* [175] utilized electrochemical cathodic hydrogen charging to the grade 2205 and observed a

strong increase of dislocation (slip and twin) density in δ grains, whereas generation of stacking faults were noticed in γ grains.

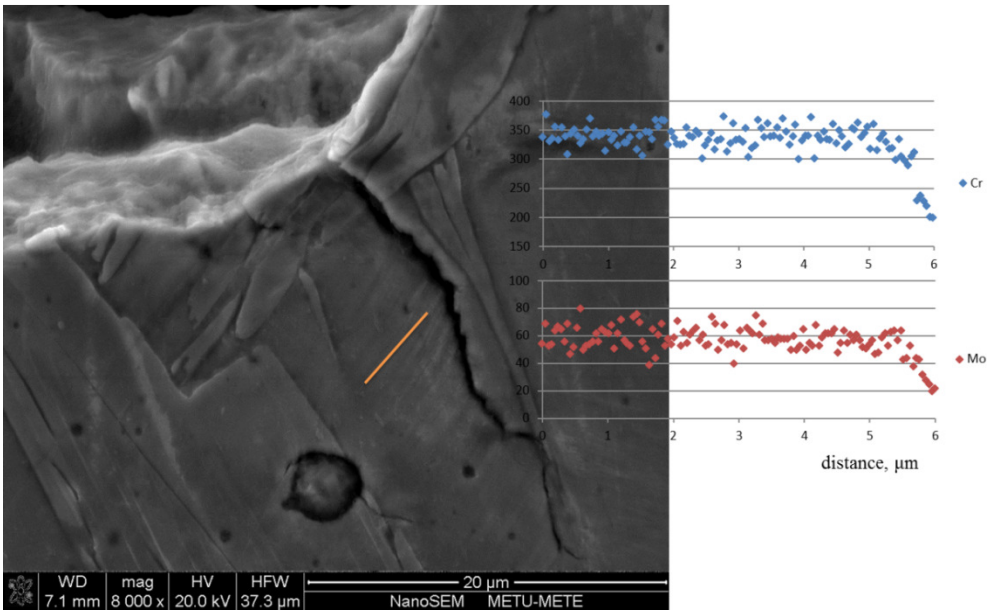

Figure 86. EDX analysis around a secondary crack.

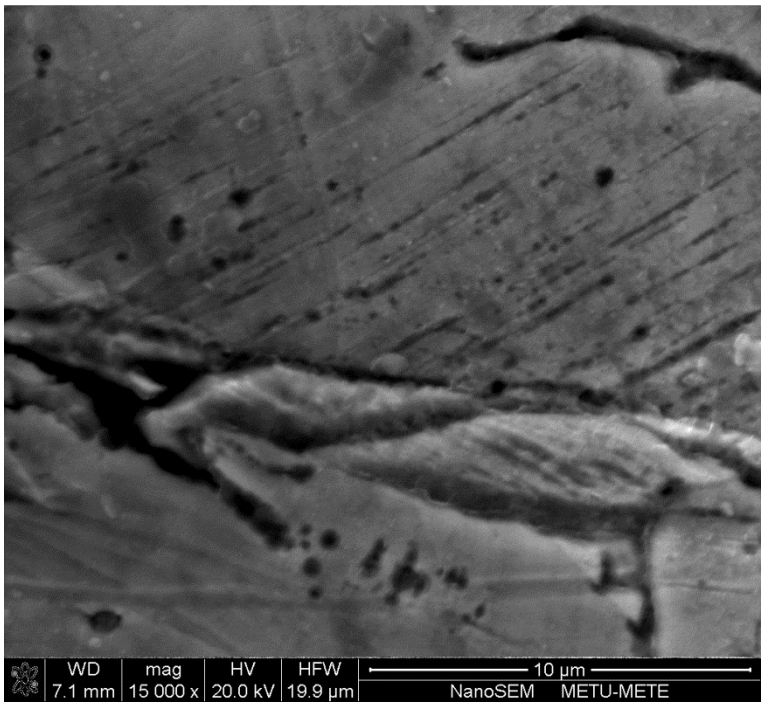

Figure 87. Pittings lead to favorable path for crack propagation.

Corrosion is a material diffusion and dissolution process and therefore time dependent, as well as chemical composition of the material and the environment. The strain energy and curvature of the surface govern the kinetics of the process. Once a crack is formed, the surface roughness evolves and the rate of the material dissolution increases resulting in pit formation. Pitting itself is a stress concentrator and therefore it may affect the preferred crack path. Stahle *et al.* [183] demonstrated how a pit becomes a crack in their study. They suggested that the material dissolution rate was proportional to the total available energy provided as elastic strain energy and surface energy.

Adeli *et al.* [184] estimated the critical pitting temperature (CPT) of the grade 2205 was above 35^{o}C if chemical homogeneity was ensured. Employing SEM, they observed that initiation of pits were in γ grains and suggested that lower PRE_N value of the phase was responsible for such a preference. Ebrahimi *et al.* [186] observed that increasing the sensitisation time reduced the CPT value.

CHAPTER 6

CONCLUSION

The study was set out to investigate, in the first place, the weldability of duplex stainless steel grade 2205, employing a recently developed welding process, hybrid plasma-gas metal arc welding. Not only the welding parameters that determines the specific point energy, but also the groove design had to be developed to obtain proper convections in the weld pool, which definitely governs the diffusion kinetics of interstitial and substitutional elements and phase transformations, as well as the solidification structure. The study, then, has sought to generate the preliminary data for crack propagation progress through such a non-conventional fusion zone structure. The output of the study has provided interesting data and documents about the controversial effect of the intragranular secondary austenite precipitates in acicular form on crack propagation behaviour in the as-welded duplex stainless steel both in laboratory air and under chloride attack.

During a design process of enclosing and structural assemblies, welding joints were assumed to have discontinuities and imperfections before the delivery, which are sometimes invisible or undetectable using existing non-destructive inspection (NDI) technologies. Therefore, linear elastic fracture mechanics approach is obviously sounds better than low- or high-cycle fatigue based approaches during any work that is supposed to interest the fatigue performance of weldments, such as for a fitness-for-service assessment and/or a damage tolerant design.

Since the basic principle of this non-conventional welding process is based on the utilisation of two conventional welding techniques, namely gas metal arc welding and plasma arc welding, simultaneously and in the same torch, conventional gas metal arc welding and plasma arc welding torches and systems were also employed to fabricate the benchmarking specimens, which were also investigated through a comparative research and development methodology.

Conventional gas metal arc welding is a well proven technique and as-welded duplex stainless steel fabricated by this method is available for service as long as the heat input and pre-heat temperatures are precisely controlled. However, the technique is based on conduction (melt-in) mode of welding that limits penetration and therefore efficiency as like other conventional arc welding techniques, because multiple weld passes are required to complete a thick section. Contrary to the conduction mode of gas metal arc welding, keyhole capability of plasma arc welding and hybrid plasma-gas metal arc welding techniques provided an opportunity of working with narrow-gap assemblies, and this led to complete the

process in a single run for the thickness of 11 mm. Less total heat input and high aspect ratio of keyhole welds resulted in narrower HAZ and less residual stresses in the joints. Whereas, excessive δ fraction in as-welded duplex stainless steel was an adverse effect of autogenous plasma arc welding, as similar to the other keyhole welding processes, the keyhole based hybrid welding technique, hybrid plasma-gas metal arc welding, emerged as a technique that promoted sufficient amount of γ in the microstructure with the advantage of addition of filler wire, consisting 4% excess Ni. Additionally, the high-power density and synergic capability of the technique led to a single-pass and secondary austenite free weldment with considerably limited amount of detrimental intermetallic and nitride precipitations, because the reason for formation of these secondary phases is linked to multi-cycle thermal treatments during a conventional multi-pass welding technique.

This study concludes that hybrid plasma gas-metal arc welding makes keyhole welding applicable for DSS and manufacturers can reduce lead times and provide better metallurgy for DSS assemblies for critical service in marine and industrial environments. Its γ_2-free FZ provides comparable fatigue crack propagation performance in air and definitely benefits the corrosion fatigue property of the weldment in sour environments.

Microstructural and mechanical characterisation of the weldments fabricated utilizing hybrid plasma-gas metal arc welding should be enhanced and especially controversial effects of the secondary austenite have to be investigated further. Concerning fatigue crack propagation kinetics, additional tests at very low cycling frequencies (less than 1 Hz) have been scheduled. In addition to these low-frequency corrosion fatigue crack propagation tests,

- Strain-induced transformation under cycling loading in,
- Residual stress determination using X-ray diffraction, redistribution of residual stresses during fatigue crack propagation and the crack closure effect in, and
- The effect of N_2 constituent in the shielding gas on competitive growth during conduction and keyhole mode of welding of,

as-welded duplex stainless steels (grade 2205 and higher alloyed grades) have also been scheduled for upcoming thesis works.

REFERENCES

[1] J. O. Nilsson, "Super duplex stainless steels," *Materials Science and Techology,* vol. 8, pp. 685-700, 1992.

[2] J. D. Kordatos, G. Fourlaris and G. Papadimitriou, "The effect of cooling rate on the mechanical and corrosion properties of SAF 2205 (UNS 31803) duplex stainless steel welds," *Scripta Metallurgica,* vol. 44, pp. 401-408, 2001.

[3] E. M. Westin and A. Fellman, "Effect of laser and laser hybrid welding on the corrosion performance of a lean duplex stainless steel," *Journal of Laser Applications,* vol. 22, pp. 150-159, 2010.

[4] J. Pekkarinen and V. Kujanpää, "The effects of laser welding parameters on the microsturcture of ferritic and duplex stainless steels welds," *Physics Procedia,* vol. 5, pp. 517-523, 2010.

[5] J. O. Nilsson, P. Kangas, T. Karlsson and A. Wilson, "Mechanical properties, microstructural stability and kinetics of σ phase formation in 29Cr-6Ni-2Mo-0,38N super duplex stainless steel," *Metallurgical and Materials Transactions,* vol. 31, pp. 35-40, 2000.

[6] T. Omura, T. Kushida and Y. Komizo, "Microstructural features and corrosion properties in laser welded duplex stainless steels," *Welding International,* vol. 14, pp. 257-260, 2000.

[7] N. A. McPherson, H. Samson, T. N. Baker and S. N. Fernandez, "Steel microstructures in autogenous laser welds," *Journal of Laser Applications,* vol. 15, pp. 200-211, 2000.

[8] J. S. Ku, N. J. Ho and S. C. Tjong, "Properties of electron beam welded SAF 2205 duplex stainless steel," *Journal of materials Prcessing Technology,* vol. 63, pp. 770-775, 1997.

[9] V. Muthupandi, P. Bala Srinivasan, S. Seshadri and S. Sundaresan, "Effect of weld metal chemistry and heat input on the structure and properties of duplex stainless steel welds," *Materials Science and Engineering A,* vol. 358, pp. 9-16, 2003.

[10] E. Capello, P. Chiarello and B. Previtali, "Laser welding and surface treatment of a 22Cr-5Ni-3Mo duplex stainless steel," *Materials Science and Engineering A,* vol. 351,

pp. 334-343, 2003.

[11] V. Stergiou and G. Papadimitriou, “Effect of an electron beam surface treatment on the microstructure and mechanical properties of SAF 2205 joints produced with electron beam welding,” *Journal of Materials Science,* p. published online, 2011.

[12] H. C. Wu, L. W. Tsay and C. Chen, “Laser beam welding of 2205 duplex stainless steel with metal powder additions,” *The Iron and Steel Institute of Japan International,* vol. 44, pp. 1720-1726, 2004.

[13] P. Sathiya, M. Kumar Mishra and B. Shanmugarajan, “Effect of shielding gases on microstructure and mechanical properties of super austenitic stainless steel by hybrid welding,” *Materials and Design,* vol. 33, pp. 203-212, 2012.

[14] J. C. Ion, “Keyhole Welding,” in *Laser Processing of Engineering Materials*, Burlington, UK Elsevier Butterworth-Heinemann, 2005, p. 395.

[15] N. McPherson, K. Chi and T. Baker, “Submerged arc welding of stainless steel and the challenge from Laser welding process,” *Journal of Materials Processing Technology,* vol. 134, pp. 174-179, 2003.

[16] E. LeGuen, R. Fabbro, M. Carin, F. Coste and P. LeMasson, “Analysis of hybrid Nd:Yag laser-MAG arc welding processes,” *Optics and laser Technology,* vol. 43, pp. 1155-1666, 2011.

[17] L.-E. Stridh, “Laser Hybrid Welding in Stainless Steels and in High Strength Steels,” *Materials Science Forum,* Vols. 539-543, pp. 3991-3995, 2007.

[18] I. Dykhno and R. Davis, “Joining GMAW and GTAW,” *The Fabricator,* pp. 60-62, 7 November 2006.

[19] I. Dykhno and R. Davis, “Hybrid welding: an alternative to SAW,” *Welding Journal,* vol. 86, no. 10, pp. 42-47, 2007.

[20] “DIN 8580 "Manufacturing processes - Terms and definitions, division",” Deutsches Institut Fur Normung E.V. (German National Standard), 2003.

[21] L. Yu, F. E. H. Tay, D. P. Poenar and C. Iliescu, “Using contact imprinting for adhesive wafer-to-wafer bonding,” in *SPIE*, 2007.

[22] X. Sun, E. V. Stephensa and M. A. Khaleel, “Fatigue behaviors of self-piercing rivets joining similar and dissimilar sheet metals,” *International Journal of Fatigue,* vol. 29, no. 2, pp. 370-386, 2007.

[23] “aluMatter,” European Aluminium Association and MATTER, 2001-2010. [Online]. Available: http://aluminium.matter.org.uk.

[24] ISO/TR 581 Weldability - Metallic materials - General principles, International Organization for Standardization, 2005.

[25] J. Cornu, Advanced Welding Systems, Volume 3: TIG and related processes, Bedford, UK: IFS Publications, 1988.

[26] K. C. Mills, B. J. Keene, R. F. Brooks and A. Shirali, "Marangoni effects in welding," *Philosophical Transactions of The Royal Society A,* vol. 356, pp. 911-925, 1998.

[27] S. Lu, H. Fujii and K. Nogi, "Marangoni convection and gas tungsten arc weld shape variations on pure iron plates," *The Iron and Steel Institute of Japan International,* vol. 46, pp. 276-280, 2006.

[28] C. R. Heiple and J. R. Roper, "Mechanism of minor element effect on GTA fusion zone geometry," *Welding Journal,* vol. 61, pp. 7-102, 1982.

[29] F. Haughton, "Automatic arc-welding machine". USA Patent 1676985, July 1928.

[30] "The Welding Engineer's Current Knowledge," GSI SLV Duisburg, 2009.

[31] H. Ayrton, The Electric Arc, London: The Electrician, 1902.

[32] G. Ohm, Die galvanische Kette, mathematisch bearbeitet, Berlin: T.H. Reimann, 1827.

[33] E. Assuncao, S. Williams and D. Yapp, "Interaction time and beam diameter effects on the conduction mode limit," *Optics and Lasers in Engineering,* vol. 50, pp. 823-828, 2012.

[34] J. N. Dupont and A. R. Marder, "Thermal Efficiency of Arc Welding Processes," *Welding Journal,* vol. 74, pp. 406-416, 1995.

[35] H. B. Smartt, J. A. Stewart and C. J. Einerson, "Heat Transfer in Gas Tungsten Arc Welding," in *ASM ınternational Welding Congress*, Toronto, Canada, 1985.

[36] B. W. Fuerschbach and G. A. Knorovsky, "A Study of Melting Efficiency in Plasma Arc and Gas Tungsten Arc Welding," *Welding Journal,* vol. 70, pp. 287-297, 1991.

[37] A. Okada, "Application of Melting Efficiency and its Problems," *Journal of Japan Welding Society,* vol. 46, pp. 53-61, 1977.

[38] N. Collings, K. Y. Wong and A. E. Guile, "Efficiency of Tungsten-Inert Gas Arcs in Very High Speed Welding," *Proceedings of the Institution of Electrical Engineers,* vol. 126, pp. 276-280, 1979.

[39] Y.-S. Kim and T. Eagar, "Analysis of Metal Transfer in Gas Metal Arc Welding," *Welding Journal,* no. June, pp. 269 - 278, 1993.

[40] User: Mysid, "Wikipedia," 2008. [Online]. Available:

http://en.wikipedia.org/wiki/Gas_metal_arc_welding.

[41] O. Semenov, V. Demchenko, I. Krivtsun, U. Reisgen, O. Mokrov and A. Zabirov, "A dynamic model of droplet formation GMA welding," *Modelling and Simulation in Materials Science and Engineering,* vol. 40, no. 4, pp. 1-14, 2012.

[42] H. Ludwig, "Plasma-Energy Transfer in Gas-Shield Welding Arcs," *Welding Journal,* vol. 38, no. 7, pp. 296s-300s, 1959.

[43] E. Eckert and E. Pfender, "Plasma Energy Transfer to a Surface With and Without Electric Current," *Welding Journal,* vol. 46, no. 10, pp. 471s-479s, 1967.

[44] M. Tomsic and C. Jackson, "Energy Distribution in Keyhole Mode Plasma Arc Welds," *Welding Journal,* no. March, pp. 109s-115s, 1974.

[45] I. Dykhno and G. Ignatchenko, "MIG-plasma welding". USA Patent US 7235758 B2, 26 June 2007.

[46] E. Bain and W. Griffiths, "An introduction to iron-chromium-nickel alloys," *Transactions of the American Institute of Mining, Metallurgical and Petroleum Engineers,* vol. 75, pp. 166-211, 1927.

[47] R. Gunn, "Developments, grades and specifications," in *Duplex Stainless Steels*, Cambridge, Abington Publishing, 1997, p. 2.

[48] K. Hashimoto, K. Asami and K. Teramoto, "An X-ray photo-electron spectroscopic study on the role of molybdenum in increasing the corrosion resistance of ferritic stainless steels in HC1," *Corrosion Science,* vol. 19, no. 1, pp. 3-14, 1979.

[49] R. Newman, "The Dissolution and Passivation Kinetics of Stainless Alloys Containing Molybdenum—I. Coulometric Studies of Fe–Cr and Fe–Cr–Mo Alloys," *Corrosion Science,* vol. 25, no. 5, pp. 331-339, 1985.

[50] R. Newman and E. Franz, "Growth and repassivation of single corrosion pits in stainless steel," *Corrosion,* vol. 40, pp. 325-330, 1984.

[51] L. Karlsson, L. Ryen and S. Pak, "Precipitation of intermetallic phases in 22% Cr duplex stainless steel welds," *Welding Journal,* vol. 74, no. 1, pp. 28s-40s, 1995.

[52] H. Solomon and L. Levinson, "Mössbauer effect study of '475°c embrittlement' of duplex and ferritic stainless steels," *Acta Metallurgica,* vol. 26, no. 3, pp. 429-442, 1978.

[53] A. Ramirez, J. Lippold and S. Brandi, "The relationship between chromium nitride and secondary austenite precipitation in duplex stainless steels," *Metallurgical and Materials Transactions,* vol. 34 A, pp. 1575-1596, 2003.

[54] J. DuPont, "The Influence of Solid State Diffusion on Microstructural Development During Solidification," *Defect and Diffusion,* vol. 266, pp. 157-169, 2007.

[55] W. Kujanpää, N. Suutala, T. Takalo and T. Moisio, "Correlation between solidification cracking and microstructure in austenitic and austenitic-ferritic stainless steel welds," *Welding Wold,* vol. 9, pp. 55-75, 1979.

[56] H. Kokawa, E. Tsory and T. North, "Nitride precipitation in duplex stainless steel weld metal," *ISIJ International,* vol. 35, no. 10, pp. 1277-1283, 1995.

[57] C. Garzon, C. Serna, S. Brandi and A. Ramirez, "The relationship between atomic partitioning and corrosion resistance in the weld-heat affected zone microstructures of UNS S32304 duplex stainless steel," *Journal of Material Science,* vol. 42, pp. 9021-9029, 2007.

[58] N. Haddad, *The development of microstructure in duplex stainless steel welds,* PhD Thesis: Cambridge: Pembroke College, 1989.

[59] T. H. Chen, K. L. Weng and J. R. Yang, "The effect of high temperature exposure on the microstructural stability and toughness property in a 2205 duplex stainless steel," *Material Science and Engineering A,* vol. 338, pp. 259-270, 2002.

[60] W. Zhang, T. Debroy, T. A. Palmer and J. W. Elmer, "Modelling of δ-ferrite formation in a duplex stainless steel weld, considering non-uniform starting microstructure," *Acta Materiaila,* vol. 53, pp. 4441-4453, 2005.

[61] H. Sieurin and R. Sandström, "Austenite reformation in the heat affected zone of duplex stainless steel 2205," *Material Science and Engineering A,* vol. 418, pp. 250-256, 2006.

[62] J. Carlen, "Apparatebau mit SANDVIK 3RE60," *Werkstoffe und Korrosion,* vol. 21, no. 8, pp. 645-650, 1970.

[63] R. Baptista, V. Infante and C. Branco, "Study of the fatigue behavior in welded joints of stainless steels treated by weld toe grinding and subjected to salt water corrosion," *International Journal of Fatigue,* vol. 30, pp. 453-462, 2008.

[64] K. Kirkhope, R. Bell, L. Caron, R. Basu and K.-T. Ma, "Weld detail fatigue life improvement techniques. Part 1:review," *Marine Structures,* vol. 12, pp. 447-474, 1999.

[65] K. Kirkhope, R. Bell, L. Caron, R. Basu and K.-T. Ma, "Weld detail fatigue life improvement techniques. Part 2: application to ship structures," *Marine Structures,* vol. 12, pp. 477-496, 1999.

[66] G. Booth, Improving the fatigue performance of welded joints, Cambridge: The Welding Institute, 1999.

[67] B. S. Institution, BS5500, Unfired Fusion Welded Pressure Vessels, London: BSI, 1990.

[68] V. Cacesse, P. Blomquist, K. Berube, S. Webber and N. Orozco, "Effect of weld geometric profile on fatigue life of cruciform welds made by laser/GMAW processes," *Marine Structures,* vol. 19, pp. 1-22, 2006.

[69] "Oakland Bay Bridge Pile Connection Plate Welding Investigation Report," U.S. Department of Transportation Federal Highway Administration, 2005.

[70] R. Ritchie, "Near threshold fatigue crack propagation in steels," *International Metals Reviews,* vol. 24, no. 26, pp. 205-230, 1979.

[71] P. Paris and F. Erdogan, "A critical analysis of crack propagation laws," *Journal of Basic Engineering, Transactions of the American Society of Mechanical Engineers,* vol. December, pp. 528-534, 1963.

[72] R. Wei, "Fracture mechanics approach to fatigue analysis in design," *Journal of Engineering Materials and Technology, Transactions of the American Society of Mechanical Engineers,* vol. 100, pp. 113-120, 1978.

[73] F. King, "Corrosion Resistance of Austenitic and Duplex Stainless Steels in Environments Related to UK Geological Disposal," Nuclear Decommissioning Authority, UK, 2009.

[74] C. Clayton and I. Olefjord, "Passivity of austenitic stainless steels," in *Corrosion Mechanisms in Theory and Practice, P. Marcus and J. Oudar (eds.)*, New York, Marcel Dekker, 1995, pp. 175-199.

[75] R. Souto, I. Rosca and S. González, "Resistance to localized corrosion of passive films on a duplex stainless steel," *Corrosion,* vol. 57, pp. 300-306, 2001.

[76] A. Sedriks, Corrosion of Stainless Steels, New York: John Wiley, 1996.

[77] R. Pettersson and J. Flyg, "Electrochemical evaluation of pitting and crevice corrosion resistance of stainless steels in NaCl and NaBr," Outokumpu, 2004.

[78] Z. Szklarska-Smialowska, Pitting and Crevice Corrosion, Houston: NACE International, 2005.

[79] IMOA, "Practical guidelines for the fabrication of duplex stainless steels," International Molybdenum Association, London, 2001.

[80] M. Nyström and B. Karlsson, "Fatigue of duplex stainless steel influence of discontinuous spinodally decomposed ferrite," *Materials Science and Engineering A,* vol. 215, pp. 26-38, 1996.

[81] T. Marrow, A. Humphreys and M. Strangwood, "The crack initiation toughness for brittle fracture of super duplex stainless steel," *Fatigue and Fracture of Engineering Materials and Structures,* vol. 20, no. 7, pp. 1005-1014, 1997.

[82] J.-B. Vogt, "The fatigue properties of Duplex Stainless Steels: role of nmicrostructure," *Key Engineering Materials,* vol. 378, pp. 101-114, 2008.

[83] F. Iacoviello, M. Boniardi and G. M. La Vecchia, "Fatigue crack propagation in austeno-ferritic duplex stainless steeş 22Cr-5Ni," *Iternational Journal of Fatigue,* vol. 21, pp. 957-963, 1999.

[84] J.-B. Vogt, K. Massol and J. Foct, "Role of the microstructure on fatigue properties of 475°C aged duplex stainless steels," *International Journal of Fatigue,* vol. 24, pp. 627-633, 2002.

[85] T. Kang, D. Li, Y. Lee and C. Lee, "Alloying and aging effects on the fatigue crack growth of duplex stainless steels," *Materials Science and Engineering A,* vol. 251, pp. 192-199, 1998.

[86] European Committe for Standardisation, EN ISO 15614-1; Specification and qualification of welding procedures for metallic materials - Welding procedure test - Part 1: Arc and gas welding of steels and arc welding of nickel and nickel alloys, Brussels: CEN, 2004.

[87] ASTM Committe A01, Practice for Steel Castings, Stainless, Instrument Calibration, for Estimating Ferrite Content, West Conshohocken, PA, USA: American Society for Testing and Materials, 2001.

[88] ASTM Committe A01, Standard Practice for Steel Casting, Austenitic Alloy, Estimating Ferrite Content Thereof, West Conshohocken PA USA: American Society for Testing and Materials, 2001.

[89] AWS Committe, Procedures for Calibrating Magnetic Instruments to Measure the Delta Ferrite Content of Austenitic Stainless Steel Weld Metal, Miami, FL, USA: American Welding Society, 2003.

[90] H. Yelbay, İ. Çam and C. Gür, "Non-destructive determination of residual stress state in steel weldments by Magnetic Barkhausen Noise technique," *NDT&E International,* vol. 43, pp. 29-33, 2010.

[91] ASTM Subcommitte E07.01, Standard Practice for Radiographic Examination, PA, USA: American Society for Testing and Materials, 2012.

[92] ASME Committe, ASME Boiler and Pressure Vessel Code, New York: The American Society of Mechanical Engineers, 2011.

[93] AWS Committee on Mechanical Testing of Welds, ANSI/AWS B4.0; Standard Methods for Mechanical Testing of Welds, Miami, FL, USA: American Welding Society, 1998.

[94] A. S. E28.07, ASTM E23; Standard Test Methods for Notched Bar Impact Testing of Metallic Materials, West Conshohocken, PA, USA: American Society for Testing and Materials, 2012.

[95] A. S. E04.05, ASTM E384; Standard Test Method for Knoop and Vickers Hardness of Materials, West Conshohocken, PA, USA: American Society for Testing and Materials, 2011.

[96] ASM International, "Volume 09 - Metallography and Microstructures," in *Metals Handbook*, Novelty, OH, USA, ASM, 2004, p. 2733.

[97] G. Vander Voort, Metallography, Principles and Practice, pp 649, McGraw-Hill, 1984.

[98] C. Park, H. Kwon and M. Lohrengel, "Micro-electrochemical polarization study on 25% cr duplex stainless steel," *Materials Science and Engeneering A,* vol. 372, p. 180, 2004.

[99] J. Pardal, S. Tavares and M. Fonseca, "Deleterious Phases Precipitation on Superduplex Stainless Steel UNS S32750: Characterization by Light Optical and Scanning Electron Microscopy," *Materials Research,* vol. 13, no. 3, pp. 401-407, 2010.

[100] ASTM Subcommitte E04.08, ASTM E112; Standard Test Methods for Determining Average Grain Size, West Conshohocken, PA, USA: American Society for Testing and Materials, 2012.

[101] ASTM Subcommitte E04.14, ASTM E562; Standard Test Method for Determining Volume Fraction by Systematic Manual Point Count, West Conshohocken, PA, USA: American Society for Testing and Materials, 2011.

[102] ASTM Subcommitte E04.14, ASTM E1245; Practice for Determining the Inclusion or Second Phase Constituent Content of Metals by Automatic Image Analysis, West Conshohocken, PA, USA: American Society fot Testing and Materials, 2011.

[103] ASTM Subcommittee E08.06, ASTM E647; Standard Test Method for Measurement

of Fatigue Crack Growth Rates, West Conshohocken, PA, USA: American Society for Testing and Materials, 2011.

[104] B. Tolungüç, K. Yurtışık, S. Tirkeş, H. Gür and T. Ertürk, "2205 dubleks paslanmaz çeliklerinin hibrit plazma ark kaynaklı birleştirmelerinde mikroyapı dönüşümleri," *Mühendis ve Makina,* vol. 53, pp. 77-82, 2011.

[105] B. Tolungüç, Microstructural and Mechanical Characterization of Duplex Stainless Steel Grade 2205 Joined by Hybrid Plasma and Gas Metal Arc Welding, Ankara, Türkiye: Middle East Technical University, Metallurgical and Materials Engineering Department, 2012.

[106] H. Vannevik, J. O. Nilsso, J. Frodigh and P. Kangas, "Effect of elemental partitioning on pitting resistance of high-nitrogen duplex stainless steels," *The Iron and Steel Institute of Japan International,* vol. 36, pp. 807-812, 1996.

[107] G. Bastin and H. Heijligers, "Quantitative electron probe microanalysis of nitrogen," *Scanning,* vol. 13, no. 5, pp. 325-342, 1991.

[108] I. Moreno, J. Almagro and X. Llovet, "Determination of nitrogen in duplex stainless steels by EPMA," *Mikrochimica Acta,* vol. 139, pp. 105-110, 2002.

[109] J. Nowacki and A. Łukojc, "Microstructural transformations of heat affected zones in duplex steel welded joints," *Materials Characterization,* vol. 56, p. 436–441, 2006.

[110] M. Hättestrand, P. Larsson, G. Chai, J. Nilsson and J. Odqvist, "Study of decomposition of ferrite in a duplex stainless steel cold worked and aged at 450–500◦C," *Materials Science and Engineering A,* vol. 499, pp. 489-492, 2009.

[111] A. Błachowski, K. Ruebenbauer, J. Jura, J. Bonarski, T. Baudin and R. Penelle, "Mössbauer study of deformation induced martensitic phase transformation in duplex steel," *NUKLEONIKA,* vol. 48, no. 1, pp. 9-12, 2003.

[112] P. Hedström, Deformation and Martensitic Phase Transformation in Stainless Steels (PhD Thesis), Luleå, Sweden : Division of Engineering Materials Department of Applied Physics and Mechanical Engineering Luleå University of Technology , 2007.

[113] Y. Han and S. Hong, "Microstructural changes during superplastic deformation of Fe–24Cr–7Ni–3Mo–0.14N duplex stainless steel," *Materials Science and Engineering A,* vol. 266, pp. 276-284, 1999.

[114] W. Liu, J. He, M. Fan, P. Lu and L. Shao, "Deformation at Room and Low Temperatures and Martensite Transformation in Resistance Spot Welding Duplex," *Journal of Materials Science and Technology,* vol. 23, no. 3, pp. 319-322, 2007.

[115] P. Chiu, K. Weng, S. Wang, J. Yang, Y. Huang and J. Fang, "Low-cycle fatigue-induced martensitic transformation in SAF 2205 duplex stainless steel," *Materials Science and Engineering A,* vol. 398, p. 349–359, 2005.

[116] S. Tavares, R. Noronha, M. Silva, J. Neto and S. Pairis, "475°C Embrittlement in a Duplex Stainless Steel UNS S31803," *Materials Research,* vol. 4, no. 4, pp. 237-240, 2001.

[117] H. Abe, K. Shimizu and Y. Watanabe, "Low-temperature aging of delta-ferrite in 316L SS welds; changes in the mechanical properties and etching properties," *Journal of Power and Energy Systems,* vol. 2, no. 1, pp. 2-7, 2008.

[118] S. David, J. Vitek, J. Keiser and W. Oliver, "Nanoindentation Microhardness Study of Low-Temperature Ferrite Decomposition in Austenitic Stainless Steel Welds," *Welding Journal,* vol. August, pp. 235-s - 240-s, 1987.

[119] A. Armas, S. Degallaix, G. Degallaix, S. Herenu, C. Marinelli and I. Alvarez-Armas, "Beneficial effects induced by high temperature cycling in aged duplex stainless steel," *Key Engineering Materials,* vol. 345, pp. 339-342, 2007.

[120] E. Hall and S. Algie, "The sigma phase," *Metallurgical Reviews,* vol. 11, pp. 61-88, 1966.

[121] S. Algie and E. Hall, "Site ordering in some sigma phase structures," *Acta Crystallographica,* vol. 20, no. 1, pp. 142-142, 1966.

[122] S. Rideout, S. Manley, E. Kamen, B. Lement and P. Beck, "Intermediate phases in ternary alloy systems of transation elements," *Transactions of the American Institute of Mining, Metallurgical and Petroleum Engineers,* vol. 191, pp. 872-876, 1951.

[123] J. Kasper, "The ordering of atoms in the chi-phase of the iron-chromium-molybdenum system," *Acta Metallurgica,* vol. 2, no. 3, pp. 456-461, 1954.

[124] J. Nilsson, L. Karlsson and J. Andersson, "Secondary austenite formation and its relation to pitting corrosion in duplex stainless steel weld metal," *Materials Science and Technology,* vol. 11, no. 3, pp. 276-238, 1995.

[125] J. Lippold and A. Al-Rumaih, "Toughness and pitting corrosion of duplex stainless steel weld heat affected zone microstructure containing secondary austenite," in *Duplex Stainless Steels, KCI Publishing*, Maastricht, Netherlands, 1997.

[126] S. Brandi and J. Lippold, "The corrosion resistance of simulated multipass welds of duplex and superduplex stainless steels," in *Duplex Stainless Steels, KCI Publishing*, Maastrich, Netherlands, 1997.

[127] J. Nilsson and A. Wilson, “Influence of isothermal phase transformations on toughness and pitting corrosion of duplex stainless steel SAF 2507,” *Materials Science and Technology,* vol. 9, pp. 545-554, 1993.

[128] M. Kaplan, C. Gür and M. Erdoğan, “Characterization of Dual-Phase Steels Using Magnetic Barkhausen Noise Technique,” *Journal of Nondestructive Evaluation,* vol. 26, pp. 79-87, 2007.

[129] C. Jang, P.-Y. Cho, M. Kim, S.-J. Oh and J.-S. Yang, “Effects of microstructure and residual stress on fatigue crack growth of stainless steel narrow gap welds,” *Materials and Design,* vol. 31, p. 1862–1870, 2010.

[130] M. Young, L. Tsay, C.-S. Shin and S. Chan, “The effect of short time post-weld heat treatment on the fatigue crack growth of 2205 duplex stainless steel welds,” *International Journal of Fatigue,* vol. 29, pp. 2155-2162, 2007.

[131] Z. Wang, Z. Wang and X. Zhang, “Study on Fatigue Crack Behavior in Welded Structure of DSS 2205,” *Advanced Materials Research,* Vols. 503-504, pp. 991-994, 2012.

[132] Z. Wang and Z. Wang, “Study on Fatigue Crack Growth Rate of Welded Joint of Duplex Stainless Steel,” *Advanced Materials Research,* Vols. 291-294, pp. 941-944, 2011.

[133] A. Comer, Corrosion Fatigue of a Superduplex Stainless Steel Weldment, Dublin, Ireland: School of Mechanical and Manufacturing Engineering, Dublin City University, 2003.

[134] L. Schwarz, T. Vrtochova and K. Ulrich, “Electron beam welding of duplex steels with using heat treatment,” *Research Papers, Faculty of Materials Science and Technology in Trnava, Slovak University of Technology in Bratislava,* vol. 28, pp. 75-80, 2010.

[135] Y. Qiao, D. Zou, J. Li and Y. Han, “Effect of Solution Temperature on Microstructure of 2205 Duplex Stainless Steel Welded Joints,” *Materials Science Forum,* vol. 658, pp. 432-435, 2010.

[136] A. Vandewynckèle, E. Couso, J. Otero, M. de Lama and G. Rodríguez, “Laser-arc welding of duplex stainless steel,” 1Asociación de Investigación Metalúrgica del Noroeste, Porriño, Spain, 2007.

[137] T. Matus and L. Zhang, “Plasma MIG welding”. United States Patent US20030183604 A1, 2 October 2003.

[138] L. Zhang and T. Matus, “Plasma MIG welding with plasma torch and MIG torch”.

United States Patent US6693252 B2, 17 February 2004.

[139] I. Dykhno and G. Ignatchenko, “Mig-plasma welding”. World Intellectual Property Organization Patent WO2004043639 A1, 27 May 2004.

[140] I. Dykhno and G. Ignatchenko, “Super-mig”. United States Patent US 78672231, 23 October 2007.

[141] C. Limmaneevichitr and S. Kou, “Visualization of Marangoni convection in Simulated Weld Pools Containing a Surface-Active Agent,” *Welding Journal,* vol. 79, no. 11, pp. 324s-330s, 2000.

[142] T. Sandor, “ATIG Welding of Duplex Steel,” *Materials Science Forum,* vol. 589, pp. 49-54, 2008.

[143] T. Sándor and J. Dobránszky, “The experiences of activated tungsten inert gas (ATIG) welding applied on 1.4301 type stainless steel plates,” *Materials Science Forum,* vol. 537, pp. 63-70, 2007.

[144] P. D. Southwick and R. W. K. Honeycombe, “Decomposition of ferrite to austenite in 26%Cr - 2%Ni stainless steel,” *Metal Science,* vol. 14, pp. 253-261, 1980.

[145] J. Elmer, S. Allen and T. Eagar, “The influence of cooling rate on the ferrite content of stainless steel alloys,” in *2nd International Conference on Trends in Welding Research*, Gatlinburg, 1989.

[146] T. Chen and J. Yang, “Microstructural characterization of simulated heat affected zone in a nitrogen-containing 2205 duplex stainless steel,” *Materials Science and Engineering A,* vol. 338, pp. 166-181, 2002.

[147] Y. Yang, B. Yan, L. Li and J. Wang, “The effect of large heat input on the microstructure and corrosion behaviour of simulated heat affected zone in 2205 duplex stainless steel,” *Corrosion Science,* vol. 53, p. 3756–3763, 2011.

[148] C. Chen, H. Yen, T. Yu and J. Yang, “Intragranularly Nucleated Austenite in a 2205 Duplex Stainless Steel,” *Materials Science Forum,* Vols. 539-543, pp. 4881-4886, 2007.

[149] R. Magnabosco, “Kinetics of Sigma Phase Formation In a Duplex Stainless Steel,” *Materials Research,* vol. 12, no. 3, pp. 321-327, 2009.

[150] H. Sieurin and R. Sandström, “Sigma phase precipitation in duplex stainless steel 2205,” *Materials Science and Engineering A,* vol. 444, pp. 271-276, 2007.

[151] A. Weisbrodt-Reisch, M. Brummer, B. Hadler, B. Wolbank and E. Werner, “Influence of temperature, cold deformation and a constant mechanical load on the

microstructural stability of a nitrogen alloyed duplex stainless steel," *Materials Science and Engineering A,* vol. 416, pp. 1-10, 2006.

[152] J. Cabrera, A. Mateo, L. Llanes, J. Prado and M. Anglada, "Hor deformation of duplex stainless steels," *Journal of Materials Processing Technology,* vol. 143, pp. 321-325, 2003.

[153] T. Saeid, A. Abdollah-zadeh, T. Shibayanagi, K. Ikeuchi and H. Assadi, "EBSD Investigation of Friction Stir Welded Duplex Stainless Steel," *World Academy of Science, Engineering and Technology,* vol. 61, pp. 376-379, 2010.

[154] M. Martins and L. Forti, "Effect of aging on impact properties of ASTM A890 Grade 1C super duplex stainless steel," *Materials Characterization,* vol. 59, pp. 162-166, 2008.

[155] Y. Han, D. Zou, W. Zhang and R. Huang, "Sigma Phase Precipitation of Duplex Stainless Steel and Its Effect on Corrosion Resistance," *Materials Science Forum,* Vols. 620-622, pp. 391-394, 2009.

[156] N. Lopez, M. Cid and M. Puiggali, "Influence of siphase on mechanical properties and corrosion resistance of duplex stainless steels," *Corrosion Science,* vol. 41, pp. 1615-1631, 1999.

[157] G. Dieter Jr., in *Mechanical Metallurgy*, New York, McGraw-Hill, 1961, p. 395.

[158] K. Tosha, "Influence of residual stresses on the hardness number in the affected layer produced by shot peening," in *2nd Asia-Pacific Forum on Precision Surface Finishing and Deburring Technology*, Seoul, Korea, 2002.

[159] R. Dakhlaoui, C. Braham and A. Baczmanski, "Influence of chemical composition and residual stresses on mechanical properties of duplex stainless steel studied by X-ray and neutron diffraction," *Journal of Neutron Research,* vol. 15, no. 2, pp. 131-137, 2007.

[160] J. Johansson and M. Oden, "Micro- and macrostress evolution in a duplex stainless steel during uniaxial loading," *Material Science Forum,* vol. 347, pp. 603-608, 2000.

[161] X. Wang, X. Yang, Z. Guo, Y. Zhou and H. Song, "Nanoindentation Characterization of Mechanical Properties of Ferrite and Austenite in Duplex Stainless Steel," *Advanced Materials Research,* Vols. 26-28, pp. 1165-1170, 2007.

[162] I. Calliari, M. Zansco, P. Bassani and E. Ramous, "The phase stability in Cr-Ni and Cr-Mn duplex stainless steels.," *Journal of Material Sciences,* vol. 46, pp. 6916-6924, 2011.

[163] V. Gavriljuk, A. Sozinov, J. Foct, J. Petrov and U. Polushkin, "Effect of nitrogen on the temperature-dependence of the yield strength of austenitic steels," *Acta Materialia,* vol. 46, no. 4, pp. 1157-1169, 1998.

[164] M. James, D. Hughes, Z. Chen, H. Lombard, D. Hattingh, D. Asquith, J. Yates and P. Webster, "Residual stresses and fatigue performance," *Engineering Failure Analysis,* vol. 14, pp. 384-395, 2007.

[165] T.-L. Teng, C.-P. Fung and P.-H. Chang, "Effect of weld geometry and residual stresses on fatigue in butt-welded joints," *International Journal of Pressure Vessels and Piping,* vol. 79, p. 467–482, 2002.

[166] K.-H. Chang and C.-H. Lee, "Residual stresses and fracture mechanics analysis of a crack in welds of high strength steels," *Engineering Fracture Mechanics,* vol. 74, pp. 980-994, 2007.

[167] A. Ohta, N. Suzuki, Y. Maeda, K. Hiraoka and T. Nakamura, "Superior fatigue crack growth properties in newly developed weld metal," *International Journal of Fatigue,* vol. 21, pp. S113-S118, 1999.

[168] M. Parry, H. Nordberg and R. Hertzberg, "Fatigue crack propagation in A514 base plate and welded joints," *Welding Journal,* vol. 51, no. October, pp. 486-490, 1972.

[169] Y. Shi, B. Chen and J. Zhang, "Effects of welding residual stresses on fatigue crack growth behaviour in butt welds of a pipeline steel," *Engineering Fracture Mechanics,* vol. 36, no. 6, p. 893–902, 1990.

[170] C. Liljedahl, O. Zanellato, M. Fitzpatrick, J. Lin and L. Edwards, "The effect of weld residual stresses and their re-distribution with crack growth during fatigue under constant amplitude loading," *International Journal of Fatigue,* vol. 32, pp. 735-743, 2010.

[171] R. Galatolo and A. Lanciotti, "Fatigue crack propagation in residual stress fields of welded plates," *International Journal of Fatigue,* vol. 19, no. 1, pp. 43-49, 1997.

[172] Y. Lam and K. Lian, "The effect of residual-stress and its redistribution on fatigue," *Theoretical and Applied Fracture Mechanics,* vol. 12, no. 1, pp. 59-66, 1989.

[173] M. Petrenec, V. Aubin, J. Polák and S. Degallaix, "Dislocation structures of duplex stainless steel in uniaxial and biaxial cyclic loading," *Materials Science Forum,* vol. 482, pp. 179-182, 2005.

[174] T. Kruml, J. Polák, K. Obrtlík and S. Degallaix, "Dislocation-structures in the bands of localized cyclic plastic strain in austenitic 316L and austenitic-ferritic duplex stainless-

steels," *Acta Materialia,* vol. 45, no. 12, pp. 5145-5151, 1997.

[175] I. Alvarez-Armas, "Low cycle fatigue behavior on duplex stainless steels," *Transactions of The Indian Institute of Metals,* vol. 63, no. 2-3, pp. 159-165, 2010.

[176] I. Serre, D. Salazar and J.-B. Vogt, "Plastic Deformation Quantified by Atomic Force Microscopy Measurements for Duplex Stainless Steel under Monotonic and Cyclic Loading," *Applied Mechanics and Materials,* vol. 13, pp. 163-172, 2008.

[177] I. Alvarez-Armas, M. Marinelli, J. Malarria, S. Degallaix and A. Armas, "Microstructure associated with crack initiation during low-cycle fatigue in a low nitrogen duplex stainless steel," *International Journal of Fatigue,* vol. 29, no. 4, pp. 758-764, 2007.

[178] M. Marinelli, S. Degallaix and I. Alvarez-Armas, "Dislocation structure developed in the austenitic-phase of SAF 2507 duplex stainless steel," *Materials Science and Engineering A,* Vols. 435-436, pp. 305-308, 2006.

[179] J. Pokluda, T. Podrábský, K. Slámečka, S. Pospíšilová and G. Chai, "Microstructure-aided Analysis of Fatigue Thresholds in Duplex Stainless Steel," *Materials Science Forum,* vol. 567, pp. 101-104, 2008.

[180] E. Monlevade, H. Goldenstein and I. Falleiros, "Intragranular formation of austenite during delta ferrite decomposition in a duplex stainless steel," *Journal of Material Science,* vol. 45, p. 5089–5093, 2010.

[181] N. Sathirachinda, R. Pettersson and J. Pan, "Depletion effects at phase boundaries in 2205 duplex stainless steel characterized with SKPFM and TEM/EDS," *Corrosion Science,* vol. 51, p. 1850–1860, 2009.

[182] S. Roychowdhury, V. Kain and R. Prasad, "Environmental Effects on the Fracture Toughness of a Duplex Stainless Steel (UNS S31803)," *Corrosion,* vol. 63, no. 5, pp. 442-449, 2007.

[183] A. Głowacka, M. Woźniak, G. Nolze and W. Świątnicki, "Hydrogen induced phase transformations in austenitic-ferritic steel," *Solid State Phenomena,* vol. 112, pp. 133-140, 2006.

[184] P. Stahle, C. Bjerken and A. Jivkov, "On dissolution driven crack growth," *International Journal of Solids and Structures,* vol. 44, p. 1880–1890, 2007.

[185] M. Adeli, M. Golozar and K. Raeissi, "Pitting Corrosion of SAF2205 Duplex Stainless Steel in Acetic Acid Containing Bromide and Chloride," *Chemical Engineering Communications,* vol. 197, pp. 1404-1416, 2010.

[186] N. Ebrahimi, M. Momeni, M. Moayed and A. Davoodi, "Correlation between critical pitting temperature and degree of sensitisation on alloy 2205 duplex stainless steel," *Corrosion Science,* vol. 53, pp. 637-644, 2011.

[187] I. Alvarez-Armas and S. Degallaix, "Low cycle fatigue behavior and microcracks nucleation on duplex stainless steels," *Key Engineering Materials,* Vols. 378-379, pp. 17-28, 2008.

[188] V. Di Cocco, E. Franzese, F. Iacoviello and S. Natali, "22 Cr 5 Ni duplex and 25 Cr 7 Ni superduplex stainless steel: Hydrogen influence on fatigue crack propagation resistance," *Engineering Fracture Mechanics,* vol. 75, pp. 705-714, 2008.

[189] H. Huang and N. Ho, "The observation of dislocation morphology in front of fatigue crack tips of as-rolled 2205 duplex stainless steel at various propagation rates," *Materials Science and Engineering A,* vol. 334, pp. 134-140, 2002.

[190] K. Makhlouf, H. Sidhom, I. Triguia and C. Braham, "Corrosion fatigue crack propagation of a duplex stainless steel X6 Cr Ni Mo Cu 25-6 in air and in artifical sea water," *International Journal of Fatigue,* vol. 25, pp. 167-179, 2003.

[191] A. El Bartali, V. Aubin, L. Sabatier, P. Villechaise and S. Degallaix-Moreuil, "Identification and analysis of slip systems activated during low-cycle fatigue in a duplex stainless steel," *Scripta Materialia,* vol. 59, pp. 1231-1234, 2008.

[192] I. Alvarez-Armas, U. Krupp, M. Balbi, S. Herenu, M. Marinelli and H. Knobbe, "Growth of short cracks during low and high cycle fatigue in a duplex stainless steel," *International Journal of Fatigue,* vol. 41, pp. 95-100, 2012.

[193] S. Tavara, M. Chapetti, J. Otegui and C. Manfredi, "Influence of nickel on the susceptibility to corrosion fatigue of duplex stainless steel welds," *International Journal of Fatigue,* vol. 23, pp. 619-626, 2001.

[194] H. Tan, Z. Wang, Y. Jiang, Y. Yang, B. Deng, H. Song and J. Li, "Influence of welding thermal cycles on microstructure and pitting corrosion resistance of 2304 duplex stainless steels," *Corrosion Science,* vol. 55, pp. 368-377, 2012.

[195] L. Chen, H. Tan, Z. Wang, J. Li and Y. Jiang, "Influence of cooling rate on microstructure evolution and pitting corrosion resistance in the simulated heat-affected zone of 2304 duplex stainless steels," *Corrosion Science,* vol. 58, pp. 168-174, 2012.

[196] S. Kawaguchi, N. Sakamoto, G. Takano, F. Matsuda, Y. Kikuchi and L. Mraz, "Microstructural changes and fracture behavior of CF8M duplex stainless steels after long-term aging," *Nuclear Engineering and Design,* vol. 174, pp. 273-285, 1997.

[197] K. Lee, H. Cho and D. Choi, “Effect of isothermal treatment of SAF 2205 duplex stainless steel on migration of δ/γ interface boundary and growth of austenite,” *Journal of Alloys and Compounds,* vol. 285, pp. 156-161, 1999.

[198] T. Omura, T. Kushida and Y. Komizo, “Microstructural features and corrosion properties in laser welded duplex stainless steels,” *Welding International,* vol. 14, no. 4, pp. 257-260, 2000.

CURRICULUM VITAE

PERSONAL INFORMATION

Surname, Name	:	Yurtışık, Koray
Nationality	:	Turkish (TC)
Date and Place of Birth	:	24 November 1975, Ankara
Marital Status	:	Married
Phone	:	+90 312 210 5841
Fax	:	+90 312 210 2518
Email	:	yurtisik@metu.edu.tr

EDUCATION

Degree	Institution	Year of Graduation
MS	METU Metallurgical and Materials Engineering	2002
BS	METU Metallurgical and Materials Engineering	1999
High School	Atatürk High School, Ankara	1993

PROFESSIONAL EXPERIENCE

Year	Place	Enrollment
2009 –	METU, Welding Tech. and NDT Res. and Appl. Center	Administrator – R&D
2007 – 2009	GAMA Industrial Plants Manuf. and Erection, Corp.	Chief Welding Eng.
2006 – 2007	Ticaret Securities Inc.	Corp. Finance Assoc.
2002 – 2006	HDM Quality Control Technologies and Services Inc.	Projects Coordinator
1999 – 2002	METU, Mathematics Department	Research Assistant
1997 – 1999	METU, Library, IT Dept.	LAN Administrator

PUBLICATIONS

Soldagem and Inspecao (Welding and Inspection), Characterization of Duplex Stainless Steel Weld Metals Obtained by Hybrid Plasma-Gas Metal Arc Welding, 2013 Vol. 18 No. 3 pp. 207-216.

Mühendis ve Makina, 2205 dubleks paslanmaz çeliklerinin hibrit plazma ark kaynaklı birleştirmelerinde mikroyapı dönüşümleri, 2011 Vol. 53 pp.77-82.

5th Defense Technologies Congress, Ankara 2010: '6063 ve 5754 Kalitelerindeki Aluminyum Alaşımlarının Değişen Alaşım İlavesi ve Darbeli Akım Gaz-altı Ark Yöntemiyle Kaynaklanabilirliği' (Jun 2010)

1st International Congress in Central and East European Region on Progressive Structural Materials and Their Joining Technologies, Slovakia 2009: 'Effect of Varying Laser Beam Welding Parameters on Microstructural Characteristics of SAE 409 Ferritic Stainless Steel Joints' (Oct 2009)

14th International Metallurgical and Materials Congress, İstanbul 2008: 'Microstructural Characterization of Heat Affected Zone in the 2507 Süper Duplex Stainless Steel Welds' (Oct 2008).

12th International Metallurgical and Materials Congress, İstanbul 2005: 'RBI In Petrochemical Industry (Oct 2005).

2nd International Non Destructive Testing Symposium, İstanbul 2003: 'Endüstride Çalışır Haldeki Sistemler için Özgün Ultrason, DGA ve KMA Metodları' (Oct 2003).

2nd International Non Destructive Testing Symposium, İstanbul 2003: 'Yerüstü Petrol Depolama Tanklarında Korozyon Mekanizmaları ve Tahribatsız Muayene Teknikleri' (Oct 2003).

11th International Metallurgical and Materials Congress, İstanbul 2002: 'Wear Behavior of Nitrided Hot Forging Die Steels' (Jun 2002).

HOBBIES

Music, Mountaineering, Cycling.